

**Recycled Water Injection in a Turbocharged Gasoline Engine and
Detailed Effects of Water on Auto-Ignition**

by

Jeongyong Choi

A dissertation submitted in partial fulfillment
of the requirements for the degree of
Doctor of Philosophy
(Mechanical Engineering)
in the University of Michigan
2019

Doctoral Committee:

Professor André L. Boehman, Co-Chair
Associate Research Scientist John Hoard, Co-Chair
Professor Venkat Raman
Professor Angela Violi

Jeongyong Choi
wjddydc@umich.edu
ORCID iD: 0000-0001-5144-1162

© Jeongyong Choi 2019

Acknowledgments

First of all, I must thank to my wife and daughter, Veronica Son and Jia Choi for their support. They gave me constant love, happiness and encouragement during this long journey. I also would like to give my special thanks to my parents and parents-in-law for their endless love and support.

I want to express my sincere gratitude to my research advisors, Prof. André Boehman and John Hoard. Because of their consistent research guidance, encouragement and financial support for last several years, I could finish my dissertation and got the faith in my abilities. Next my committee members, Prof. Angela Violi and Prof. Venkat Raman must be thanked for accepting to be on my committee and guiding me.

My fellow lab mates, Kwang Hee Yoo and Taehoon Han must be acknowledged as they helped me a lot in better understanding of the experimental setup and the results. Also, I have worked with many undergraduate students and master students. I must thank to them for their great assistance.

The financial support from Ford Motor Company as part of the Ford-UM alliance program is gratefully acknowledged.

Table of Contents

Acknowledgments	ii
List of Figures.....	vi
List of Tables	xii
List of Appendices.....	xiv
Abstract.....	xv
Chapter 1 Introduction.....	1
1.1 Background.....	1
1.2 Motivation.....	6
Chapter 2 Literature Review	9
2.1 Charge air cooler condensation	9
2.1.1 Charge air cooler.....	9
2.1.2 Charge air cooler condensation.....	11
2.1.3 Condensate Separator.....	15
2.2 Water Injection	17
2.2.1 Thermodynamic effects of water injection	18
2.2.2 Performance effects of water injection	19
2.2.3 Emission effects of water injection.....	21

2.2.4 Chemical effect of water injection	23
2.2.5 Limitation of water injection	24
Chapter 3 Charge Air Cooler Condensation Management	26
3.1 Experimental Setup.....	27
3.2 Charge air cooler condensation model validation	36
3.3 Tip in test and slowburn / misfire	39
3.3.1 Experiment setup	39
3.3.2 Experiment results; added water in the charge air cooler	42
3.3.3 Experiment results; generated condensation with humid air	44
3.3.4 Experiment results; comparison.....	46
3.4 Condensate separator	48
3.4.1 Numerical calculation setup.....	48
3.4.2 Numerical calculation results.....	53
3.4.3 Experiment setup and results	59
3.4.4 Separator design integrated in charge air cooler.....	63
3.5 Conclusion	66
Chapter 4 Effect of Water Injection on Auto-Ignition under Boosted Conditions..	68
4.1 Experimental.....	68
4.1.1 . Motored Engine Setup.....	68
4.1.2 . Water injection setup.....	71
4.1.3 . Heat release calculation.....	75
4.1.4 . Critical compression ratio	75
4.1.5 . Fuel Selection.....	76

4.1.6 . Test conditions	78
4.2 .Results	80
4.2.1 . Effects of Intake air property changes under boosted conditions ...	80
4.2.2 . Intake air cooling vs intake air property change	92
4.3 .Conclusion.....	99
Chapter 5 Chemical Reaction of Water with Oxygenated Fuels.....	101
5.1 Simulation Setup.....	101
5.1.1 Modeling tools	101
5.1.2 Methodology	102
5.1.3 Modeling setup.....	103
5.2 Results.....	107
5.2.1 Ignition Delay	107
5.2.2 Sensitivity and Reaction Pathway Analyses	111
5.3 .Conclusion.....	131
Chapter 6 Conclusions and Recommendations for Future Work.....	133
6.1 .Conclusion.....	133
6.2 .Recommendations for Future Work	137
Appendices.....	139
Bibliography	147

List of Figures

Figure 1-1. Actual(solid Lines) and projected(dotted Lines) fuel economy for passenger vehicles by location.....	2
Figure 1-2. Comparison of normal operating ranges for naturally aspirated and boosted-downsized engines	3
Figure 1-3. Temperature effect on start of spark retard	6
Figure 1-4. Humidity effect on start of spark retard	6
Figure 2-1. Comparison of the detachment velocity between analytical solutions and experimental data [23]	13
Figure 2-2. Sketch of vane separator – flow is left-to-right [34]	16
Figure 3-1. Experimental Setup, (a) external fan for the cooling air, (b) the engine and cooling air flow duct, and (c) the combustion air for intake.....	28
Figure 3-2. Schematic of intake air flow from the combustion air unit to engine	32
Figure 3-3. Cooling air flow distribution test setup	33
Figure 3-4. Cooling air flow distribution at the cross section of outlet of cooling air flow duct in m/s (interpolated) (a) without the charge air cooler, (b) with the charge air cooler.....	34
Figure 3-5. Schematic diagram of FTIR analysis	35
Figure 3-6. Condensation region. Color contours indicate the rate of liquid water condensation in grams of water per minute	36

Figure 3-7. Comparison of the amount of condensation between model calculations (line) and experiment results (triangles).....	39
Figure 3-8. Test condition (a) engine speed(RPM), (b) brake mean effective pressure(bar)	41
Figure 3-9. Schematic of experiment procedure in case of the known amount of water added.....	42
Figure 3-10. Schematic of experiment procedure in case of the generated condensation with high humid air.....	42
Figure 3-11. Maximum water mass fraction normalized by total fluid mass intake to engine cylinder (from FTIR analysis).....	43
Figure 3-12. Average number of slowburn event	44
Figure 3-13. Average number of misfire event.....	44
Figure 3-14. Total amount of water condensed (model) and measured amount of water(exp)	45
Figure 3-15. H ₂ O concentration measured by exhaust during tip-in transient	45
Figure 3-16. Total amount of water condensed (model) and measured amount of water(exp)	47
Figure 3-17. H ₂ O concentration measured in the engine exhaust.....	47
Figure 3-18. The separator configurations.....	50
Figure 3-19. Effect of total air path width on pressure drop.....	53
Figure 3-20. Effect of blade length on pressure drop	54
Figure 3-21. Effect of number of air path on pressure drop	55
Figure 3-22. Effect of angle of plate on pressure drop with fixed blade width	55

Figure 3-23. Effect of angle of plate on pressure drop with fixed air path width.....	56
Figure 3-24. Definition of ratio of open path width.....	57
Figure 3-25. Effect of ratio of open path width on pressure drop for various inlet air mass flow rate(g/s).....	57
Figure 3-26. Effect of ratio of open path width on separation efficiency for various droplet size and on average.....	58
Figure 3-27. Engine test setup	60
Figure 3-28. Comparison of pressure drop between simulation results (line) and experiment results (triangles), (a) 2000rpm, 7.8bar BMEP, (b) 3000rpm, 13.3bar BMEP.....	63
Figure 3-29. Comparison of pressure drop between simulation results (line) and experiment results (triangles).....	63
Figure 3-30. A prototype of separator integrated in charge air cooler.....	64
Figure 3-31. Comparison of pressure drop between simulation results (scatters) and empirical equation (line).....	65
Figure 3-32. Comparison of separation efficiency between simulation results (triangle) and empirical equation (line)	65
Figure 4-1. Schematic of the CFR engine setup	71
Figure 4-2. Schematic of water injection apparatus in the intake manifold	72
Figure 4-3. CO emission versus compression ratio at various intake pressures and water- fuel ratios for: (a) Gasoline, (b) PRF, (c) TRF	82
Figure 4-4. Critical compression ratio versus water-fuel ratio	83
Figure 4-5. Critical compression ratio versus intake air pressure.....	85

Figure 4-6. Change of critical compression ratio versus intake air pressure	86
Figure 4-7. Apparent heat release rate profiles for PRF with water-fuel ratio 0 – 1.5 as a function of crank angle at CR=9.15.....	87
Figure 4-8. Apparent heat release rate profiles for PRF with water-fuel ratio 0 – 1.5 as a function of crank angle at CCR	88
Figure 4-9. CA50 versus water-fuel ratio at CCR	88
Figure 4-10. CA1090 versus water-fuel ratio at CCR	89
Figure 4-11. Maximum bulk in cylinder temperature for PRF with water-fuel ratio 0 – 1.5 versus compression ratio.....	90
Figure 4-12. Zoomed in plot of Figure 4-11 indicating the thermal runaway points and differences in temperature.....	91
Figure 4-13. Maximum bulk in cylinder pressure for PRF with water-fuel ratio 0 – 1.5 versus compression ratio.....	91
Figure 4-14. Maximum in cylinder pressure expressed as a function of compression ratio for W/F ratio 0 (○) and W/F ratio 1.5(■), Two intake pressure are shown; 1bar(___), 2.5bar(___).....	92
Figure 4-15. CO emission of PRF expressed versus compression ratio at various intake pressure and water-fuel ratio.....	93
Figure 4-16. Critical Compression Ratio changes for PRF due to intake air cooling (differences of ■ and ▲) and intake air property changes (differences of ● and ■).....	94
Figure 4-17. Change of critical compression ratio versus intake air pressure	94

Figure 4-18. Apparent heat release rate profiles for PRF versus crank angle at CR=8.8.	95
Figure 4-19. Apparent heat release rate profiles for PRF versus of crank angle at CCR.	96
Figure 4-20. CA50 as a function of water-fuel ratio at CCR.....	96
Figure 4-21. CA1090 as a function of water-fuel ratio at CCR.....	97
Figure 4-22. Maximum bulk in cylinder temperature for PRF versus compression ratio	98
Figure 4-23. Zoomed in plot of Figure 3-21 indicating the thermal runaway points and differences in temperature.....	98
Figure 4-24. Maximum bulk in cylinder pressure for PRF versus compression ratio.....	99
Figure 5-1. The methodology used to separate the effects of H ₂ O on combustion	106
Figure 5-2. The specific heat capacity of the inlet charge mixture and gases	107
Figure 5-3. Ignition delay time for iso-Octane, Toluene, Ethanol, and n-Butanol with water (open symbols) without water (closed symbols).....	108
Figure 5-4. Ignition delay time changes due to water on (a) iso-Octane, (b) Toluene, (c) n-Butanol, and (d) Ethanol. Negative values indicate water shortens ignition delay	111
Figure 5-5. Reaction pathway for iso-Octane at 909K (a) with H ₂ O and (b) without H ₂ O	113
Figure 5-6. Reaction pathway for iso-Octane at 1250K (a) with H ₂ O and (b) without H ₂ O	115
Figure 5-7. Evolution of CH ₄ in the oxidation of iso-Octane with / without H ₂ O.....	115
Figure 5-8. Reaction pathway for iso-Octane at 1666K (a) with H ₂ O and (b) without H ₂ O	117
Figure 5-9. Reaction pathway for Toluene at 909K (a) with H ₂ O and (b) without H ₂ O	118

Figure 5-10. Reaction pathway for Toluene at 1250K (a) with H ₂ O and (b) without H ₂ O	119
Figure 5-11. Reaction pathway for Toluene at 1666K (a) with H ₂ O and (b) without H ₂ O	121
Figure 5-12. Reaction pathway for n-Butanol at 909K (a) with H ₂ O and (b) without H ₂ O	123
Figure 5-13. Reaction pathway for n-Butanol at 1250K (a) with H ₂ O and (b) without H ₂ O	124
Figure 5-14. Reaction pathway for n-Butanol at 1666K (a) with H ₂ O and (b) without H ₂ O	125
Figure 5-15. Reaction pathway for Ethanol at 909K (a) with H ₂ O and (b) without H ₂ O	127
Figure 5-16. Reaction pathway for Ethanol at 1250K (a) with H ₂ O and (b) without H ₂ O	129
Figure 5-17. Reaction pathway for Ethanol at 1666K (a) with H ₂ O and (b) without H ₂ O	130
Figure A-1. The condensation model simulates a single air passage in a charge air cooler core containing computational domains for charge air and water film.	140
Figure A-2. Entrainment model illustration	144

List of Tables

Table 1-1. Test engine specification	4
Table 3-1. Test engine specification	27
Table 3-2. Charge air cooler specification	30
Table 3-3. Heat rejection per temperature differences of CAC	30
Table 3-4. Thermal effectiveness of CAC	30
Table 3-5. Specification of combustion air unit.....	31
Table 3-6. List of test conditions	37
Table 3-7. Equivalent engine conditions for air mass flow rate	37
Table 3-8. Number of slowburn and misfire events	46
Table 3-9. List of geometrical dimensions of the separator.....	50
Table 3-10. Separator boundary conditions and equivalent engine conditions (Inlet: mass flow rate, Outlet: pressure)	52
Table 3-11. Specifications of separator prototypes for engine tests	59
Table 3-12. Specifications of separator used in calculation	64
Table 4-1. CFR engine specification	70
Table 4-2. HPLC water pump specification	72
Table 4-3. Tested fuel specifications	78

Table 4-4. Summary of the initial conditions for CFR water injection test.....	80
Table 5-1. Summary physical and chemical properties of tested fuels.....	105
Table 5-2. Summary of the mole fraction of the inlet charge mixture	106
Table B-1. Fuel properties of premium gasoline	146

List of Appendices

Appendix A. Condensation model description	139
Appendix B. Data of commercial premium gasoline fuel properties	146

Abstract

In recent years, many engine manufacturers have turned to downsizing and boosting of gasoline engines in order to meet the ever more stringent fuel economy and emissions regulations. With an increase in the number of turbocharged gasoline engines, solutions are required to manage knock under a range of operating conditions. The engine is required to operate with spark retard and/or boost reduction to provide knock reduction leading to reduced fuel economy.

The charge air cooler has been introduced to mitigate knock and yield a denser intake charge. However, under certain conditions, water condenses onto the charge air cooler inner surfaces, and this water can be introduced into the combustion chamber during a hard acceleration. Therefore, water ingestion may cause abnormal combustion behavior such as misfire or slowburn. Understanding of this water condensate ingestion issue and separating the condensate from the charge air are required. In addition, many researchers have advocated water injection as an approach to replace or supplement existing knock mitigation techniques. However, such systems require that the customer replenishes a water supply periodically. To maximize the efficiency of the water injection system for a given amount of water, a deeper understanding of the ability to capture and utilize water is required.

The first part of this dissertation pursues an understanding of the condensates generated inside of the charge air cooler is discussed. A 1-D condensation model to estimate the potential amount of water condensation and the experiments is conducted to understand how and how much the condensates are generated at specific air humidity and engine conditions using a 1.6L gasoline turbocharged engine. Moreover, to understand the ingestion of condensates into the cylinders, the hard acceleration is applied with the condensates and quantitatively correlated the amount of condensation and number of abnormal combustion behavior such as misfire and slowburn in different engine conditions. The next study is designing the condensation separator to prevent the abnormal combustion behavior due to the condensates ingestion. Corrugated plate separators have been widely used in gas-water separation and oil-water separation in many industries including marine diesel engines. However, this sort of separator has not been applied to gasoline engines in vehicles to separate the condensation in the charged air. An approach to designing a unit to separate condensation in the flow from the charge air cooler while maintaining a low pressure drop is described.

The effect of water on auto-ignition is described using modified CFR engine. Three test fuels gasoline, PRF, and TRF which have similar RON blends are used for this test at various intake pressure and amount of water conditions. The first test is done with constant intake air temperature and ϕ to exclude the effects of intake air cooling. Also, for more detail analysis of the effect of the intake charge property changes, the heat release analysis by comparing combustion phasing and duration, the bulk in-cylinder temperature and the bulk in-cylinder pressure analysis are done. For the second part of

this research, the comparison of the effect of the intake air cooling and the effect of the intake air property change is made.

The numerical calculations of the chemical effect of water addition with high octane number fuels and oxygenated fuels such as iso-Octane, toluene, n-Butanol, and Ethanol are presented. Using chemical reaction simulation, CHEMKIN, the simulations have been conducted on the change of hydrocarbon and oxygenated hydrocarbon oxidations process with water addition by examining ignition delay, sensitivity analysis and chemical reaction pathway analysis. At the beginning of the study, change of the ignition delay due to water addition is quantified. Then, the sensitivity analysis and the reaction pathway analysis are carried out to verify more detail of chemical effect of water on combustion process.

Through the studies presented in this thesis, some of potential contributions to high efficiency gasoline engine have been obtained. By collecting the condensate, the abnormal combustion behavior such as misfire or slowburn can be prevented, and also collected water condensate can be utilized as a source of water injection system. Because detail effect of water has been shown in the studies, it is expected that the gasoline engine could achieve higher compression ratio by avoiding knock with water injection system.

Chapter 1

Introduction

1.1 Background

In recent years, the increase in the number of vehicles has led to detrimental effects on the environment, forcing strong emissions and fuel consumption standards. Figure 1-1 shows the increases in average fuel economy from 2002 to 2016 for new vehicles in Corporate Average Fuel Economy (CAFE)-normalized miles per gallon [1]. To meet the increasingly stringent requirements, the automotive industry is moving towards direct injection boosted downsized gasoline engines.

The turbocharger compresses the intake air, so that denser air is able to be forced into cylinder. A simplified analysis by Gerty and Heywood [2] suggests that turbocharging and downsizing the engine would increase efficiency by about 16%. Boosting an engine increases its specific torque output while downsizing to maintain similar brake torque output causes the engine to operate with higher brake mean effective pressures (BMEPs) as illustrated in Figure 1-2. At higher BMEP, the engine fuel economy is improved due to reduction in relative heat transfer and pumping losses along with an overall increase of efficiency due to weight reduction and reduced frictional

losses. The major consequences of downsizing are the high levels of in-cylinder pressure and thermal loading, which results in increased possibility of abnormal combustion phenomena called knock. In contrast to these benefits, turbocharged gasoline engines may be limited by spark knock because of high cylinder pressure and temperature.

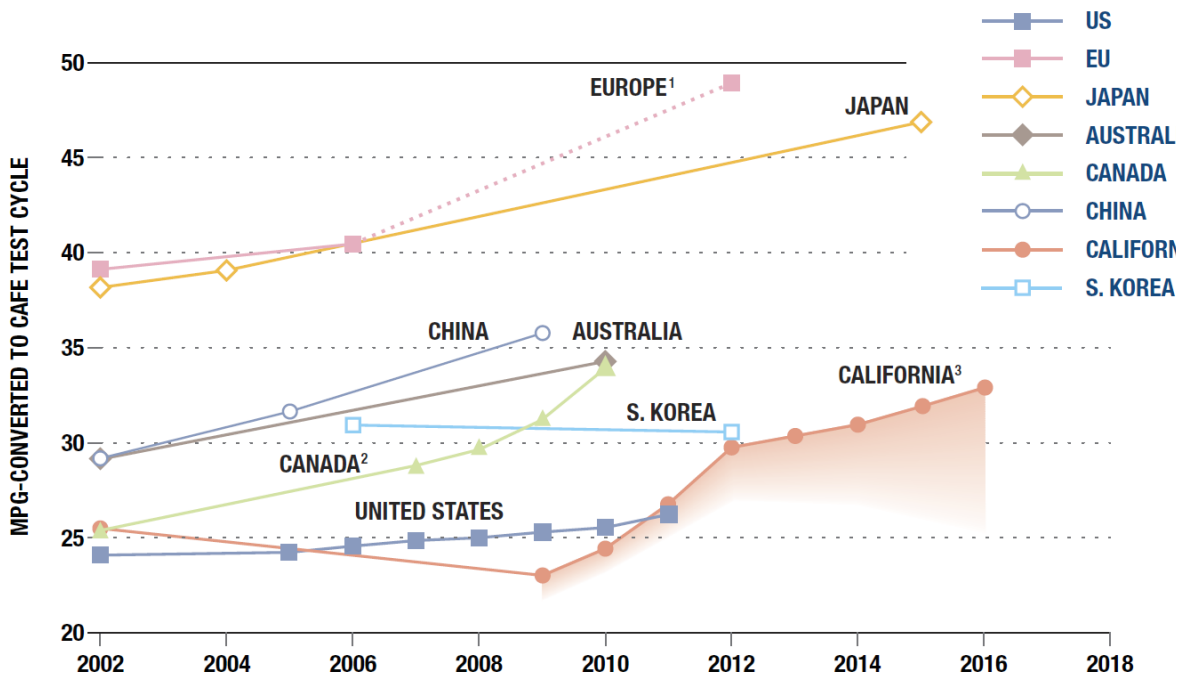


Figure 1-1. Actual(solid Lines) and projected(dotted Lines) fuel economy for passenger vehicles by location

Knocking noise is unacceptable to the driver and repeated exposure to the extreme local pressures and temperatures can cause damage to engine components. Advancing the spark has a dramatic effect on knock [3]. An increase in the spark advance produces a higher cylinder pressure and temperature closer to top dead center. The increased temperature of the unburned end-gas increases the tendency for auto-ignition and knock.

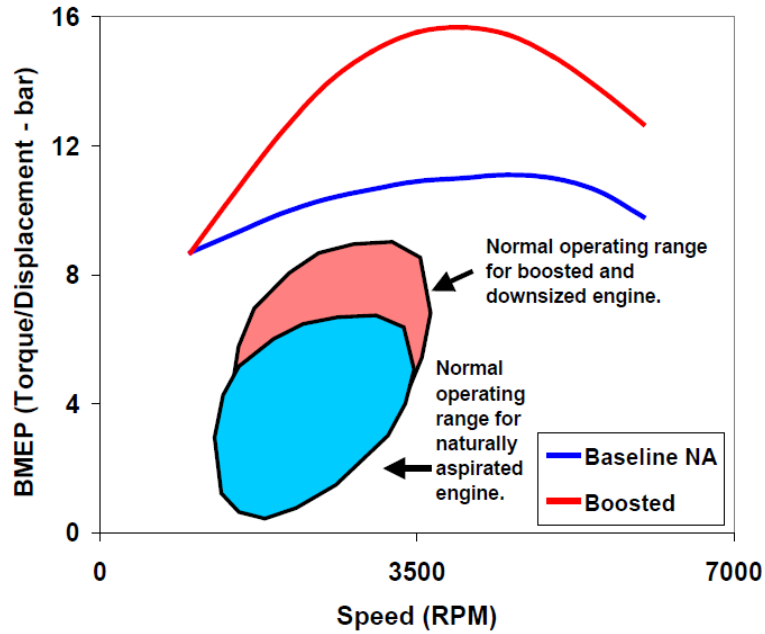


Figure 1-2. Comparison of normal operating ranges for naturally aspirated and boosted-downsized engines

A charge air cooler (CAC) is used to reduce intake air temperature and reduce the chance of knock. Moreover engine control systems adjust spark timing to lower the peak pressure and temperature. The spark retard results in significant decreases in torque, combustion stability, and fuel economy in addition to an increase in exhaust temperature. To avoid the need for excessive spark retard, compression ratio or boost is limited, which in turn limits engine efficiency and power. Use of extremely rich mixtures is also an effective method to limit the exhaust gas temperature at turbine inlet, but this method results in degradation of fuel efficiency. Higher octane fuel can be used when available to reduce the tendency to knock. Recently, cooled EGR has been shown to be advantageous for high compression engines. An alternative option to avoid fuel-rich mixtures or restrict engine designs to use of lower boost pressure or compression ratio, is to utilize the charge

cooling effect of water as an effective means to reduce end gas temperatures and hence knock.

A preliminary investigation explored the effect of charge air temperature and presence of water in the air on spark timing. Engine dynamometer testing was carried out using a four-cylinder turbocharged gasoline direct injection (GDI) engine. Table 1-1 shows the engine specifications. A series of experiments were designed to conduct a parametric study of intake temperature on knock. Note the effect of humidity is also included as part of the same study.

Table 1-1. Test engine specification

Displacement	1.596 L
Number of Cylinder	4
Bore / Stroke	79.0 / 81.4 mm
Compression Ratio	10:1
Maximum Power	133 kW @ 5700 rpm
Maximum Torque	250 N m @ 2500 rpm

To simulate the effects of charge air temperature and humidity on knock, the charge air cooler outlet temperature was varied to obtain intake manifold air temperature varying from 20 to 35 °C over a range of engine load and speed. Unless otherwise noted, the atmospheric condition at the engine intake (before the compressor inlet) was maintained constant at 53% relative humidity and 26 °C to obtain mean humidity ratio of 0.0113 gm water/gm dry air during the experiment. To study the effect of humidity on knock, the atmospheric temperature controller was adjusted to maintain steady temperature of 26°C while humidity was adjusted for relative humidity 30%, 50%, 70%

and 90% to obtain mean humidity ratios of 0.075, 0.013, 0.021 and 0.025 gm water/gm dry air at the intake of the engine turbocharger, respectively. The intake manifold temperature was maintained constant at 30°C throughout the experiment by adjusting the flowrate of cooling water through a water-air CAC. Multiple steady state engine speeds were tested; at each speed, load was increased until the engine control system identified slight knock events and initiated spark retard.

Figure 1-3 and Figure 1-4 show the maximum torque without knock limit versus engine speed, with lines of varying CAC-out temperature and humidity. The tests were done by increasing engine speed from 1250RPM to 3250RPM and load at given engine speed to determine the borderline of knock. At the time when spark retard starts, indicated torque was measured. Comparing the time when spark retard starts, it was interesting to note that the effect of temperature on start of spark retard has a more pronounced effect as compared to humidity. No significant effect on start of spark retard due to humidity variation could be observed for similar operating conditions. At lower engine speed, it was observed that intake cam timing was adjusted by the engine control to reduce volumetric efficiency to reduce knock tendency. The effect of changing cam timing was more prominent than intake air temperature at lower speed. At higher engine speeds, the effect of charge cooling variation on the start of spark retard was more prominent than low engine speeds.

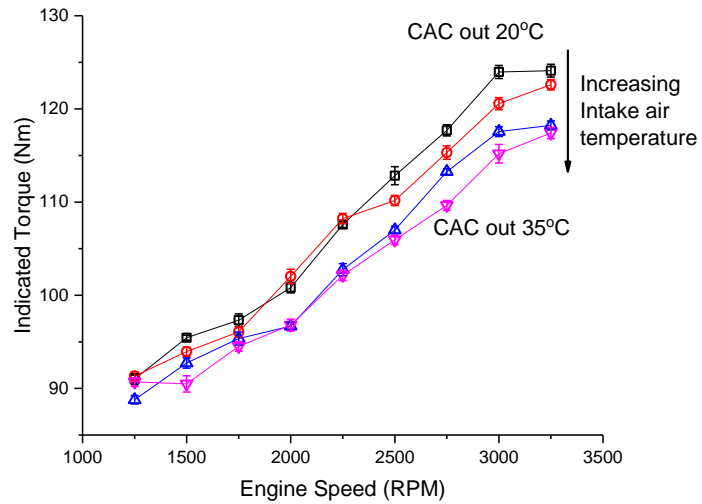


Figure 1-3. Temperature effect on start of spark retard

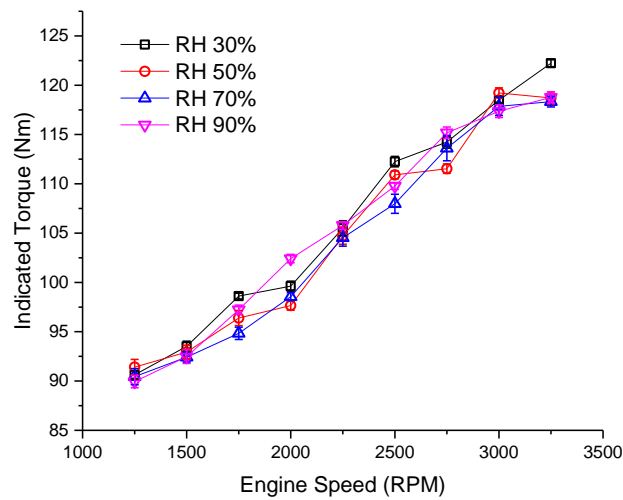


Figure 1-4. Humidity effect on start of spark retard

1.2 Motivation

As shown above, the automotive industry has been witnessing a major shift towards downsized boosted direct injection engines due to increasingly stringent emission and fuel economy targets. Boosted engines operate at a high mean effective pressure (MEP), resulting in higher in-cylinder pressures and temperatures, effectively

leading to increased possibility of abnormal combustion events like knock and pre-ignition. Therefore, the compression ratio and boost pressure in modern engines are restricted, which in-turn limits the engine efficiency and power. To mitigate conditions where the engine is prone to knocking, the engine control system uses spark retard and/or mixture enrichment, which decrease indicated work and increase specific fuel consumption.

The objective of the current work is to secure a possible source of water injection using charge air cooler condensation and to fully-understand the effect of water injection in boosting conditions resulting from changes in the fuel properties. To this end, experiments examined collection method of charge air cooler condensate and the effect of water injection. Chemical kinetic mechanisms for de-couple chemical effect of water injection from thermal effects such as changing specific heat and reducing intake air temperature will be selected and shown in the results.

Therefore, the research questions that will be addressed through this thesis are:

- Under what conditions does water condensate occur in the charge air cooler?
What factors affect the abnormal combustion, such as misfire or slowburn?
How could the condensate be separated from the charge air?
- Under boosted conditions, how does water affect the auto-ignition behavior of high octane number fuels? How much does the intake air properties change due to the effect of water under boosted condition? How much is this effect compared to the intake air cooling effect of water?
- What is the chemical effect of water? Does water show a different chemical effect with oxygenated fuels?

The current document is organized as follows. In Chapter 3, an investigation of the effect of charge air cooler condensate carried over to the cylinder is shown using four cylinder turbocharged gasoline direct injection engine. Moreover, condensate separator is designed using CFD simulation. Through this numerical study, condensate droplet behavior is analyzed, and the prototypes of the separator test results are shown. Chapter 4 presents an investigation of the effect of water on boosted condition. Water is injected to single cylinder research engine with three different fuels and 16 combinations of the boundary conditions. In Chapter 5, more detailed analysis is done by numerical analysis to identify a chemical effect of water. It presents the kinetic simulation results of two reference fuels and two oxygenated fuels with water. Finally, Chapter 6 presents summaries, conclusions, and recommendations for future work.

Chapter 2

Literature Review

2.1 Charge air cooler condensation

2.1.1 Charge air cooler

After the boosted, direct injection engine, had become mainstream among production vehicles, the importance of the charge air cooler has been emphasized. When the intake air is compressed using a turbocharger or supercharger, the temperature of the intake air is also increased. Due to high intake air temperature, the primary challenges of the boosted engine are higher mechanical and thermal loads to the engine and higher NO_x emissions. To partly resolve those issues, charge air cooling was introduced. There are several of benefits of the charge air cooling [4,5]. The first benefit is reducing the thermal load on the engine. As mentioned above, once the intake air is compressed, the temperature of the intake air is also increased due to a polytropic change of state of the air. The heated intake air temperature results in higher exhaust gas temperature and

temperature of the engine components. It also leads more heat loss and more material load on the engine parts. The second advantage of the intake air cooling is increasing the intake air density. With higher density of the cooled intake air, the intake air could contain more oxygen, so that it is possible to inject more fuel or make more complete combustion [6]. Therefore, the volumetric efficiency and the engine power are improved. The cooled intake air is also able to reduce NO_x emission because formation of NO_x has a strong temperature dependency [3]. The lower the intake air temperature, the lower the NO_x emission level. Another advantage of the intake air cooling on the spark ignition engine is suppressing spark knock. Due to high pressure and density of the intake air, the boosted spark ignition engine tends to be knock limited. So, the cooled intake air provides greater restriction of auto-ignition of the fuel.

The charge air cooler (CAC), also called an intercooler, is a heat exchanger located between the turbocharger and the intake manifold. Over several years, the efficiency of the charge air cooler has been improved by changing the type of the charge air cooler, fin geometries and charge air flows [6–8]. Generally, there are two types of charge air cooler: air-to-water and air-to-air [6,9]. The air-to-water charge air cooler uses a liquid coolant to cool the intake air. With such a system, the intake air temperature can be controlled by controlling the coolant temperature. However, since the engine coolant temperature is normally higher than the desired intake air temperature, a separate coolant system is necessary. There is also a risk of coolant leakage to the charge air cooler and the engine. In contrast, ambient air is utilized as a cooling medium in the Air-to-Air charge air cooler. The most common location for the air-to-air charge air cooler is in the front of the engine radiator. This system is very reliable since there are no moving parts

and there is easy access to the cooler. However when the ambient air is too hot or too cold, the intake air temperature is also too hot or too cold which affects combustion.

2.1.2 Charge air cooler condensation

If gas and liquid are present simultaneously in a tube, several types of gas-liquid flow patterns are identified: bubbly, slug, semi-annular, annular, and mist [10]. The patterns are decided by fluid properties, flow rates, and flow geometry. When gas flows in the pipe at a low flow rate, the small liquid bubbles are randomly distributed. By increasing the gas flow rate, the small liquid bubbles coalesce, and these form larger bubbles which is called slug flow. Understanding the slug flow is important since it occurs in several applications such as oil pipelines, nuclear reactors, refrigerants and air conditioning equipment. For example, when the water boils in the pipe of the heat exchanger or the boiling water reactor, the flow oscillates and is unstable. Flow instability may cause mechanical damage or disturb controller of the system [11–13].

The charge air becomes cooler and denser by improving the efficiency of the charge air cooler. However, these changes can lead to condensate production inside of the charge air cooler under some conditions. As high humidity air passes through the charge air cooler, it may be cooled below the dew point, so moisture condenses onto the charge air cooler surfaces [7]. To understand this phenomenon, there have been several analyses reported in the literature [14–17]. Understand the heat exchanger behavior, in itself, is not a significant problem. However, transients lead to complex multiphase behavior. With a hard acceleration, the condensate can be introduced into the engine cylinder causing abnormal combustion behavior [18].

After the condensate has formed on the inner surfaces of the charge air cooler, understanding the condensate flow behavior is important. Once the condensate is formed, the droplets are driven in the direction of the air flow due to shear forces. The condensate movement can be categorized into various regimes including partial slugs, slugs, films, and mist [19–21]. The slug regime has the most significant effect on the boosted system due to the large volume of water being moved and the pressure drop across the charge air cooler. Hence, the slug dynamics are the main focus of understanding condensate movement. A study conducted by Cho et al. [22] focused on the fluid velocity as a factor affecting the slug movement. It has been said that the fluid flow over the surface of the condensate causes a drag force. Once the drag force exceeds the adhesion force between the condensate and the surface, the condensate is detached and forms a droplet.

Equation (2-1) is the model for the detachment velocity Cho et al. developed. In equation (2-1) θ_s , θ_a , and θ_r are the static, advancing, and receding contact angles. The coefficients a and b are defined as follows, where D is the droplet diameter and H is the channel height. As shown in Figure 2-1, the model had a good agreement with the experimental results presented [23]. Although this equation gives good correlation for the detachment velocity for the condensate, it cannot be applied to the condensation in the charge air cooler because the surface finishes used in the model are not the same as the materials in a charge air cooler.

$$We_r Re_H^b = \frac{4\pi \sin^2 \theta_s \sin \frac{1}{2} (\theta_a - \theta_r)}{a(\theta_s - \sin \theta_s \cos \theta_s)} \quad (2-1)$$

where, $a = 46.247 \times \left(\frac{D}{H}\right)^{0.1757}$, $b = 0.2158 \times \left(\frac{D}{H}\right) - 0.6384$

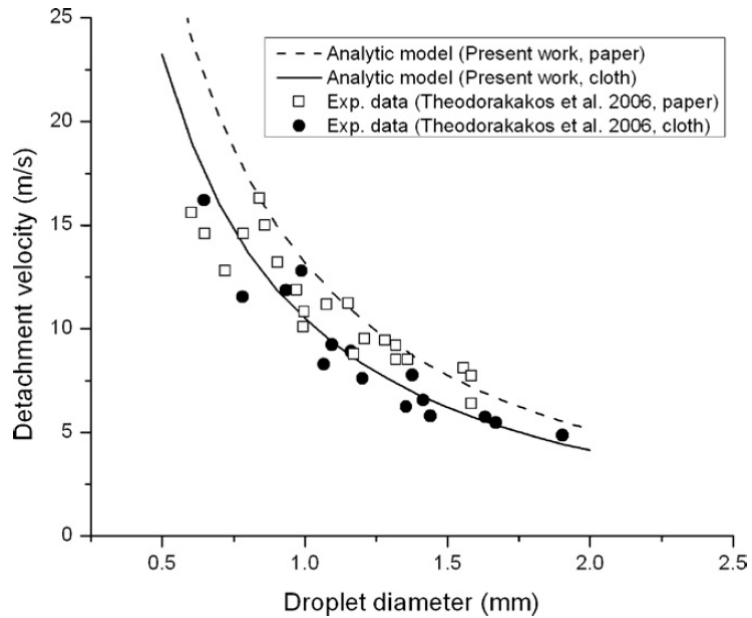


Figure 2-1. Comparison of the detachment velocity between analytical solutions and experimental data [23]

There are some of other related studies for how the condensate detaches from the wall of the charge air cooler. In reference [20], the authors have hypothesized that the droplets advance under stick-slip conditions as the contact angle between the gas, liquid, and solid advance. In another paper [21], they have analyzed how the condensate droplet is formed in a square channel, which is one geometry of the production charge air coolers.

The initial motion of the droplet has been studied and understood by models. Cheah et al. [20] have developed a model of droplet motion through the length of the channel. Also, Orell [24] has developed a model for a slug movement in the horizontal pipes. He has derived the pressure gradient by performing a momentum balance shown in equation (2-2). Results are also compared to data from previous research and his model

yielded an average error of 8%. A model for the slug movement through the 90 degree bent pipe has been also developed by Tay et al. [25].

$$\frac{dP}{dx} = 2 \frac{f_s}{D} \rho_s U_s^2 \frac{l_s}{l} + \frac{\tau_f S_f - \tau_i S_i}{A_f} \frac{l_f}{l} \quad (2-2)$$

After the condensate droplet is detached from the surface of the charge air cooler, most of the droplets coalesce into a flow in the direction of the fluid velocity gradient. However there is a portion of the droplets entrained into the charge air stream. This phenomenon occurs when an instability between the gas and the liquid stream surface exceeds a critical level [26,27]. A study presented in reference [26] has concluded that this is inherently a transient phenomenon. Chang-Mateau developed a model using the critical wavelength to calculate an entrainment velocity shown in equation (2-3) and an expression for the critical wavelength is shown in equation (2-4).

$$V_r = const(a \lambda_c)^{\frac{1}{2}} \quad (2-3)$$

$$\lambda_c = 2 \pi \left[\frac{\sigma}{a(\rho_f - \rho_g)} \right]^{\frac{1}{2}} \quad (2-4)$$

Koestel et al. [27] have proposed a way to calculate the interfacial wave growth using the Kelvin-Hemlholtz theory. Their model shown in equation (2-5) predicts the critical velocity and the onset of instability wave growth at a Reynolds number of 203 for an air-water system.

$$\frac{u_g \mu_g}{\sigma} \left(\frac{\rho_g}{\rho_l} \right)^{\frac{1}{2}} > 2.46 \times 10^{-4} \quad (2-5)$$

Another study [28] found that the onset of entrainment occurs when the volumetric air flux is larger than 40m/s and proposed a new correlation shown in equation (2-6) where Re_l is the liquid Reynolds number and P is defined by equation (2-7).

$$P = 135 Re_l^{-0.912} \quad (2-6)$$

$$P = \frac{j_{Gc} \cdot \mu_L}{\sigma} \quad (2-7)$$

There is a discrepancy between the two studies [27,28] mainly due to geometry differences of the test apparatuses and it causes an early onset of a turbulence. Therefore, Assad et al. [29] have found a correlation of the entrainment rate when $We_l^{1.25} Re_l^{0.25}$ is less than 10^6 . The various flow rates are tested to validate this correlation. Though the studies shown above do not completely explain the detailed droplet entrainment behavior, those provide a better understanding of the entrainment phenomenon.

2.1.3 Condensate Separator

In many industrial applications, separating a liquid or solid from a gas stream is very important. If it is separated efficiently, it can reduce cost save time and improve device performance. References [30,31] present the principal mechanisms of multiphase flow separation technologies such as a gravitation deposition, centrifugal separation, inertial deposition and diffusional interception.

The gravity deposition is the easiest type of separator. It uses the weight of the particles or droplets to be separated from the gas flow. The centrifugal separation is a more efficient approach than gravity separation. It uses a centrifugal force higher than the

drag force created by the gas flow, and includes devices such as a cyclone separator. The cyclone separator works with a solid, liquid and gas. It is widely used in the petroleum industry if the gas volume fraction is high [32]. The next approach is called the inertial deposition. When a gas flow passes through the obstacles such as the fibers or barriers, the particles or droplets lose their momentum and then are trapped in the obstacles or fall to the bottom. This last approach, the diffusional interception, usually applies for the separation of particles from aerosols with small particles (less than $0.1\mu\text{m}$).

Among the principal mechanisms of a liquid/solid and gas separation, vane separators are one of the technologies that use an inertial impaction to remove the liquids and solids from the gases. Such devices have a series of the wavy plates in the vessel. Some of the separators have hooks or blades on the corner of the wavy plate to improve the separation efficiency. This type of the separator can advantageously drain the liquid from the gas and minimizes re-entrainment of the liquid. In addition, because of its small size and high separation efficiency, it can be embedded in a vehicle [33]. When the droplets are carried through the vane gas-water separator, the water droplets tend to go straight so they hit the hooks or blades and accumulate on the wall. Therefore, thin liquid films accumulate on the wall and the droplets fall on the bottom of the separator. A sample sketch of vane separator is shown in Figure 2-2 [34].

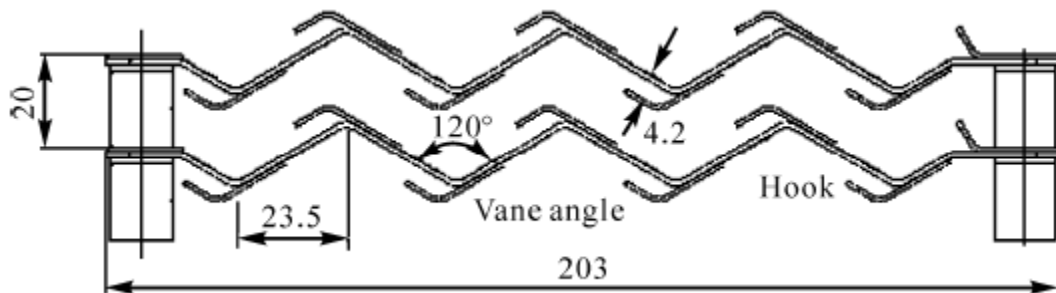


Figure 2-2. Sketch of vane separator – flow is left-to-right [34]

Nakao et al. [35,36] have researched the water droplet behavior passing through the vane gas-water separator. Their results have shown that most of large droplets (30-600 μm) are captured on the first and second hooks. However, smaller droplets (less than 30 μm) are not trapped well. Some researchers [34,37] have developed numerical models of the vane separator. However, those models neglect the secondary droplet breakup due to wall collisions, and show a calculation error of about 20%. Even if the droplet breakup is considered, the numerical calculations are carried out only at low inlet velocity of the water droplets, less than 10m/s [34,38] as compared to the range of interest for the CAC outlet of 10-15m/s. Therefore the prediction of pressure drop and separation efficiency for the high inlet velocities of the water droplets needs to be explored by analysis of the secondary water droplet breakup.

2.2 Water Injection

The application of water injection in combustion engines is not new. Water injection methods were recognized over a hundred years ago and applied during World War II to obtain more power from the aircraft engines. The usage of the water injection technology in gas turbines is still studied and in use up to now [39–43]. Also there is much research about water injection on internal combustion engines over the last 50 years, which is summarized in the next section.

2.2.1 Thermodynamic effects of water injection

Due to its high enthalpy of vaporization, injection of water into the air stream in the intake manifold or directly into the cylinder results in evaporative cooling of the charge and thus increases the density of the charge and potentially the air mass flow into the engine. This can translate to more fuel burning and allow for higher power from the engine. Bhagat et al. [44] performed a series of spray visualization experiments and engine simulation studies which indicated that direct in-cylinder water injection at 90 degrees before top dead center (BTDC) resulted in about 8% reduction in peak temperature at the end of compression compared to without water injection. Also, the decrease in temperature due to water evaporation reduces the temperature at the end of compression, thus resulting in lower end gas temperature and allowing the engine to operate at the MBT spark timing. Without the water injection, the engine would be knock limited under high load, low speed conditions.

Water, being a triatomic molecule, has a higher specific heat than air (which is mostly diatomic nitrogen and oxygen). The presence of water vapor in the combustion chamber increases specific heat capacity, assuming the same equivalence ratio [3], which results in lower combustion temperature and lower NO_x emissions. The presence of water vapor can lead to higher the specific heat capacity of the air charge as compared to CO₂ on mass basis which suggests the potential replacement of EGR with water vapor addition. Additionally, due to peak temperatures during combustion, the water molecules may dissociate into H and OH radicals. From experimental investigations by Wang et al. [45], the formation of NO is suppressed in the presence of such OH radicals.

2.2.2 Performance effects of water injection

Several studies have been conducted to determine the effect of water addition on engine performance. There are three methods used for water addition to the engine: fuel-water emulsion; intake manifold injection; and direct water injection into the cylinder.

Fuel-water emulsion technique is the method injecting water into the engine. An emulsion of water in fuel with stabilizing additives is defined as the emulsion fuel. Several previous studies using fuel-water emulsion have shown advantages of water injection on engine performance parameters. It has been shown that water in the fuel promotes atomization of fuel due to micro explosion of droplets [46–48]. In 1984, a fuel-water emulsion study for performance and emission control was done by Tsao et al. [49] on a single cylinder, four stroke, engine. The authors concluded that using unleaded gasoline containing 5, 10, and 15% of water by volume in a modified spark ignition engine gave both engine output and fuel economy improvement in the order of 10% as the water content in fuel was varied up to 15%. Introducing the water into the intake manifold by emulsion or injection did not make any difference in performance, which is consistent with the findings of Bratkov et al. [50] in regards to the antiknock effect of water. Besides, water-fuel emulsions as a technique to reduce emissions have been reported [51,52]. A blend of 20% of water by mass in a conventional diesel fuel was applied to a heavy duty diesel engine. The engine was tested over the Millbrook London Transport Bus (MLTB) cycle and the water-fuel emulsion offered up to 21% of NO_x reduction. At the steady state test condition, NO_x and PM emissions were reduced by 19% and 16%, respectively. Additional research conducted using fuel-water emulsions has shown the beneficial results of water addition [53–56].

Recently, BMW offered manifold water injection on their 2016 M4 GTS, which achieved higher fuel economy and more power compared to their previous 6 cylinder engine [57]. Advantages of intake manifold injection were demonstrated in 1950 by Porter [58]. Porter injected the alcohol-water mixture, 85% alcohol plus 15 % water (not mentioned vol. % or wt. %), compared to fuel and achieved a 30% of power increase by increasing compression ratio from 6.8:1 to 8:1. Peters et al. [59] examined numerically and experimentally the effects of injecting water into the intake manifold on the P-V diagram. The authors also report that water addition to the reactant mixture slows the combustion process, hence in order to maintain MBT spark settings, the timing must be advanced when using water-gasoline fuels. Lanzafame [60] and Brusca and Lanzafame [61] reported that “by simultaneous increase of volumetric compression ratio and water injected mass flow rate, measured Research Octane number (RON) increased from 70 to 93 and Motor Octane number (MON) from 64 to 90”. Also, a limitation of water injection was also observed in the literature. Nicholls et al. [62] showed in their theoretical analysis and experimental data for manifold injection that an increase of water injection beyond a water-fuel ratio of 0.75 results in a return to the original non-injection value of BMEP. Increases beyond about 1.25 results in diminished BMEP relative to the original case. In reference [63], Harrington observed a decrease of burn rate and increase of fuel consumption when adding water under normal operating conditions. Effect of intake manifold water injection on combustion was also discussed in different types of engine such as compression ignition engines [64–76].

Direct water injection means injecting water directly into the cylinder by using a second injector. The main advantage of this approach is controlling the water fuel ratio

and injection timing [77]. In 1944, Miller [78] tested direct water injection with a water fuel ratio 0.3 at 570 rpm and argued that the optimum angle of water injection is critical. Experiments on a direct water injection system by Lestz et al. [79] found that with constant spark operation, power deteriorates as the water to fuel mass ratio is increased due to the high latent heat of vaporization of water and to the water-induced slow-down of the combustion process. To compensate for slow combustion, the spark timing was readjusted to obtain maximum brake torque (MBT) for each operating condition with water injection. Water injection timing for the best performance is still controversial because it changes depending on fuel type, cylinder geometry and operating condition [73,80–87].

2.2.3 Emission effects of water injection

The major gaseous effluents coming out of gasoline direct injection engines are dinitrogen (N_2), water (H_2O), nitric oxides (NO_x), carbon oxides (CO_2 and CO) and hydrocarbons (HC). Several studies have shown that water addition affects to those exhausts gases.

NO_x , referring to the sum of nitric oxide (NO) and nitrogen dioxide (NO_2), is formed when nitrogen reacts with oxygen at high temperature and pressure conditions. Water injection by the following mechanisms reduces NO_x formation with: (1) the temperature reduction due to the charge cooling effect because of the latent heat of evaporation; (2) the increase in heat capacity of the mixture due to dilution of the charge by water vapor; and (3) the reduction in adiabatic flame temperature due to water dilution [62]. Experimental data obtained by Lanzafame [60] indicates nitric oxide reductions of

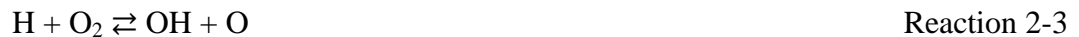
over 50% with water injection/fuel ratio in the range from 1 to 1.25. In a comprehensive study, Lestz et al. [79] established that with constant spark timing operation, power deteriorates due to water induced slower combustion; the spark timing has to be adjusted to MBT. After adjusting the spark timing to obtain MBT, there was a 50% reduction in NO_x without sacrificing power. With a direct water injection system, the NO_x reduction was dependent on the injection timing of water [79,85]. Overall, water injection is an effective method to reduce NO_x emission [45,55,63,65,66,68,70,80,82,88,89].

Unburned hydrocarbon emissions are emitted when fuel molecules do not burn or burn only partially in the engine. Partial burning can result because of crevice volumes, rich fuel-air ratio, or flame quenching [3]. Many studies (including [55,60,67,68,79]) confirmed increases in HC emission with water injection, which can be explained by reduction in-cylinder temperature because of water acting as a heat sink. There is a pronounced increase in unburned HC emissions for late water injection timings, but for earlier injection timings, the HC level reaches a peak and then decreases for larger water-fuel ratios. [79]. However, in reference [84] Mingrui et al. argues that HC emissions decrease by adding water because more complete combustion is achieved.

Carbon monoxide is a byproduct of incomplete combustion when carbon in the fuel is partially oxidized rather than fully oxidized to carbon dioxide. The percent composition of the exhaust gas made up of CO and CO₂ was essentially unaffected by water injection [45,63,68,83,89].

2.2.4 Chemical effect of water injection

Early studies of water injection effects on spark ignition engines suggested that the reason for reducing pre-ignition and knocking due to water injection was the internal charge cooling effect of water [90]. However, there are a relatively limited number of studies on the chemical reaction effects of water, because the chemical reactions are not easy to separate from the thermal effect, due to strong dependency of temperature. In reference [91], two percent increase in absolute humidity led to suppress on flame speed by ten percent. In addition, this reduction was three times higher than expected, considering the increase of heat capacity based on a simple calculation, presented in reference [92]. A possible mechanism has been introduced in references [93] and [94]. Water acts as a promoter for hydrogen-oxygen radical reactions. So by promoting the rate of chain branching, it lowers hydrogen atom concentrations through



Therefore, the auto-ignition can be promoted [46].

More research on the effect of water on combustion can be found. Shock tube experiments to identify the methane oxidation mechanism have been performed and oxygen atoms and hydroxyl radicals were observed by Bowman [95]. By adding 10 percent water vapor in the gas mixture in 1400K, hydroxyl radical was increased by 30 percent and oxygen atom concentration was decreased by 22 percent. Experimental data obtained by Le Cong and Dagaut [96] identified that the chemical effect of water on hydrogen-air and methane-air flames. They added 10%mol. of water to a jet-stirred

reactor and compared ignition delays and species concentrations. Water contributed to remove H via $\text{H} + \text{O}_2 + \text{M} \rightleftharpoons \text{HO}_2 + \text{M}$ reaction and $\text{H}_2\text{O} + \text{O} \rightleftharpoons \text{OH} + \text{OH}$ reaction. Researchers have studied change of the burning velocity of methane flames due to water addition, using experimental and numerical analyses [97]. Burning velocity was measured under fuel lean, stoichiometric, and fuel rich conditions with fixed temperature and pressure with and without water. They argued that the chemical effect of water is greater under lean and stoichiometric conditions than rich conditions.

2.2.5 Limitation of water injection

Despite the benefits of water injection described above, water injection creates penalties on combustion. Typically, boosted engines use a charge air cooler (CAC) after the boosting system, in order to reduce charge temperature for improved volumetric efficiency and reduced knock tendency. It should be noted that under high humidity conditions, the CAC-out charge may be at or near 100% relative humidity. Under this condition, water injected in the intake system will not evaporate. Instead, liquid water will enter the cylinder and evaporate during the compression stroke as the mixture pressure and temperature rise. At higher pressure, the heat of vaporization of water is reduced so there is less effect on charge temperature. Nonetheless, there will be some reduction in charge temperature and the change in charge composition and thus the water injection will still have a beneficial effect.

The net benefit of water injection on power and efficiency is difficult to predict. Knock limits occur under low speed, high load, and/or boosted conditions. How often those occur depends on the driving modes, ambient temperature and humidity, and many

other factors. We can conclude, however, that under customer relevant conditions there can be a significant increase in power and/or fuel efficiency through use of water injection.

As mentioned above, some authors found that water injection into the engine yielded a slowdown of combustion. In addition, as mentioned earlier, HC emission increased with water injection [63]. To maximize the benefits of water injection, the amount of injected water as well as combustion parameters such as spark timing should be carefully controlled. If this strategy is carefully implemented, water injection can give fuel economy improvements along with knock limit extension.

The production uses of a water injection strategy would need to include developing an efficient on-board diagnostic (OBD) strategy which ensures that a minimum level of adequate quality water is available, failing which, the engine control system should trigger conventional knock mitigating strategies. Other limitations include the need for a separate water reservoir, and perhaps developing anti-freeze systems to avoid water freezing during cold ambient conditions.

Chapter 3

Charge Air Cooler Condensation Management

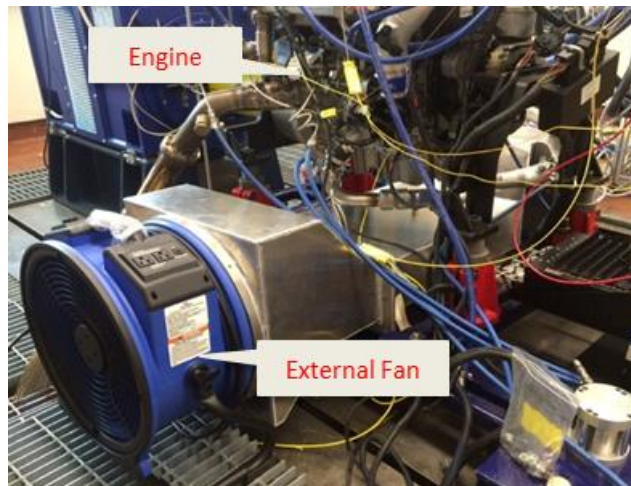
In this chapter, a 1-D condensation model to estimate the potential amount of water condensation and entrainment from a charge air cooler is presented. The model results of the 1-D condensation model and the 3-D computational model have been validated by experiments on an engine-dynamometer based test cell. The experiments were conducted to duplicate condensate issues and analyze abnormal combustion behavior, such as misfire and slowburn due to condensate ingestion. An approach to designing a unit to separate condensation in the flow from the charge air cooler while maintaining a low pressure drop is described. The design approach provided correlations of separator geometries versus separation and pressure drop performance. The study was developed using a 3-D computational model for analyzing charge air and condensation flow.

3.1 Experimental Setup

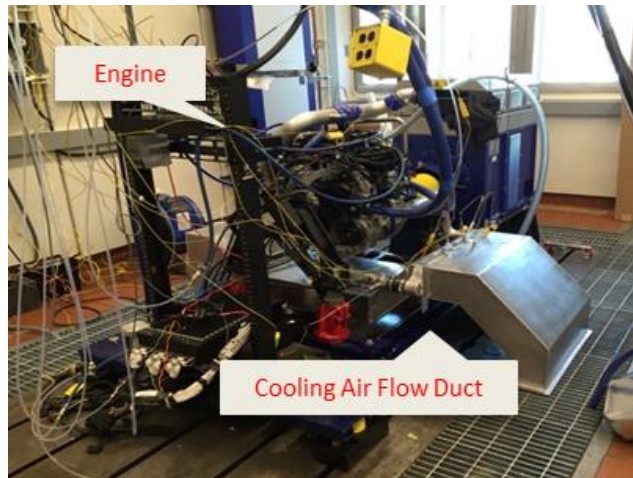
Engine dynamometer testing was carried out using a four-cylinder turbocharged gasoline direct injection (GDI) engine. The engine specifications are shown in Table 3-1. An air-to-air charge air cooler was fitted to the side of the engine. An external fan was used for the CAC cooling air flow. The intake air for the engine was supplied using a combustion air unit that allows the operators to control the temperature and humidity. Detailed setup photos are shown in Figure 3-1.

Table 3-1. Test engine specification

Displacement	1.596 L
Number of Cylinder	4
Bore / Stroke	79.0 / 81.4 mm
Compression Ratio	10:1
Maximum Power	133 kW @ 5700 rpm
Maximum Torque	250 N m @ 2500 rpm



(a)



(b)



(c)

Figure 3-1. Experimental Setup, (a) external fan for the cooling air, (b) the engine and cooling air flow duct, and (c) the combustion air for intake

The air-to-air charge air cooler (CAC) was used to cool down the charge air. The specification of the CAC is shown in Table 3-2. A test for the charge air cooler verification was done prior of the experiments. For the verification, a heat rejection per temperature differences and thermal effectiveness calculations were applied. The engine tests were done at two different conditions: 2000rpm, 13bar BMEP; and 3000rpm, 16bar

BMEP. The cooling air flow rate, cooling air temperature, CAC inlet temperature, CAC outlet temperature, a charge air mass flow rate, heat rejection per temperature differences, and thermal effectiveness are calculated using equations (3-1), (3-2), where:

- heat rejection Q in W,
- CAC outlet temperature T_{outlet} in K,
- CAC inlet temperature T_{inlet} in K,
- cooling air temperature $T_{cooling\ air}$ in K,
- specific heat of air c_p in J/kgK, and
- charge air mass flow rate \dot{m} in kg/s.

The results were compared with the data which were provided by the engine manufacturer as shown in Table 3-3 and

Table 3-4. The heat rejection per temperature difference obtained by the engine test was calculated to be 33.7W/K and 63.5W/K at the lower load and the higher load conditions respectively. Since the charge air flow rate in those conditions were out of range on the table, the values were obtained using an interpolation method, and 36.9W/K and 62.2W/K at the lower load and the higher load condition, respectively. In the same way, the thermal effectiveness from the engine tests were 95.6% and 89.5% at the lower load and the higher load conditions, and the values from the table were 92.1% and 86.2%. The percentage errors were less than 4% in the every case, except the heat rejection per temperature differences in the low load engine condition, 10% error. This is mainly due to a result of the interpolation method, because the change of the heat rejection per temperature difference does not follow a linear equation.

$$\frac{Q}{dT} = \frac{(150 - T_{outlet}) \times c_p \times \dot{m}}{125} \quad (3-1)$$

$$\text{Thermal Effectiveness} = \frac{T_{inlet} - T_{outlet}}{T_{inlet} - T_{cooling\ air}} \quad (3-2)$$

Table 3-2. Charge air cooler specification

Dry Mass	2.1kg
Charge Air Internal Volume	2.4L
Dimension	657mm L × 67mm W × 157mm H

Table 3-3. Heat rejection per temperature differences of CAC

	<i>Cooling Air Flow(m/s)</i>			
		<i>2</i>	<i>4</i>	<i>6</i>
<i>Charge Air Flow rate (kg/s)</i>	0.1	73	80	83
	0.2	110	131	140
	0.3	131	165	182

Table 3-4. Thermal effectiveness of CAC

	<i>Charge air flow rate (kg/s)</i>			
		<i>0.1</i>	<i>0.2</i>	<i>0.3</i>
<i>Cooling air speed at CAC face(m/s)</i>	1.7	0.70	0.52	0.41
	4	0.79	0.65	0.55
	7	0.84	0.71	0.62

To generate the condensation, high humidity air is needed as the intake air to the engine. A test cell combustion air unit was used to control the humidity level of the intake air. It is designed to supply a conditioned airflow at a fixed speed through a supply

duct. Unconditioned ambient air passes through an evaporator coil and a refrigeration system. The air is cooled and de-humidified before the air heater which re-heats the air to the desired temperature. After the air heater, the heated air is injected to a steam riser to re-humidify the air to the required level. This conditioned air passes through the blower and is delivered to the engine. The specification of the combustion air unit is shown in Table 3-5 and a schematic of the intake air flow is shown in Figure 3-2. There is a heat loss from the intake air as it passes from the combustion air unit to the engine cell. Therefore, a temperature and humidity sensor was located right before the engine intake, which was to adjust the temperature and humidity through the combustion air unit controller.

Table 3-5. Specification of combustion air unit

Temperature Range	15.5°C to 40.5°C dry bulb
Temperature Tolerance	±0.5°C
Humidity Range	20% to 95% RH; 13°C to 35°C dew point
Humidity Tolerance	±0.5°C dew point or ±2.0% RH, whichever is greater
Airflow	1926Nm ³ /h max

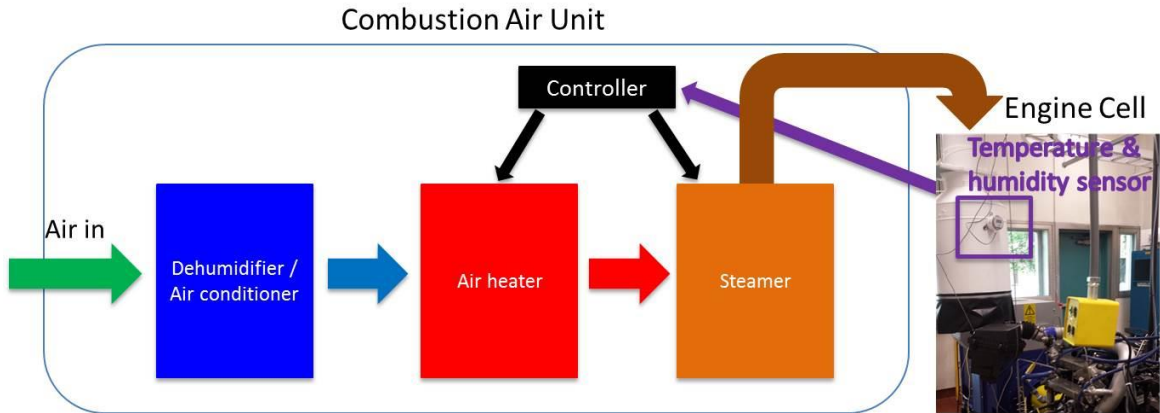


Figure 3-2. Schematic of intake air flow from the combustion air unit to engine

To duplicate a condition under which a vehicle is driven on the road, an external fan was used to provide a cooling air for the air-to-air charge cooler. To obtain high efficiency of the charge air cooler, a high cooling air flow rate is needed. For this reason, a cooling air flow duct was used to concentrate the cooling air. The cooling air flow rate is one of the important factors to predict the amount of condensation generated in the charge air cooler. Also, well distributed and steady air flow is needed to get a consistent result. Therefore, the cooling air distribution was examined using a hand held anemometer. A cross section of the outlet of the cooling air flow duct was divided into 10 sections as shown in Figure 3-3, and interpolated the sections. The cooling air speed was measured with and without the charge air cooler. Total average of the cooling air was 5.8m/s without the charge air cooler and 5.0m/s with the charge air cooler. However the distribution of the cooling air without the charge air cooler was not uniform; standard deviation was 1.87m/s without the charge air cooler and 0.45m/s with the charge air cooler, respectively, as shown in Figure 3-4.

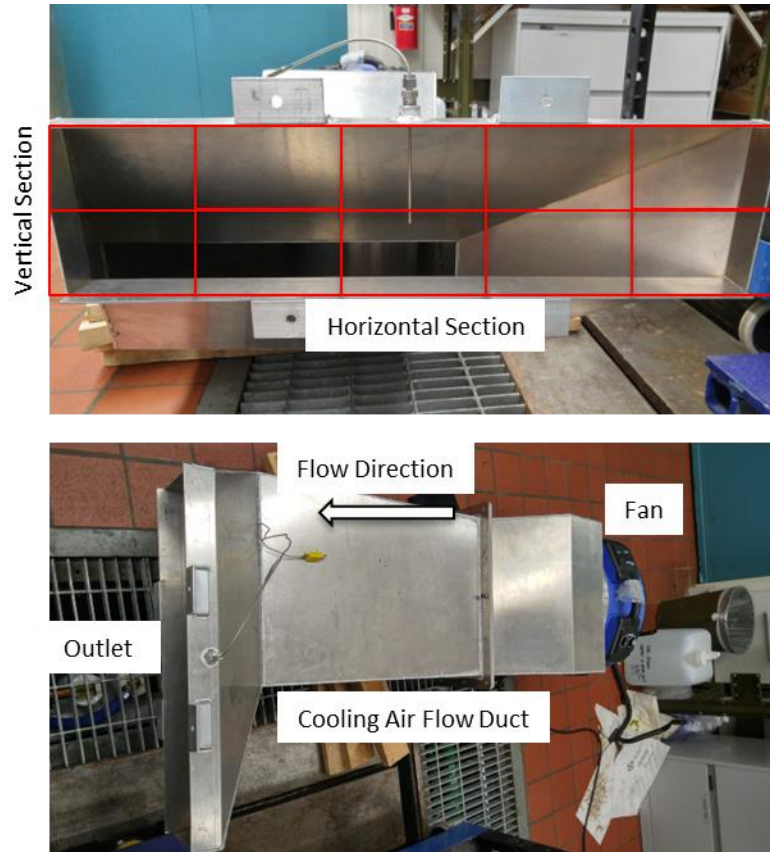
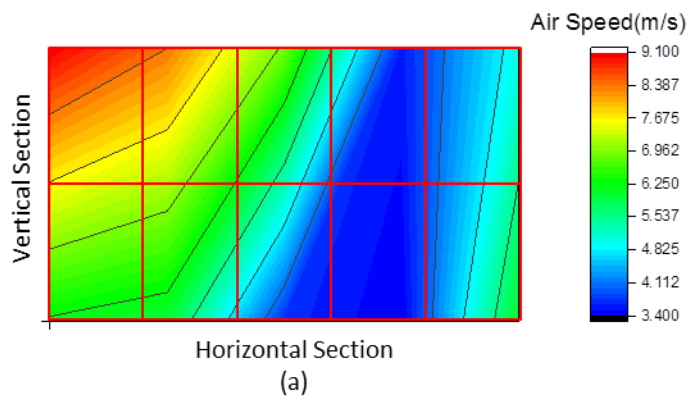


Figure 3-3. Cooling air flow distribution test setup



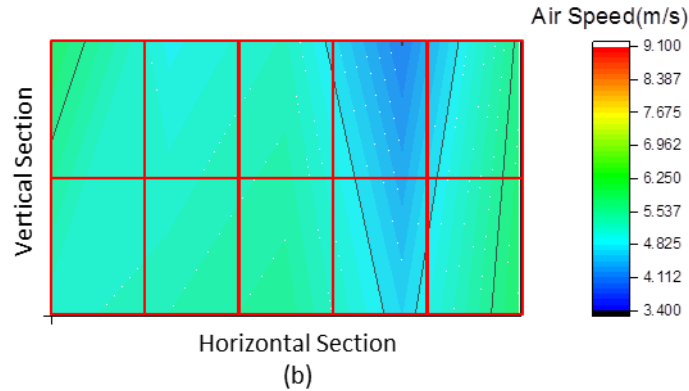


Figure 3-4. Cooling air flow distribution at the cross section of outlet of cooling air flow duct in m/s (interpolated) (a) without the charge air cooler, (b) with the charge air cooler

Exhaust composition is measured by an instrument bench, AVL i60, based on an FTIR spectrometer, to determine exhaust H₂O content. A Fourier transform infrared spectroscopy (FTIR) is a technique which is using an infrared to obtain a spectrum of a solid, liquid or gas. Molecules of each sample have their own unique resonant absorption frequency depending on the characteristics of their structure. When a beam of infrared light passes through the sample, if the frequency of the infrared light is the same as the resonant absorption frequency, the infrared spectrum of the sample can be recorded. Using a Fourier transform, the raw data is converted from time domain to the frequency domain. Now, the concentration of the emission can be analyzed using the FTIR measurement [98]. In the same way, H₂O concentration in the exhaust gas was measured and analyzed to determine the amount of water the cylinder consumes or generates in the combustion cycle. To calculate the amount of water added into the cylinder, the amount of water generated from combustion and the amount of water from the ambient air needs to be subtracted from the total amount of water recorded by the FTIR measurement. To estimate the amount of the water generated from the results of combustion, the air fuel ratio was obtained from equation (3-3). And the air fuel ratio was calculated using the

Brettschneider equation, shown in equation (3-4), where gas concentration in % volume $[XX]$, atomic ratio of hydrogen to carbon in the fuel H_{cv} , atomic ratio of oxygen to carbon in the fuel O_{cv} , number of carbon atoms in each of the HC molecules, n [99]. After the rejection the amount of water generated from the combustion and the amount of water the ambient air has, the amount of water additionally consumed in the cylinder was counted by integration of over the certain period of time. A schematic diagram of the FTIR analysis is shown in Figure 3-5.

$$\lambda = \frac{AFR}{AFR_{atoich}} \quad (3-3)$$

$$\lambda = \frac{[CO_2] + \left[\frac{CO}{2}\right] + [O_2] + \left[\frac{NO}{2}\right] + \left\{ \left(\frac{H_{cv}}{4} \times \frac{3.5}{3.5 + \frac{[CO]}{[CO_2]}} \right) - \frac{O_{cv}}{2} \right\} \times ([CO_2] + [CO])}{\left(1 + \frac{H_{cv}}{4} - \frac{O_{cv}}{2}\right) \times ([CO_2] + [CO] + (n \times [HC]))} \quad (3-4)$$

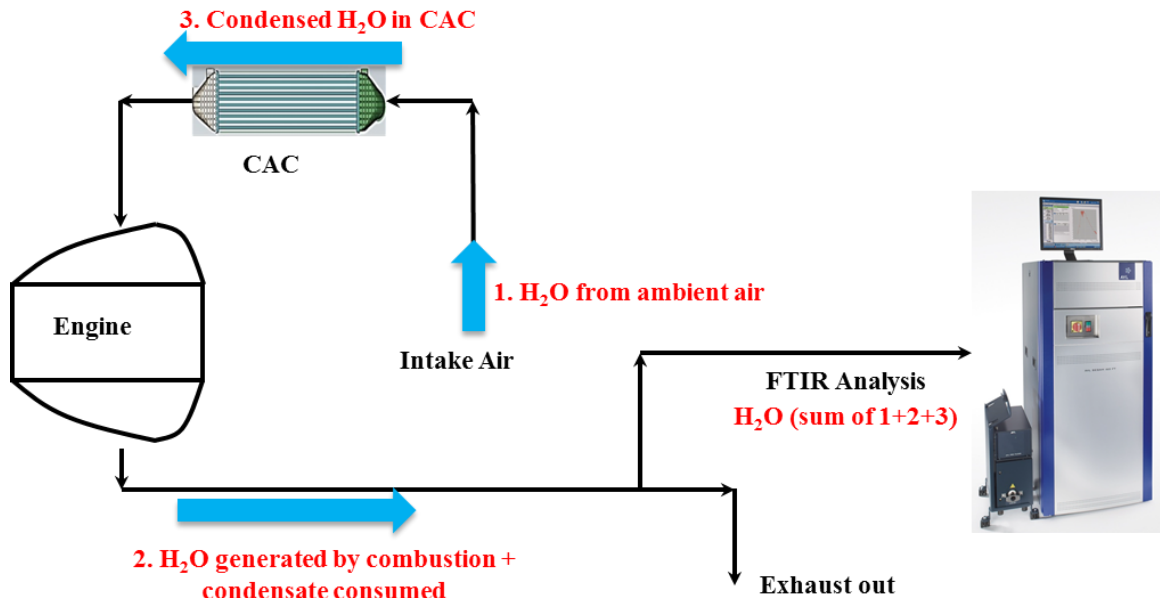


Figure 3-5. Schematic diagram of FTIR analysis

3.2 Charge air cooler condensation model validation

This section presents a test result to predict water condensation in the charge air cooler using the condensation model described in Appendix A. There are two parts to the model: a 1D phase change heat exchanger model for the air-water vapor mixture; and a transient entrainment model for the liquid water phase.

The amount of condensate in the charge air cooler is determined by a combination of several conditions, such as intake air temperature and humidity, charge air temperature, flow rate and pressure, cooling air temperature and flow rate. The condensation region over the engine operating range is calculated by the model described in Appendix A, and is shown in Figure 3-6. Test conditions are described in Table 3-6.

- At low loads, the boost is low enough that water does not condense
- At high loads, the large charge air flow exceeds the cooling capacity of the CAC so the charge air remains too hot for water condensation
- In between, significant rates of water condensation can occur

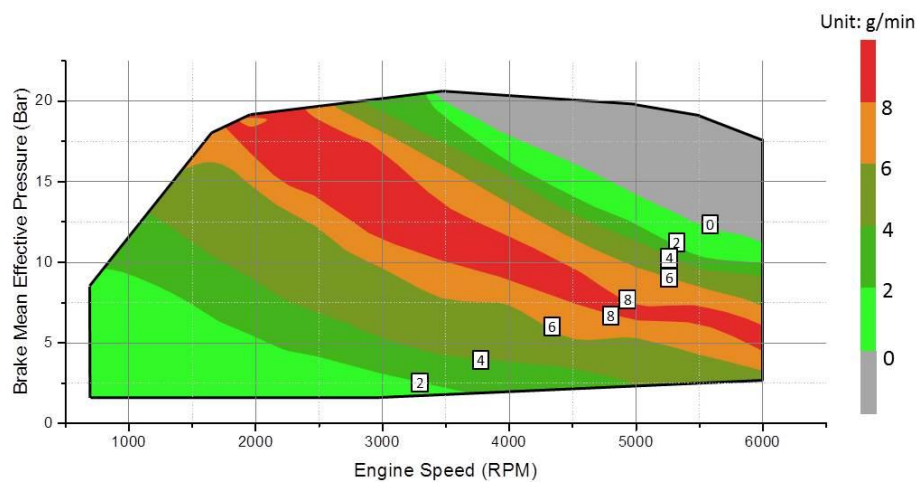


Figure 3-6. Condensation region. Color contours indicate the rate of liquid water condensation in grams of water per minute

Table 3-6. List of test conditions

Intake Air Temperature	33°C
Intake Air Humidity	70%RH
Cooling Air Temperature	26°C
Cooling Air Flow Rate	0.6kg/s

Different conditions were applied to evaluate the experimental results and compare to the amount of condensate predicted by the model. The experiments were conducted with four air mass flow rates of the engine intake air, 0.021kg/s, 0.031kg/s, 0.041kg/s, and 0.053kg/s. Equivalent engine conditions for each air mass flow rate are shown in Table 3-7. All experiments were carried out with 89%RH \pm 3 at 36.5°C \pm 0.5 of the intake air, which was controlled by the test cell combustion air unit. The CAC cooling air was controlled by an external fan operated at a maximum flow rate of 0.2kg/s, 27°C \pm 1 by an air controller at the test cell. Commercial premium gasoline fuel (RON99, MON90, E10) was used in these experiments. The detail of the fuel properties is shown in Appendix B.

Table 3-7. Equivalent engine conditions for air mass flow rate

<i>Mass Flow Rate(kg/s)</i>	<i>Equivalent Engine Condition</i>
0.021	2000rpm/7.8bar BMEP
0.031	2000rpm/12.5bar BMEP
0.041	2500rpm/12.6 bar BMEP
0.053	3000rpm/13.3 bar BMEP

The engine was operated for 10 minutes at each speed and load point. The weight of the charge air cooler before and after the test was measured to obtain the amount of condensation generated during the test period.

Figure 3-7 shows the amount of condensation measured at four different air mass flow rates for the engine and for the model calculations. For each calculation, measured engine data such as a charge air inlet temperature and pressure, and a charge air mass flow rate were applied to the model. All test points were repeated three times to analyze the results of the experiment and the error of the model calculation. The measurement of the amount of condensation was made in two separate steps: the amount of condensation remained in the CAC; and the amount of condensation flow into the cylinder. To obtain the amount of condensation remaining in the CAC, the CAC weight was measured before and after each test and subtracted. To measure the amount of condensation flow into the cylinder, the Fourier transform infrared spectroscopy (FTIR)-based exhaust analysis system was used. The total H₂O concentration of the exhaust gas is the sums of water generated by combustion, water contained in the ambient air, and condensate. The amount was obtained by subtracting combustion water from the measured total water. In each experimental condition, the error between the experimental result and the model calculation is less than 10%.

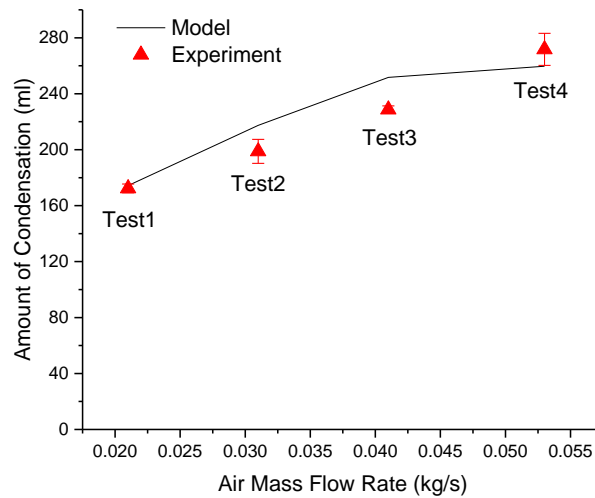


Figure 3-7. Comparison of the amount of condensation between model calculations (line) and experiment results (triangles)

3.3 Tip in test and slowburn / misfire

3.3.1 Experiment setup

The following experiments are to reproduce a field issue due to the condensation entrainment to the cylinder and an analysis of the amount of condensate effect to a combustion behavior, such as the misfire and the slowburn. The misfire event is defined as IMEP of the cycle is less than 0.5 bars, and the slowburn event is defined as IMEP of the cycle is less than 70% of IMEP at normal condition. Moreover, the condensate carried into the cylinder at different engine conditions was examined using the 1.6L GDI turbo engine, as shown in the previous section. First, a known amount of water, 100ml, 150ml, and 200ml was applied by pouring it into the CAC at three different tip-in engine conditions to understand how the engine reacts to different amounts of condensate. By applying a known amount of water, the test can be repeated with same amount of water,

and in each test, we do not need to wait a certain period time to accumulate the condensate in the charge air cooler. The engine conditions were set to 2500rpm/9.5bar BMEP/28% pedal position, 2750rpm/11.6bar BMEP/33% pedal position, or 3000rpm/14.1bar BMEP/40% pedal position. The engine was operated and maintained for 5 minutes at 2000rpm/7.8bar BMEP condition to obtain a steady state. We confirmed that with 2000rpm/7.8bar BMEP condition, water in the CAC does not get transported into cylinder with the charge air. After five minutes, a sudden acceleration was applied by rapid transition to one of the three conditions noted above. The engine was held at this condition for 20 seconds to carry the condensate within the charge air into the cylinder, and then the engine returned to 2000rpm/7.8bar BMEP for 60 seconds. The engine speed and load profile is shown in Figure 3-8.

To measure the amount of condensate consumed in the cylinder, FTIR analysis as explained in previous section was applied. The remaining condensate inside of the charge air cooler and a connecting pipe were measured after the experiment for comparison. The detail of the procedure is shown in Figure 3-9. The condensation inside of the charge air cooler was generated with the intake air temperature and humidity controlled by the test cell combustion air unit. The humidity was controlled to 76%, 81%, 84%, and 90% RH at 35°C. The engine tip in condition was chosen to be 3000rpm/14.1bar BMEP, since it was the worst case shown in previous tests. Similar to the previous setup, the engine was operated for 10minutes, in this case at 2000rpm/7.8bar BMEP condition, and then tipped in for 20seconds and back to the cruise condition. Because the exact amount of condensation cannot be predicted before each test run, the charge air cooler weight was measured before and after the test and the differences obtained for counting the amount

of condensate retention inside of the charge air cooler core. This amount was added to the amount of condensation transferred from the core during the tip-in which is the combined amount of condensate collected from the drain valve at the charge air cooler and the connection pipe, and consumed by the cylinders. This is illustrated in Figure 3-10. In the next of these two sets of experiment, a comparison is made to investigate the differences between the manually added water into the CAC and the naturally generated condensate tests condition.

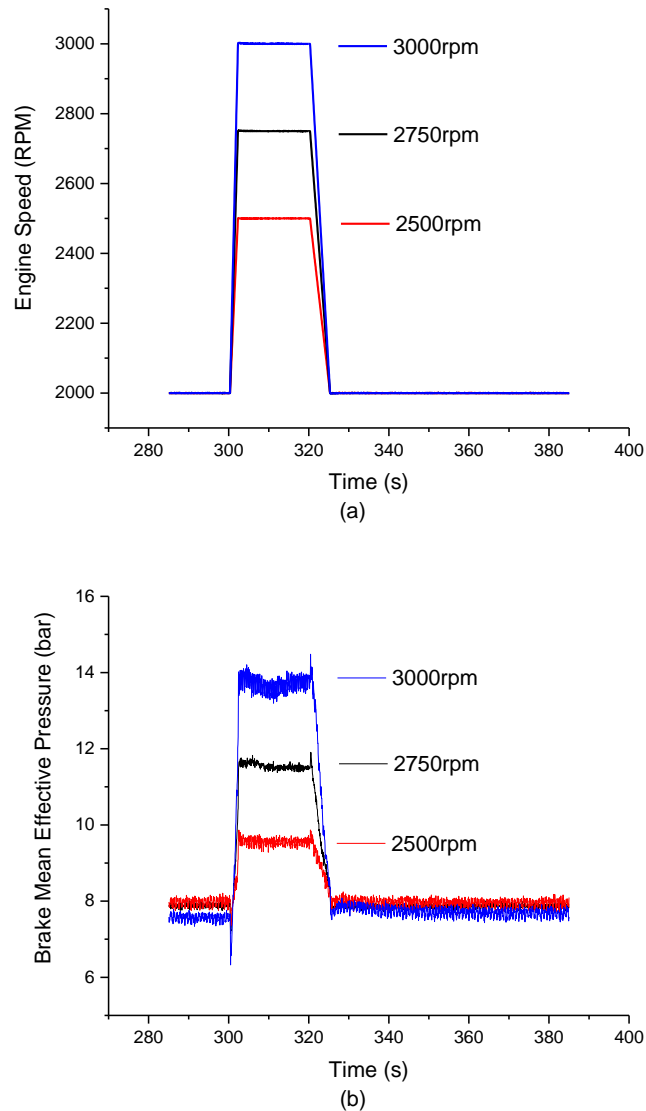


Figure 3-8. Test condition (a) engine speed(RPM), (b) brake mean effective pressure(bar)

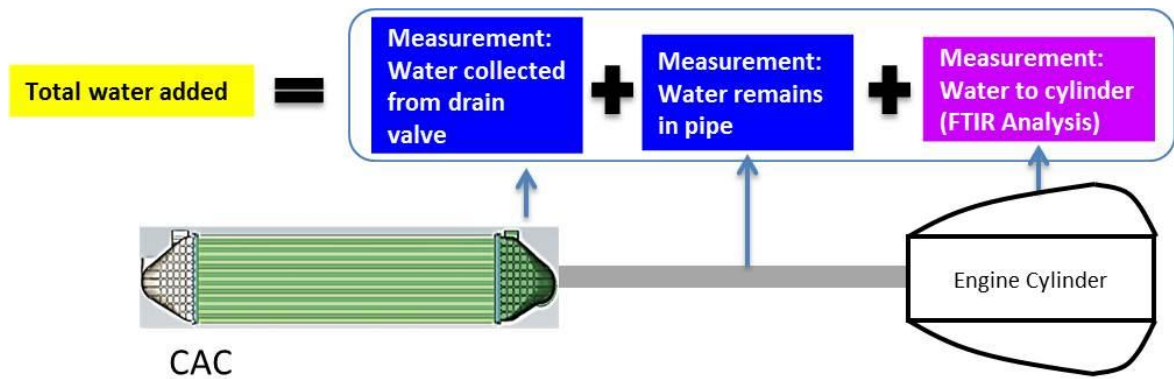


Figure 3-9. Schematic of experiment procedure in case of the known amount of water added

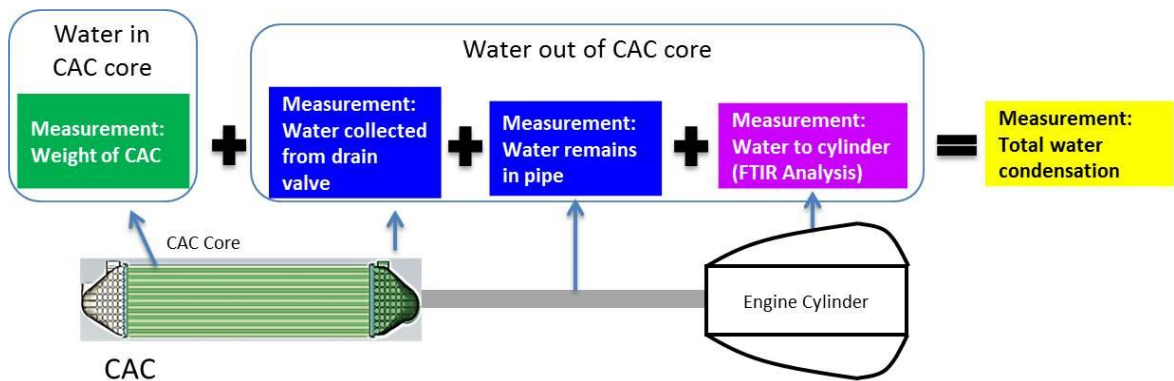


Figure 3-10. Schematic of experiment procedure in case of the generated condensation with high humid air

3.3.2 Experiment results; added water in the charge air cooler

Figure 3-11 shows a change of the maximum water mass fraction, normalized by total fluid mass intake to the engine cylinder based on the FTIR analysis of exhaust by three different amounts of water addition and three different engine tip-in conditions. With 2500rpm and 28% of a pedal position no matter of the amount of water maximum water concentration of exhaust does not change. From 2750rpm and 33% of pedal

position, the added water flow was started into the engine and gradually increased. Obviously, when the engine was running 3000rpm and 40% of pedal position, more water can be carried to the cylinder than at lower engine speed and load. Depending on the amount of water flowing into the cylinder, a higher number of slowburn and misfire events were observed. As shown in Figure 3-12 and Figure 3-13 Total 492 cycle, on average 46.7 cycles of slowburn were observed with 200ml, 2750 rpm and 33% of pedal position, 155.5 cycles of slowburn and 1.75 cycles of misfire were observed with 150ml, 3000rpm and 40% of pedal position. As a worst case, 256 cycles of slowburn and 21 cycles of misfire were measured with 200ml, 3000rpm and 40% of pedal position.

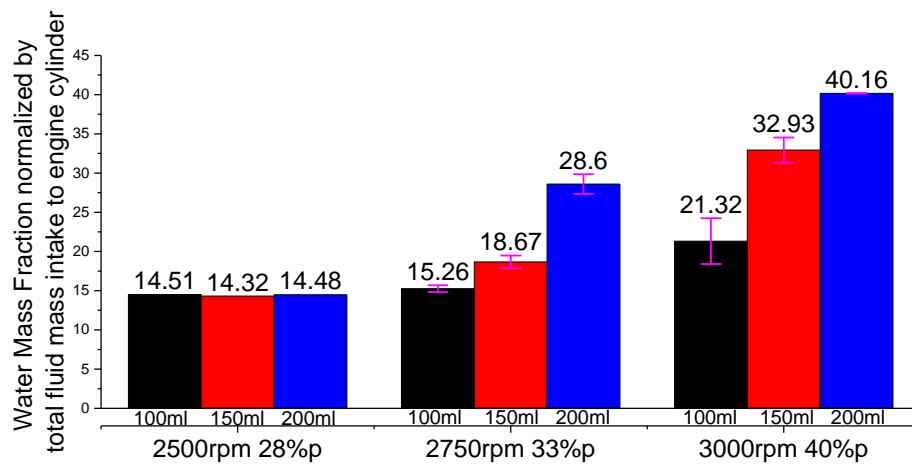


Figure 3-11. Maximum water mass fraction normalized by total fluid mass intake to engine cylinder (from FTIR analysis)

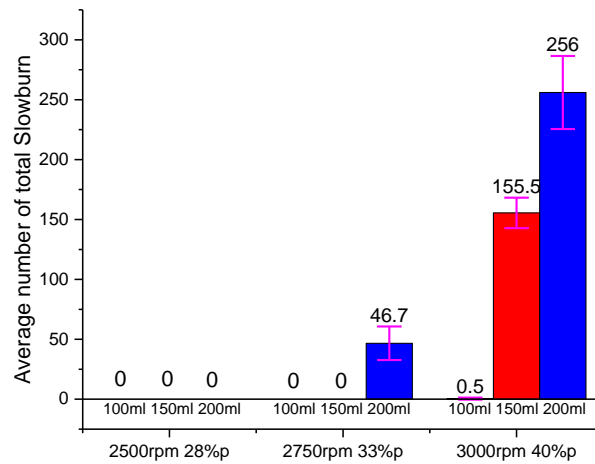


Figure 3-12. Average number of slowburn event

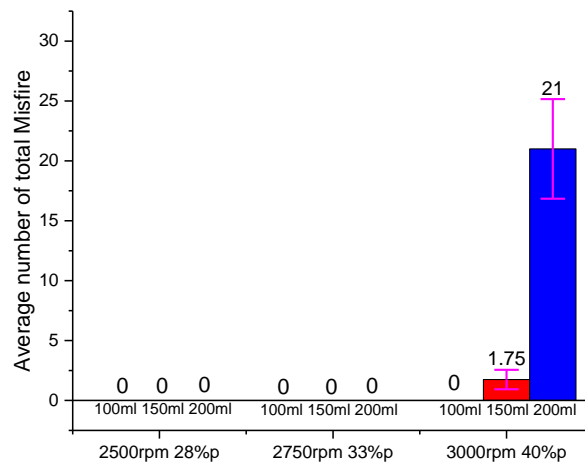


Figure 3-13. Average number of misfire event

3.3.3 Experiment results; generated condensation with humid air

In Figure 3-14, a total expected amount of condensation by the 1-D condensation model presented in Appendix A is compared with the actual measurement by the experiment. Some unaccounted amount of water resulted during the experiment and it is assumed that the difference is because some amount of condensate remains in the

connection pipe and intake manifold that cannot be completely collected, along with error in the 1-D condensation model and FTIR analysis error. The water concentration in error in engine exhaust is shown in Figure 3-15. Comparing case1 and 2, the maximum water concentrations are similar but case 1 shows a longer period time of water entrainment. Table 3-8 shows the number of slowburn and misfire events measured in each case of the engine operation.

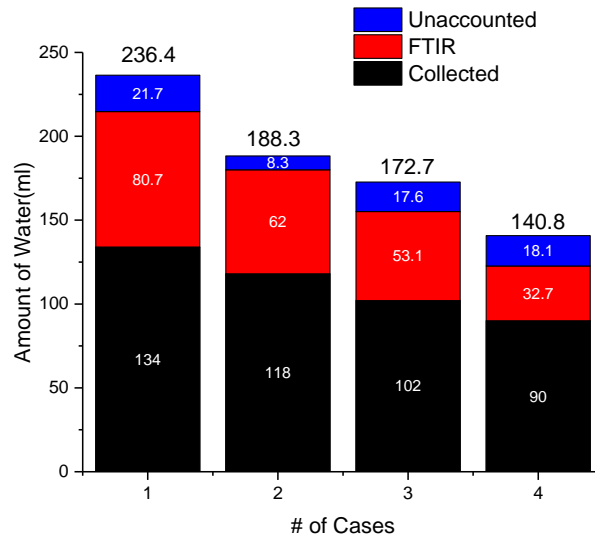


Figure 3-14. Total amount of water condensed (model) and measured amount of water(exp)

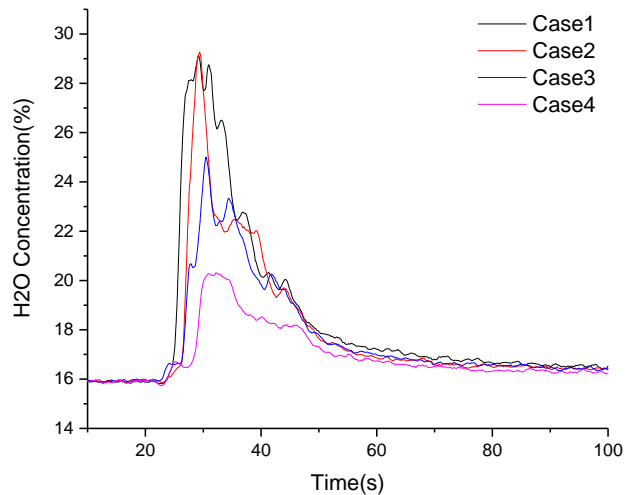


Figure 3-15. H₂O concentration measured by exhaust during tip-in transient

Table 3-8. Number of slowburn and misfire events

CASE	%RH (@35°C)	# of Slowburn					# of Misfire				
		Cyl 1	Cyl 2	Cyl 3	Cyl 4	Tot	Cyl 1	Cyl 2	Cyl 3	Cyl 4	Tot
1	90	58	0	2	115	175	0	0	0	1	1
2	84	35	0	1	55	91	0	0	0	1	1
3	81	12	0	0	18	30	0	0	0	0	0
4	76	0	0	0	0	0	0	0	0	0	0

3.3.4 Experiment results; comparison

To compare the water ingestion between manually added water to the charge air cooler and generated condensate, two cases for each test condition are chosen and compared. Case 1 and 3 are the cases of generated condensation which are case 1 and 4 in section 3.3.3. Case 2 and 4 are the cases of manually added water into the charge air cooler which are cases of 150ml and 100ml of water addition in section 3.3.2. Case 1, 2 and case 3, 4 are matched similar amount of water ingested to the cylinder as shown in Figure 3-16. In Case 2, 4, 70% of water was introduced at 14s and 19s after the tip in, but in Case 1, 3, 70% of water was introduced at 21s and 30s after the tip in, shown in Figure 3-17. The real condensation cases (Case 1, 3) had more water left in the CAC than the manual water addition cases (Case 2, 4) after tip in. The main reason for the differences in the water condensation results is that the extra force to detach the condensation from the inner matrix of the charge air cooler was not needed. When the water was manually added into the CAC, the water was sitting on the bottom of the charge air cooler, not inside of the matrix.

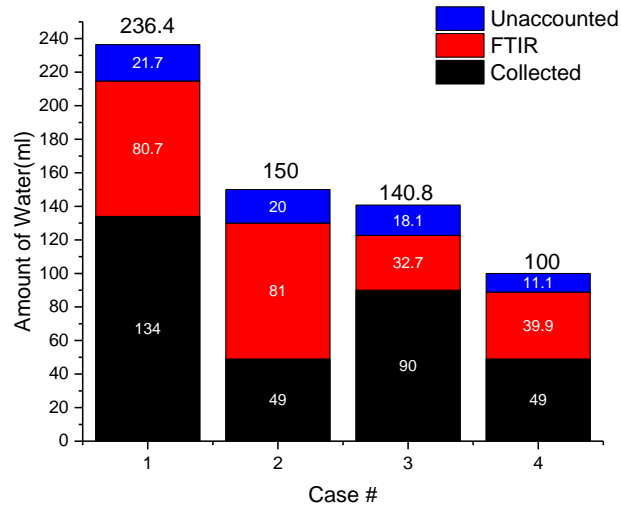


Figure 3-16. Total amount of water condensed (model) and measured amount of water(exp)

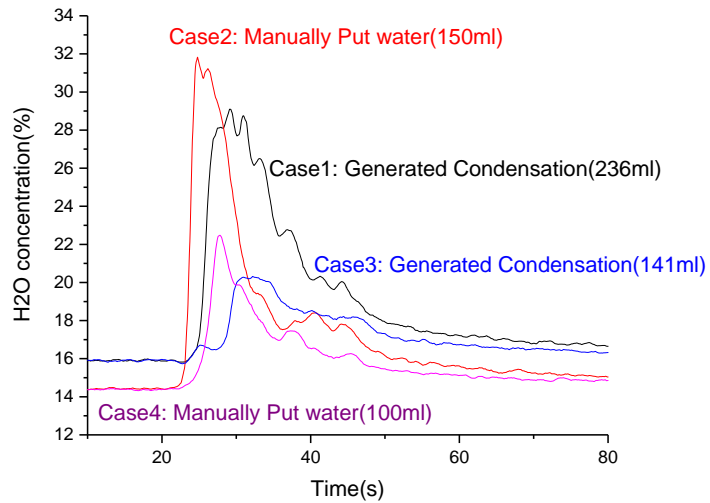


Figure 3-17. H₂O concentration measured in the engine exhaust

3.4 Condensate separator

3.4.1 Numerical calculation setup

Two different approaches were pursued for the pressure drop simulation and the separation efficiency simulation: the pressure drop calculation is tested as a single stream of continuous air; while the separation efficiency calculation has two phase flow - a continuous air flow with dispersed water droplets. In most engine operating conditions, the flow of condensation water droplets in the charge air can be ignored except in the high humidity intake air conditions.

To predict the pressure drop over the flow regime of the separator, the continuity, energy, and momentum equations were solved as governing equations for the air flow. The turbulence model was chosen as the standard k - ϵ model. To calculate the separation efficiency, a calculation of dispersed water droplets was adapted to the Lagrangian particle tracking model in ANSYS CFX®. This model tracks individual water droplets from the inlet of the separator through a final destination such as the outlet or wall of the separator. The assumptions applied in the calculation are shown below;

- The air flow was not affected by the water droplets, while the water droplet movement is controlled by the air flow.
- Water droplets were considered to be solid spherical particles because the density of water droplets is much larger than air [100].
- Three fixed droplet sizes of 100 μ m, 500 μ m, and 2mm which represented fine, average and coarse sized droplets, were assumed and the separation efficiency was obtained by averaging them (assuming the three droplet sizes are equally distributed).
- Temperature of air and water do not change.

- Water droplets sitting on the wall surface were counted as collected.
- Water droplets were injected in the normal direction to the inlet surface and uniformly distributed.
- Thickness of wall is 1mm.
- The material of the separator is aluminum.

The drag and buoyancy forces are calculated by ANSYS CFX® Solver. For numerical calculation, more parameters such as a surface tension coefficient, a wall film interaction, and number of droplets for the particle tracking model have been carefully selected.

One of the design goals is that the separator should be sufficiently small to fit in a vehicle. Thus the outer dimensions of the separator are designed as a rectangle 64-82 mm W×100 mm L×76 mm H because the outlet of the charge air cooler has a 60.325 mm inner diameter. The geometry is defined by the angle of plate, the air path width, the blade length, the blade width, and the number of air paths. Figure 3-18 shows configurations of the separator. In order to observe de-coupled effects of these configurations, a number of combinations of the angle, the number of air paths, the blade width, the blade length, and the air path width were simulated. The geometry of the separator was created using Autodesk Inventor 2015, and detailed dimensions are shown in Table 3-9.

Table 3-9. List of geometrical dimensions of the separator

<i>Case</i>	<i>Air path Width (mm)</i>	<i>Blade Length (mm)</i>	<i>Blade Width (mm)</i>	<i>NO. of Air Path</i>	<i>Angle of Plate(°)</i>
1	16	10	9	2	120
2	12	10	9	2	120
3	20	10	9	2	120
4	16	5	9	2	120
5	16	10	4	2	90
6	16	15	9	2	120
7	16	10	12	2	150
8	43	10	9	1	120
9	7	10	9	3	120
10	11	10	9	2	90
11	19	10	9	2	150
12	16	10	13	2	180
13	20	10	9	2	180
14	62	0	0	1	180
15	16	20	9	2	120

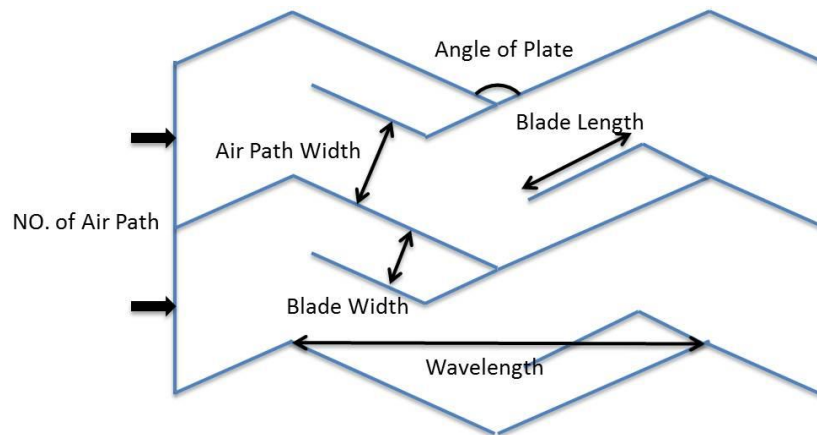


Figure 3-18. The separator configurations

Meshes were created using ANSYS Meshing 17.1. A mesh sensitivity test was performed on two different mesh sizes for the case 1-7. So a total of nearly 3 million nodes and 5 million elements were applied throughout the simulation.

As boundary conditions for the calculation, the mass flow rate of the charge air was applied for the inlet condition, and a static pressure was applied for the outlet condition on both the pressure drop and the separation efficiency cases. Specific engine conditions were selected based on actual vehicle speed and corresponding mass flow rate, and the charge air cooler outlet pressure was obtained by actual engine testing. The detailed inlet and outlet boundary conditions are presented in Table 3-10. For the calculation of the separation efficiency, the test conditions assumed that the vehicle is in a transient condition such as a highway entry. Therefore, the initial conditions of the calculation were determined for engine conditions of 2000rpm, 8 bar BMEP. The air density and dynamic viscosity were automatically calculated based on the charge air outlet pressure and temperature obtained by the engine experiments.

Table 3-10. Separator boundary conditions and equivalent engine conditions (Inlet: mass flow rate, Outlet: pressure)

<i>Pressure Drop Simulation</i>		
<i>Engine Condition</i>	<i>Mass Flow Rate(kg/s)</i>	<i>Pressure (kPa)</i>
2000rpm, 8 bar BMEP	0.021	20
3000rpm, 15 bar BMEP	0.053	50
6000rpm, 16.5 bar BMEP	0.160	210
<i>Separation Efficiency Simulation</i>		
<i>Engine Condition</i>	<i>Mass Flow Rate(kg/s)</i>	<i>Pressure (kPa)</i>
3000rpm, 15 bar BMEP	0.053	50
4500rpm, 19 bar BMEP	0.130	210
6000rpm, 16.5 bar BMEP	0.160	210

To establish a convergence criteria, three different root-mean-square (RMS) residuals (1×10^{-5} , 5×10^{-5} , and 1×10^{-6}) were applied to confirm that the results were the same. Therefore, all other simulations used on RMS residual of 1×10^{-5} to minimize execution time. All steady state simulations had a maximum of 300 iterations, and completed as soon as the residual satisfied the convergence criteria. In the case of transient simulation for the separation efficiency calculations, the time step has been chosen to 1×10^{-5} s by the RMS courant number from the CFX software [101]. Therefore the Courant number should be within the range of 0.5-1 for high accuracy results. Five iterations were performed within a single time interval.

3.4.2 Numerical calculation results

Simulation results were carried out for the pressure drop and the separation efficiency through the charge air gas / water condensation separator. The pressure drop due to each geometric factor and the separation efficiency are shown below.

The effect of total air path width on pressure drop is shown in Figure 3-19. Total air path width is calculated as the air path width multiplied by the number of air paths. Case numbers 1, 2, 3, 8, and 9 are compared. As the total air path width increases, there is less energy loss of contraction, thus reducing the pressure drop. The next calculated results are the effect of the blade lengths shown in Figure 3-20. The results show that increasing the length of the blade does not significantly affect the pressure drop, as seen by comparing the results from case numbers 1, 4, 6, and 15.

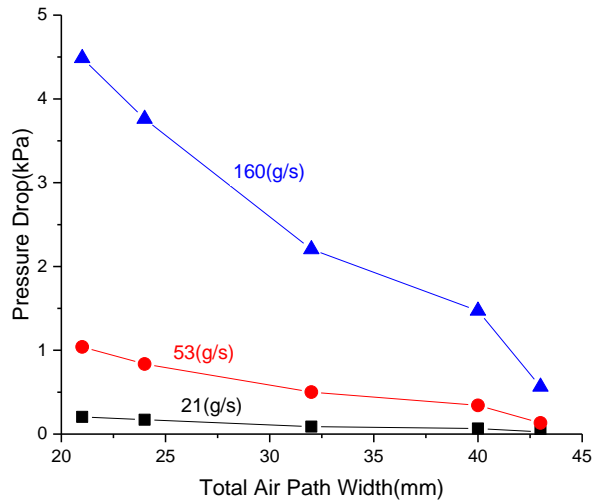


Figure 3-19. Effect of total air path width on pressure drop

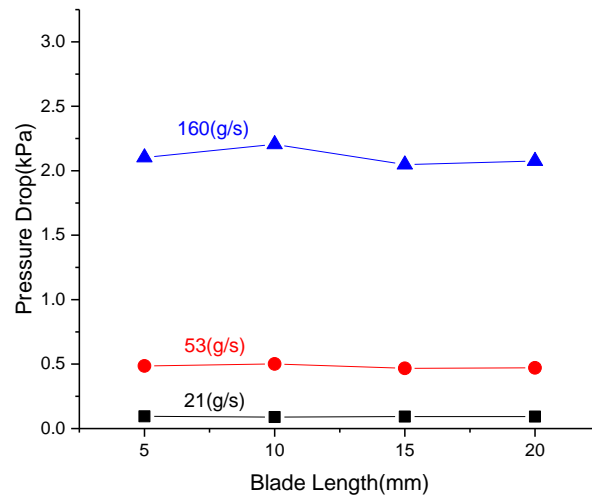


Figure 3-20. Effect of blade length on pressure drop

Figure 3-21 through Figure 3-23 show the influence of the number of air paths and the plate angles. Increasing the number of air paths at a constant total air path width increases the pressure drop. For the angle of plate effects with the fixed blade width in Figure 3-22, smaller angles have higher pressure drop but there is no significant difference between 150° and 180° . Those two cases are due to similar air path width and geometric constraints. In contrast, a comparison of the effect of angle of plate on the pressure drop with respect to the fixed air path width is given in Figure 3-23. In this case, the pressure drop for case 7, 150° angle of plate, represents the lowest pressure drop and increases again for case 12, 180° angle of plate. Since the case 12 has wider blade width than for case 7, the energy loss due to air swirl is larger.

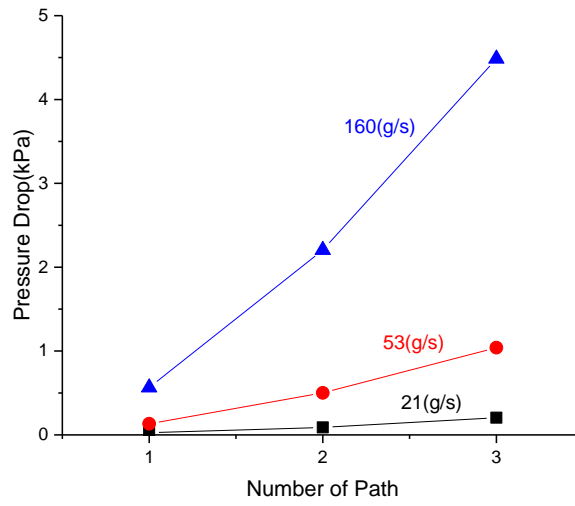


Figure 3-21. Effect of number of air path on pressure drop

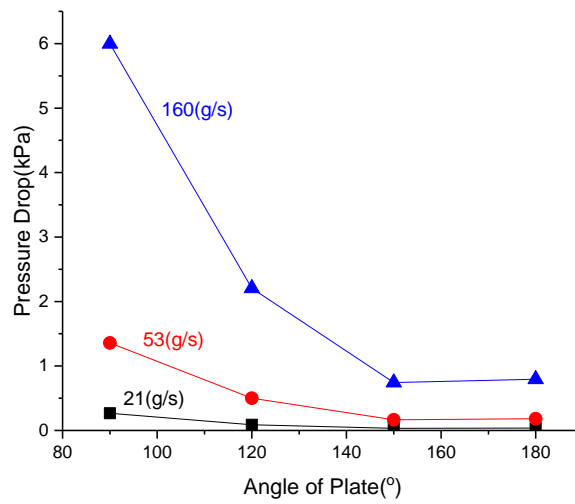


Figure 3-22. Effect of angle of plate on pressure drop with fixed blade width

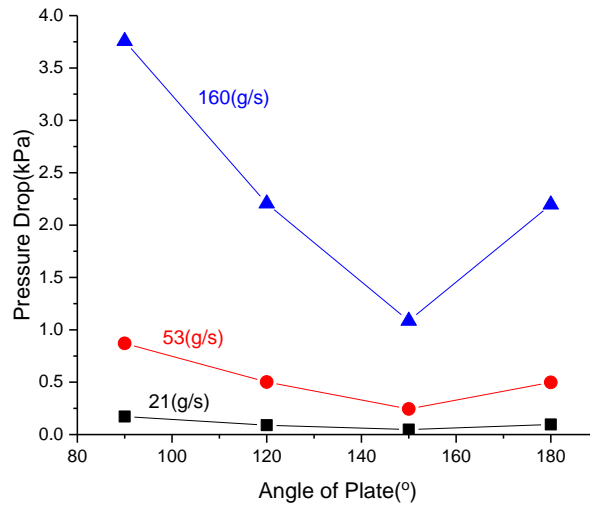


Figure 3-23. Effect of angle of plate on pressure drop with fixed air path width

The effects of the ratio of open path width on the pressure drop and the separation efficiency were examined. Open path width is defined as the size of air path which the air can pass straight from the inlet side to the outlet side of the separator as illustrated in Figure 3-24. Ratio of the open path width is calculated as the open path width over the total air path width. The larger this ratio, it has the wider the open path. If the air path is overlapped, it is defined that the ratio is negative. So the higher the negative value, the more the air path is overlapped. Therefore, as shown in Figure 3-25, the lower the ratio of open path width, the greater the charge air pressure drops across the separator. The separation efficiency associated with the ratio of open path width is shown in Figure 3-26. As can be seen from the graph, the separation efficiency increases with decreasing of the ratio of the open path width from 1 to 0. If the ratio of the open path is negative, the calculated separation efficiency result is 100%. Moreover, a bigger droplet size (2mm) shows better separation efficiency than a smaller droplet size (0.1mm). There is no

significant relationship to other geometric parameters such as the total air path width, blade width, blade length, number of air paths, and angle of plate.

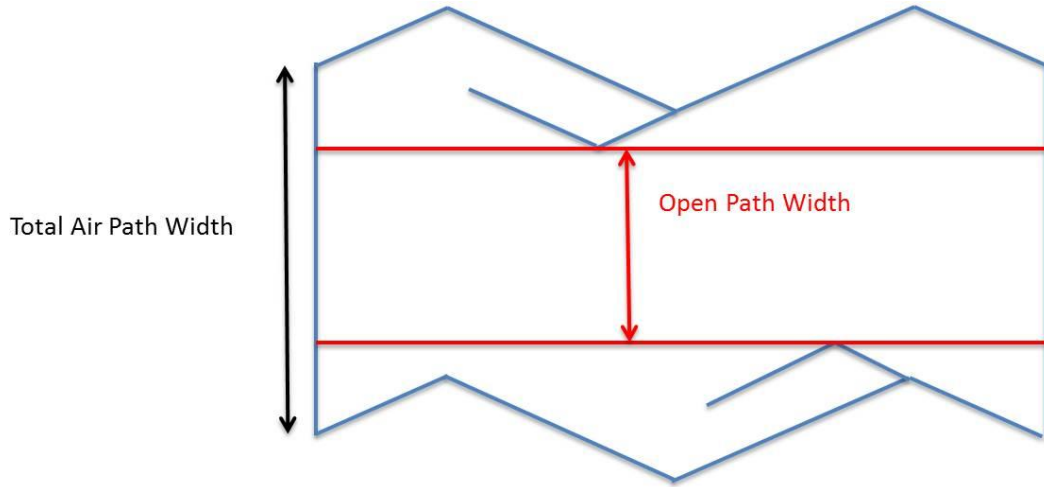


Figure 3-24. Definition of ratio of open path width

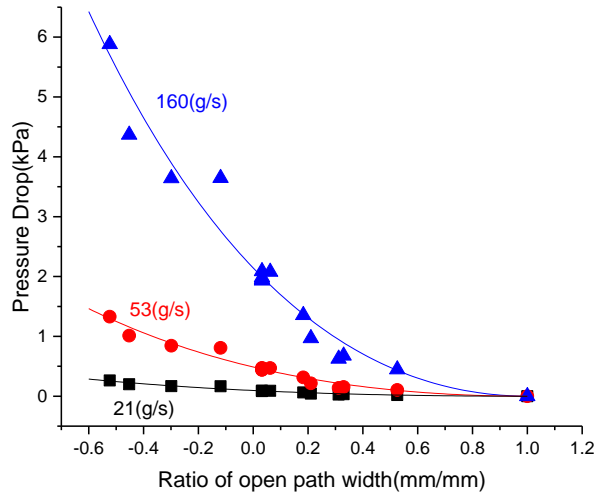


Figure 3-25. Effect of ratio of open path width on pressure drop for various inlet air mass flow rate(g/s)

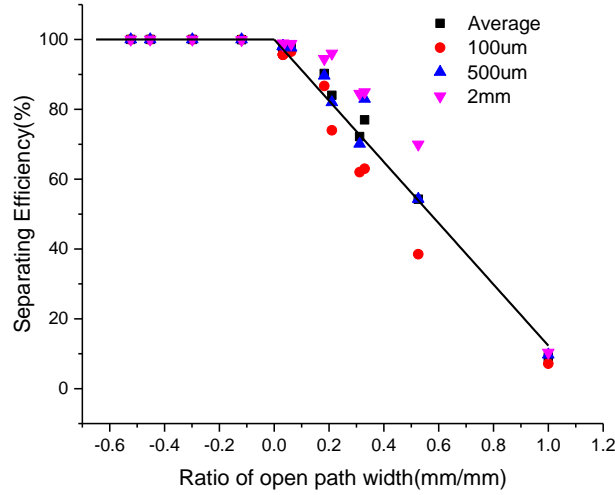


Figure 3-26. Effect of ratio of open path width on separation efficiency for various droplet size and on average

Empirical equations for the pressure drop and the separation efficiency were derived based on the simulation calculation results. The means to calculate the pressure drop and the separation efficiency are reported in equations (3-5) and (3-6) where pressure drop $\Delta p(\text{Pa})$, density of charge air $\rho(\text{kg}/\text{m}^3)$, and velocity of charge air at inlet $V(\text{m}/\text{s})$. $R(\text{mm}/\text{mm})$ is the ratio of open path width, and it is dictated by the geometry of the separator and is calculated as shown in equation (3-7).

$$\Delta p(\text{Pa}) = \left(\frac{49.4R^2 - 99.3R + 49.9}{R + 4} \right) \times \frac{\rho V^2}{2} \quad (3-5)$$

$$\text{Separation Efficiency} = \begin{cases} -87.69 \times R + 100, & \text{if } R > 0 \\ 100, & \text{if } R < 0 \end{cases} \quad (3-6)$$

$$R = 1 - \frac{\text{NO of Air Path}}{\text{Total Air Path Width}} \left[\left(\frac{\text{Blade Width}}{\cos\left(\frac{\text{Angle of Plate}}{4}\right)} \right) + \tan\left(\frac{\pi - \text{Angle of Plate}}{2}\right) \times \frac{\text{Wavelength}}{2} \right] \quad (3-7)$$

3.4.3 Experiment setup and results

To verify the simulation results for the pressure drop and the separation efficiency shown above, the engine tests were performed using prototypes of the charge air cooler condensation separator. Four pressure drop tests and two separation efficiency tests were performed according to the separator specifications in Table 3-11. The corrugated plates were made of ABS on a 3D printing machine. The separator was placed at the outlet of charge air cooler, and a reservoir is put at the bottom of the separator to collect the condensation. The test setup is shown in Figure 3-27.

Table 3-11. Specifications of separator prototypes for engine tests

<i>Case</i>	<i>Air path Width (mm)</i>	<i>Blade Length (mm)</i>	<i>Blade Width (mm)</i>	<i>NO. of Air Path</i>	<i>Angle of Plate($^{\circ}$)</i>
A	18	9	7	2	120
B	16	10	9	2	120
C	4	18	6	2	90
D	3	15	6	3	120

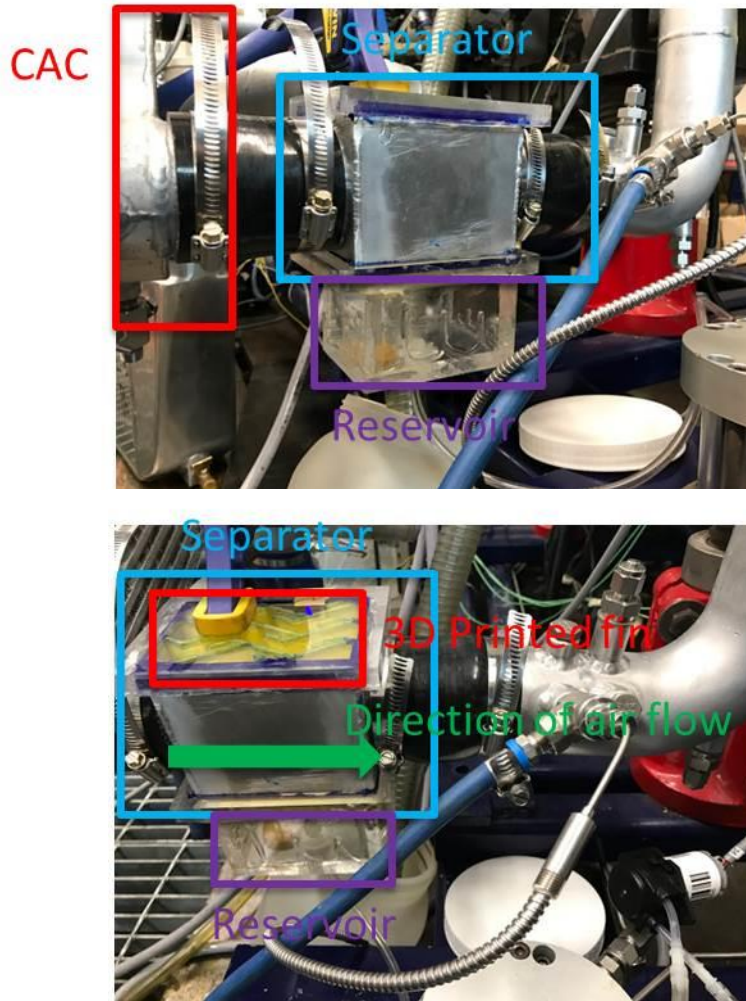


Figure 3-27. Engine test setup

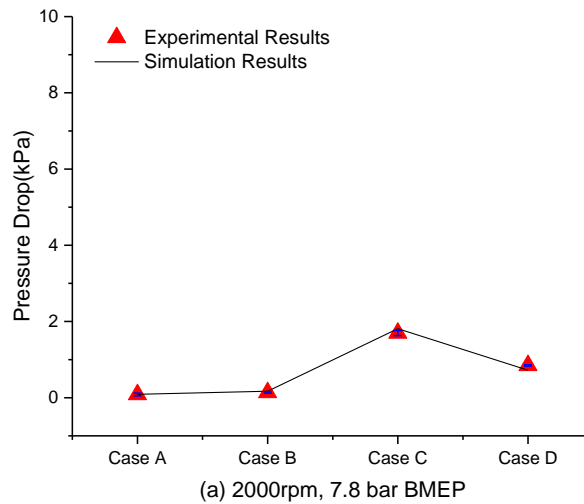
Two separate tests were conducted for the pressure drop and the separation efficiency. For the pressure drop, two different intake air mass flow rates were chosen, 0.021kg/s, and 0.053kg/s, corresponding to the engine conditions of 2000rpm/7.8bar BMEP, and 3000rpm/13.3 bar BMEP. The engine was operated and maintained for 10 minutes under each condition to reach a steady state. The pressure sensors were located before and after the charge air cooler. The pressure for these two locations was recorded with and without the separator and subtracted to calculate the pressure drop due to the separator. Each test condition was repeated three times.

For validation of the simulation results for the separation efficiency, experiments were conducted with transient engine conditions. The engine started at 2000rpm/7.8bar BMEP, and was held for 10 minutes to reach a steady state under non-condensing conditions. Then, the engine was tipped in at 3000rpm/13.3 bar BMEP for 20 seconds, and moved back to 2000rpm/7.8bar BMEP. To create a short and repeatable experiment, 200 ml water was added to the CAC outlet with the engine off; this avoided running for a longer time with a high humidity to condense water in the CAC. Other experiment settings were the same as presented above. The tests were repeated three times for each separator prototype. After each test, the weight of water remaining in the charge air cooler and the reservoir was measured to obtain the separation efficiency. Equation (3-8) used to calculate the separating efficiency is shown below.

$$\begin{aligned} & \text{Separating Efficiency}(\%) \\ & = \frac{\text{Amount Collected from the reservoir}}{\text{Amount collected from the reservoir} + \text{Amount flowed into the cylinder}} \end{aligned} \quad (3-8)$$

Figure 3-28 and Figure 3-29 show the comparisons between the simulation results and the experimental results for the pressure drop and the separation efficiency. Because the desired pressure drop (less than 5kPa at full load condition) was obtained only case A and B, the separation efficiency testes were considered with case A and B. Case C and D were chosen for a comparison and validation of angle of plate and number of air path. In the pressure drop comparison, the error between the experimental results and the simulation results was less than 10%. Overall, the simulation results are in good agreement with the experimental results.

For the separation efficiency, the simulation results show better separating efficiency than the experimental results. Some of the assumptions made for the numerical calculations can account for higher separation efficiency predictions. First, water droplets sitting on the wall surface were considered as being collected, because there is no method for an accurate calculation of droplet motion on the surface [101]. Second, water droplets were injected normal to the inlet surface and uniformly distributed. However, the direction and distribution of the droplets could not be estimated from the experiment. Lastly, some of the droplet sizes may be smaller than $100\mu\text{m}$. Small droplets are more difficult to collect and may reduce the separation efficiency.



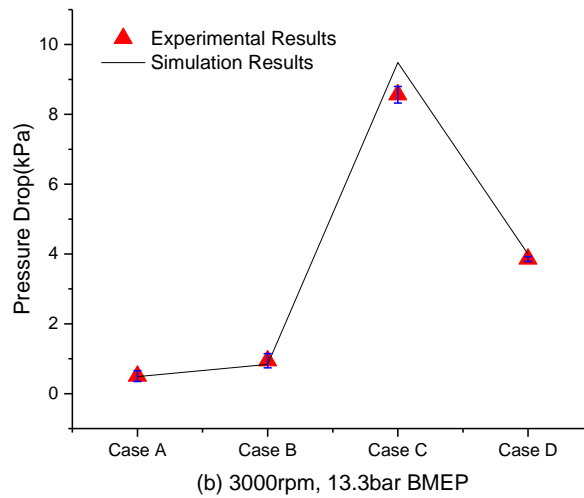


Figure 3-28. Comparison of pressure drop between simulation results (line) and experiment results (triangles), (a) 2000rpm, 7.8bar BMEP, (b) 3000rpm, 13.3bar BMEP

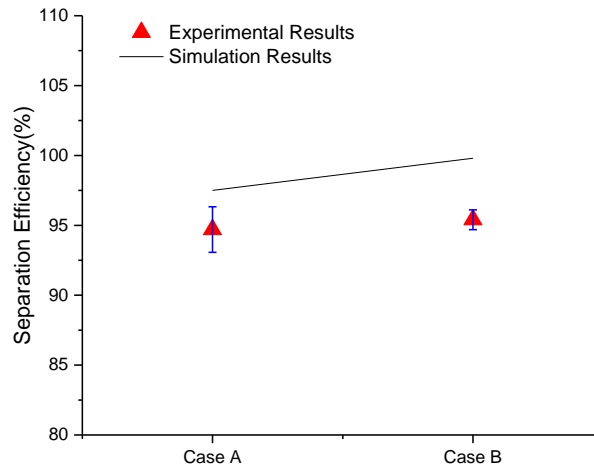


Figure 3-29. Comparison of pressure drop between simulation results (line) and experiment results (triangles)

3.4.4 Separator design integrated in charge air cooler

A separator which can be integrated with the current charge air cooler was designed as shown in Figure 3-30. The separator is placed between the charge air cooler

matrix and the outlet housing of the charge air cooler. The separator has the same height (157mm) and width (40mm) as the charge air cooler matrix installed in the engine. The length of the separator is set to 80mm. Table 3-12 shows specifications of the separator used in calculations. The pressure drop and the separation efficiency were calculated using the same setup shown in the section 3.4.1.



Figure 3-30. A prototype of separator integrated in charge air cooler

Table 3-12. Specifications of separator used in calculation

<i>Case</i>	<i>Angle of Plate($^{\circ}$)</i>	<i>Air path Width(mm)</i>	<i>Ratio of open path width</i>
I	180	22	0
II	150	22	0.25
III	180	25	0.10
IV	150	17	0.10

Figure 3-31 and Figure 3-32 show the effects of the ratio of open path width on the pressure drop and the separation efficiency. Symbols in the graphs mean the calculation results and lines mean the results of the empirical equation which was shown in equations (3-5) to (3-7) with each boundary condition such as the air mass flow rate. The calculation results are well matched with the empirical equations even if the separators have different geometries.

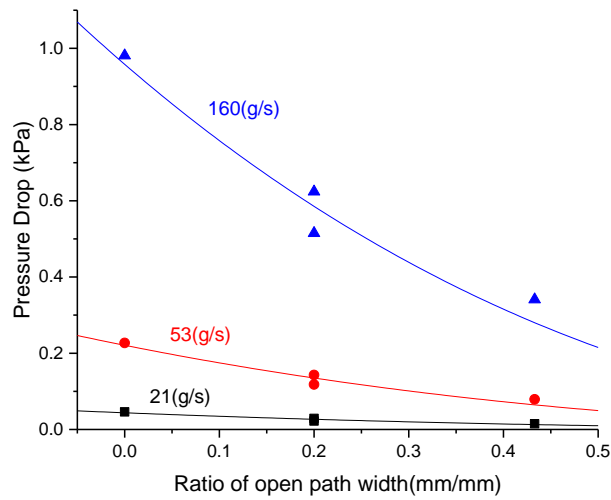


Figure 3-31. Comparison of pressure drop between simulation results (scatters) and empirical equation (line)

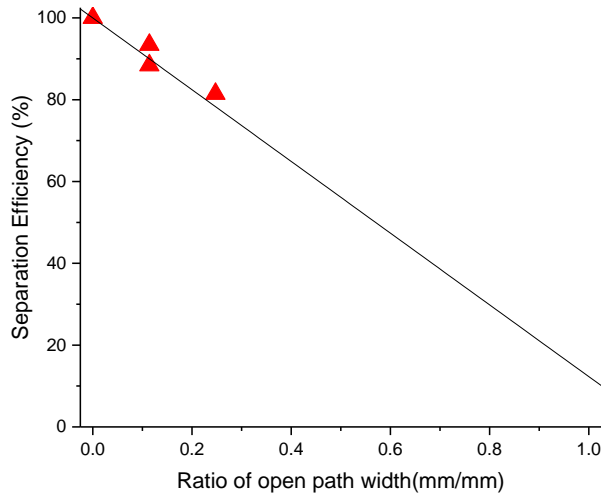


Figure 3-32. Comparison of separation efficiency between simulation results (triangle)

and empirical equation (line)

3.5 Conclusion

In this study numerical calculations of the amount of condensation generated from a charge air cooler are presented. Using a 1.6L GDI gasoline turbocharged engine, experiments have been conducted on the total amount of condensation of specific air humidity and four engine conditions. Those results show that the predictions are close to the experimental data.

With a hard acceleration, the water condensate generated in the charge air cooler was ingested into engine cylinder, and caused an abnormal combustion behavior such as a slowburn or a misfire. With different amounts of the condensate and different tip-in engine conditions, changes of maximum water concentration in the engine exhaust were measured and correlated to the number of slowburn and misfire events.

In addition, the numerical simulations of the pressure drop and the separation efficiency for a charge air cooler condensation separator have been developed. It was found that the ratio of open path width is a good variable to predict the pressure drop and the separation efficiency. Decreasing the ratio of open path width increases the pressure drop and the separation efficiency. If the ratio of open path width was less than 0, the separation efficiency was 100%. A total of 16 different separators were designed and simulated, and four prototype separators were engine tested. For the optimum design of charge air cooler condensation separator, the ratio of open path width should be close to zero for high separation efficiency and acceptable pressure drop. The charge air cooler condensation separator efficiently collects the condensate from the charge air. As a last

stage of this research, the prototype separators which can be integrated in a current charge air cooler were designed and engine tested. All of the simulation and experiment results matched well with the empirical equations.

Chapter 4

Effect of Water Injection on Auto-Ignition under Boosted Conditions

In this chapter, a careful examination of the effect of water on auto-ignition under boosted conditions is presented. The experiments were conducted in two different ways. The first experiment was for identifying the effect of water through changing intake air properties. The second experiment was for comparing the effect of water between intake air temperature drop and intake air properties change. Those experiments have been performed using a modified cooperative fuel research engine.

4.1 Experimental

4.1.1. Motored Engine Setup

In this work, a modified motored Cooperative Fuel Research (CFR) engine is used to study the effects of water on auto-ignition of hydrocarbon fuels. The engine is a modified CFR Octane Rating Engine, four-stroke single cylinder engine with

compression ratio controllable between from 4.0 to 15.7. This engine has been used extensively to investigate combustion and emission characteristics [102–107]. The engine used in this work has been modified by previous researchers [108–111]. A solenoid injector replaced the original carbureted fueling system. The injector used is a production part originally used for direct injection, but in this work it is placed upstream of the intake air system (1.4 meters above the intake valve) allowing that a fuel can be fully vaporized and mixed with the intake air. A fuel tank was located near the injector, and held under a constant pressure of 700 psi using an inert gas, helium, and fuel was injected at a constant frequency of 10 Hz. A Max Model 213 piston flow meter was used to control fuel mass flow rate. The addition of this Max flowmeter was made by previous researcher and calibration had been performed carefully [111]. A series of electric heaters and supplemental heaters were installed to control the intake air temperature as high as 260°C. Air mass flow rate was obtained using a Delphi hot wire mass airflow sensor. Additional modification was made to deliver dry and pressurized intake air to a maximum boost pressure of 3 bar (abs). A Kistler 6052B piezoelectric pressure transducer was used to measure the in-cylinder pressure at a 0.1 crank angle resolution for 70 cycles. The pressure signal was amplified by a Kistler 5010 dual mode amplifier and a LabView-based high speed data acquisition system recorded the signals. Engine speed was measured by an Accu-Coder shaft encoder at the resolution of a 0.1 crank angle per revolution. Static pressure sensors were installed at the intake plenum chamber and the exhaust plenum chamber. Two (8L, 1000 W and a 6L, 1100W) chiller circulators were used to maintain the engine cylinder temperature and the GDI fuel injector temperature to 90°C. A MedTherm coaxial thermocouple was used to measure the

cylinder wall temperature. The effect of residual gas has been carefully examined by previous researchers [108,109]. Residual gas was set to minimal by applying a slight vacuum (~ 0.97bar) to the exhaust. Details of the CFR engine and schematic are shown in Table 4-1 and Figure 4-1.

Table 4-1. CFR engine specification

Number of cylinder	1
Bore (cm)	8.26
Stroke (cm)	11.43
Connection rod (cm)	25.4
Swept volume (cm ³)	611.7
Compression ratio	4.0-15.7
Number of overhead valve	2
Engine speed (rpm)	900
Intake valve open (degrees after TDC)	10
Intake valve closes (degrees after BDC)	34
Exhaust valve open (degrees before BDC)	40
Exhaust valve closes (degrees after TDC)	15
Combustion chamber	Pancake piston

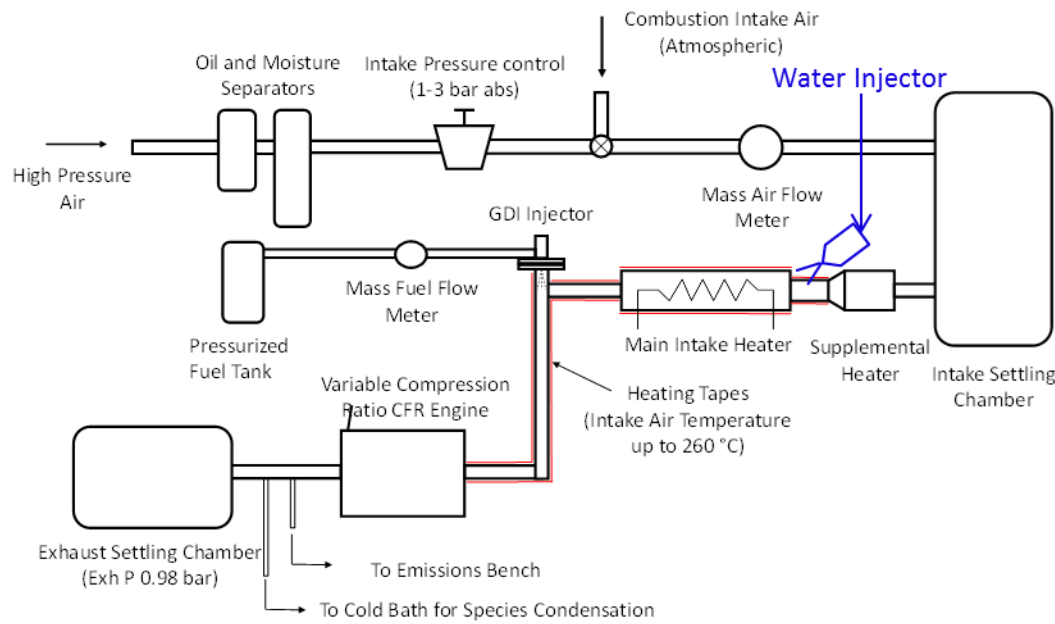


Figure 4-1. Schematic of the CFR engine setup

4.1.2. Water injection setup

To examine the effects of water on auto-ignition, the amount of water should be precisely controlled. A Waters Model 590 HPLC pump was used to deliver a desired amount of water. The specifications of the pump are shown in Table 4-2. Water was injected between the supplemental heater and the main intake heater. The supplemental heater pre-heated the intake air to 400°F before water was injected. This setup provides enough time for the water droplets to completely evaporate and be well mixed with the intake air. The controlled amount of water was delivered through a sintered stainless metal fitting. The inside of the fitting was filled by glass fiber to evaporate water quickly and constantly. The schematic diagram of the water injection in the intake manifold is shown in Figure 4-2.

Table 4-2. HPLC water pump specification

Operating temperature	4 to 38°C
Flow rate range	0.001 to 20.0 ml/min; 0.001ml/min increments
Flow rate accuracy	± 1% of setting at 3ml/min
Flow rate precision	± 0.1% from 0.1 to 20.0 ml/min ± 1% from 0.01 to 0.05 ml/min
Operating pressure limit	480 bar maximum ± 10% of reading

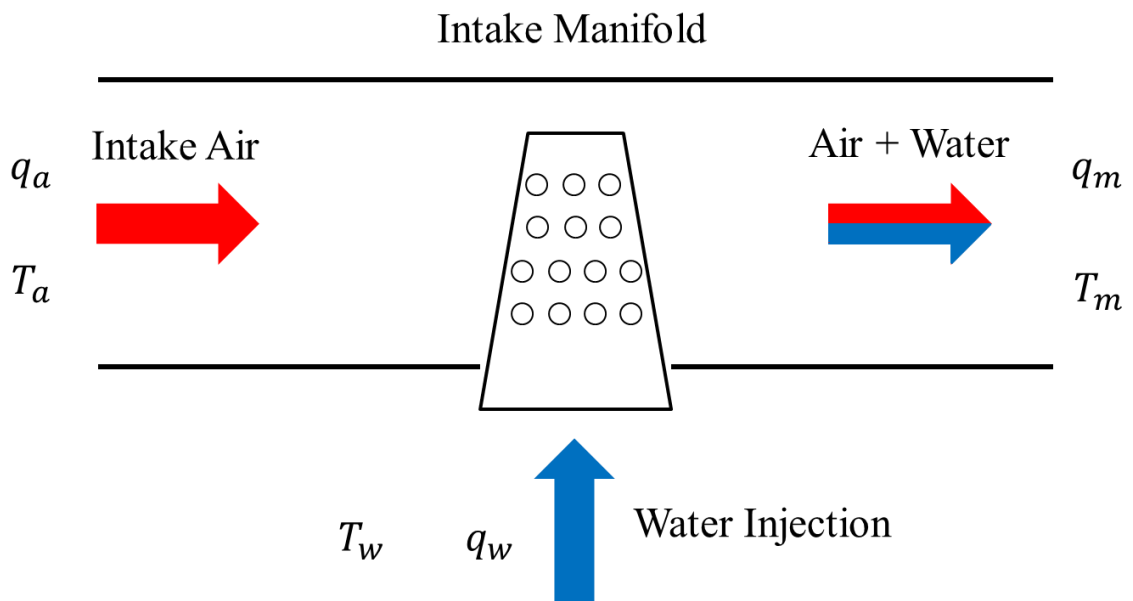


Figure 4-2. Schematic of water injection apparatus in the intake manifold

In the air and water mixture, the latent heat of vaporization is taken from the intake air. Assuming satisfactory mixing and sufficiently long time duration, the evaporation of the atomized liquid water would continue until the combined effect of cooling and increase in content of water vapor would bring about saturation. Thermodynamically the process can be broken down into two steps.

The thermodynamic equations that dictate the heat transfer between air and water at the moment when both are mixed are as following equations.

$$m_w c_w (T_w - T_m) = m_a c_{pa} (T_m - T_a) \quad (4-1)$$

$$c_{pa} = \frac{c_p T_a + c_p T_m}{2} \quad (4-2)$$

$$T_m = \frac{m_w c_w T_w + m_a c_{pa} T_a}{m_w c_w + m_a c_{pa}} \quad (4-3)$$

Where m_a and m_w are the mass of air in the manifold and mass of water injected respectively, c_w and c_{pa} are the specific heat of water and air. T_w , T_a , and T_m are the initial temperatures of water, and air, and final mixture temperature, respectively. The specific heat of air is a function of temperature, thus it can be averaged over the temperature before and after the heat exchange.

The mass of water reduces by a small quantity Δm_w which corresponds to the quantity of water that is converted into vapor. Thus the thermodynamic equation can be written as below in two phases; an initial phase and a second phase.

At the initial phase, there is no vapor present in the dry air. The change in temperature of the mixture is due to the evaporation of the small quantity of water, Δm_w . Latent heat of vaporization of the water varies according to temperature, however, for the intake manifold it can be assumed to be a constant 2500 kJ/kg under standard temperature and pressure conditions. The new temperature of the mixture on evaporation of the first mass can be given by the equation (4-4).

After the initial vaporization the specific heat of the vapor will also come into play. The specific heat of vapor, c_{pv} , can be considered to be around 2.5 kJ/kg-K under standard temperature and pressure. Thus the thermodynamic equation for the second

phase is in equation (4-5). Equation (4-5) is an iterative progression form, and thus can be represented as equation (4-6). The iteration index i is stopped by a numeric check that stops the iteration if the relative humidity reaches 100% (attainment of saturation) or m_w becomes zero.

$$[(m_w - \Delta m_w)c + m_a c_{pa}](T_{m\ Old} - T_{m\ New}) = \Delta m_w h_{fg} \quad (4-4)$$

$$[(m_w - \Delta m_w)c + m_a c_{pa} + \Delta m_w c_{pv}](T_{m\ Old} - T_{m\ New}) = \Delta m_w h_{fg} \quad (4-5)$$

$$[(m_w - i\Delta m_w)c_w + m_a c_{pa} + (i - 1)\Delta m_w c_{pv}](T_{m\ Old} - T_{m\ New}) = \Delta m_w h_{fg} \quad (4-6)$$

In the experiments, the total mass flow rate can be measured by the mass flow sensor, and relative humidity present in the intake air can be assumed to zero since the intake air passes through an oil and moisture separator. Therefore the humidity ratio under the intake manifold pressure and temperature can be determined using equation (4-7). Thus in the iteration equation, the iteration index i changes from 1 to n where n is the n^{th} iteration of the process. In the given amount of water, the humidity ratio at the n^{th} value is checked whether the relative humidity reaches to 100% or not. The solution of the iteration gives a final temperature of the mixture under saturated condition before the mixture enters the cylinder. This calculation is important because if the water is injected is more than the amount needed to reach water for 100% relative humidity, the excess water remains liquid in the intake manifold. Therefore at every test point, initial analyses were performed to check whether the amount of water was completely evaporated and the final temperature of mixture from the calculation was matched to actual measured temperature after the water injection port.

$$\text{Humidity Ratio} = \frac{m_v + n\Delta m_w}{m_a} \quad (4-7)$$

4.1.3. Heat release calculation

When the fuel burns, its chemical energy releases. By observing rate of the chemical energy release (or heat release), details of the progress of combustion can be quantified, which can be calculated from in-cylinder pressure versus crank angle over the engine cycle. The in-cylinder pressure and crank angle data are measured by the sensors and acquired through a LabView program as mentioned above. Those signals are filtered and smoothed to compute an apparent heat release rate (AHRR) using a single zone model [3]. The detailed explanations of the calculation were presented previously [108,111].

Because water is added to the intake air, the ratio of specific heats (γ) of the intake air mixture is changed. To compute the apparent heat release rate, the change in γ of the intake air mixture should be considered in the calculation. The new γ of the mixture is calculated using an equation (4-8).

$$\frac{\tilde{c}_{p,i}}{\tilde{R}} = a_{i1} + a_{i2}T + a_{i3}T^2 + a_{i4}T^3 + a_{i5}T^4 \quad (4-8)$$

Where i is each species, T is temperature, \tilde{c}_p is specific heat. Values of the coefficient a_{ij} for O₂, N₂, H₂O and equation (4-8) are from Heywood [3]. A specific heat of the mixture is calculated by multiplying mole fraction of each species and specific heat of each species.

4.1.4. Critical compression ratio

The benefits of the modified CFR engine are its flexibility for selection of the end of compression pressure and temperature in the cylinder, and the repeatability of the test

conditions compared to ideal reactors such as RCM, shock tubes, and flow reactors, that traditionally have been used to characterize hydrocarbon ignition behavior. In this study, the CFR engine is used as a chamber to compression ignite rather than spark ignite the fuel and air mixture and observe temperature, pressure and exhaust products to study auto-ignition and pre-ignition chemistry. The experimental method is that increase the compression ratio from 4 (which is the lowest compression ratio setting for the engine) until auto-ignition of the fuel and air mixture is observed. When the compression ratio is 4, a little or no reaction is expected and CO emissions stay pretty low or zero. By increasing the compression ratio, CO emissions increase slowly, but at a certain point, CO emission increases dramatically, and suddenly drops with further compression ratio increase. A reduction of CO emission means that CO is converted to CO₂ because more complete combustion occurs, with more CO oxidation to CO₂. The compression ratio at this point where CO emissions suddenly drop is defined as the critical compression ratio (CCR). Therefore, a condition with a higher CCR means that a test fuel is less prone to auto-ignite. This approach to observing auto-ignition and related chemical kinetics with regard to the compression ratio using the motored engine was introduced by Curran et al. [112]. Previous research [109–111] adopted the approach to modify the CFR engine to explore the CCR and a critical equivalence ratio for diesel fuels, gasolines, jet fuels, biofuels and model compounds.

4.1.5. Fuel Selection

The purpose of this study is to observe the differences in auto-ignition behavior of fuels with similar octane number fuel but with different amounts of water and with different intake air pressure. In the current study, premium gasoline is chosen as the base

fuel for the motored engine experiments, which has a RON of 98.7. In comparison, primary reference fuels (PRF) and a toluene reference fuel (TRF), prepared by mixing primary reference fuels with toluene, are used.

The primary reference fuel is a mixture of iso-Octane and n-heptane, and is used to define the octane reference scale for gasoline. Thus, a blend of 99% of iso-Octane and 1% of n-heptane by volume has a RON and MON of 99 by definition.

However, the operating condition for the RON test is different from current gasoline engines. Therefore RON does not represent a fuel's auto-ignition behavior sufficiently well in current technology GDI engines [113]. In practice, a combination of RON and MON $((RON + MON) / 2)$ is used to define the anti-knock index. The difference between RON and MON is referred to as the octane sensitivity. Since a gasoline used in this test has the sensitivity of 8.7, the auto-ignition behavior of the fuel as compared to the primary reference fuel is expected to be different [3,114]. To compare the auto-ignition behavior with water at similar octane sensitivity, a toluene reference fuel is adopted for this experiment. Toluene is one of the aromatic surrogates used in model gasoline fuels, and aromatic fuels show a higher resistance to auto-ignition than paraffin fuels such as iso-Octane [115]. Details of the test fuels are shown in Table 4-3. To calculate RON and MON of the TRF, a method presented in reference [116] was applied.

Table 4-3. Tested fuel specifications

	Gasoline	PRF	TRF
RON	98.7	99.0	99.1
MON	90.0	99.0	92.7
Sensitivity	8.7	0	6.4
iso-Octane		99 vol%	59 vol%
n-Heptane		1 vol%	9 vol%
Toluene			32 vol%

4.1.6. Test conditions

To examine the effect of water injection on auto-ignition under boosted conditions, the experimental conditions are divided into two different sets. The first test set is to observe the effect of changes of intake air properties under boosted conditions with water at a constant charge temperature. The second test set is to compare the effects of intake air property changes and the intake air cooling effect.

For the first test set, the following initial conditions were applied. The intake air temperature was set to 190°C, and this temperature enabled complete evaporation of the water in a short period of time. Moreover, by heating the premixed intake air (pressurized air with water, and pressurized air without water) to 190°C, the effect of intake air cooling on auto-ignition was eliminated.

The amount of water was controlled by an HPLC pump and water was injected at a water-fuel ratio from 0 to 1.5, in increments of 0.5. The water-fuel ratio is defined as a mass flow rate of water over a mass flow rate of fuel. The intake air pressure was swept from 1 bar

to 2.5 bar abs. The engine speed was kept constant at 900 rpm for all of the test conditions. Three test fuels were chosen for this experiment as shown above.

For the second test set, a comparison was made to de-couple the effect of intake air cooling and the intake air property changes in combination with the effect of water on auto-ignition behavior. To do this, three experimental conditions were examined. First was to measure the fuel auto-ignition behavior without water. Therefore, the temperature of the intake air was set to 207°C. Second was to measure the effect of the intake air cooling. Using equation (4-3), the predicted intake air temperature at the fuel-water ratio of 1.5 was calculated, but no actual water was added to the intake air. Therefore, the intake air temperature was set to 190°C without water. As the last experimental condition, the intake air temperature was set to 190°C and a certain amount of water (water-fuel ratio of 1.5) was also added to the intake air. By comparing the first condition and second condition, the effect of the intake air cooling effect of water can be derived, and by comparing the second condition and third condition, the effect of the intake air property changes with water can be observed.

For each test condition, compression ratio was gradually increased from the compression ratio of 4 to the critical compression ratio (CCR). Constant equivalence ratio (ϕ), 0.25, was maintained during the study. There are some reasons that a low equivalence ratio was selected. Compared to high equivalence ratio such as 1 or higher, it provides wider range to observe low temperature pre-ignition behavior. Also, it is a typical operation condition for homogeneous charge compression ignition (HCCI) engine. The summary of the test conditions is given in Table 4-4.

Table 4-4. Summary of the initial conditions for CFR water injection test

<i>Test set</i>	Fuel	Intake air Pressure	Intake air temperature	Phi	Water Fuel Ratio
1			190°C		0 – 1.5
2 - 1	PRF / TRF / Gasoline	1 - 2.5 bar abs.	207°C	0.25	0
2 - 2			190°C		0
2 - 3			190°C		1.5

4.2. Results

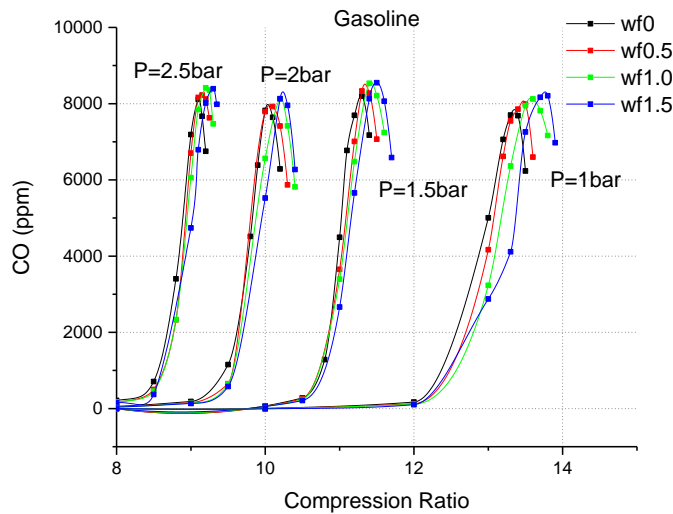
Overall, the effect of water can be categorized in two parts. When the water is injected into the intake air, the intake air temperature is decreased by evaporation of water droplets. The other effect of water addition is changing the intake air property. Due to water's high specific heat, the total intake air specific heat increases with water addition. Also, as water is added into intake air, oxygen concentration is reduced. Lastly, the presence of water molecules affects the chemical reaction pathway.

Therefore, the experiment consisted of two parts. One is for examining effect of water on changing intake air properties, and the other is for comparing the effect of water via intake air temperature drop and intake air property changes.

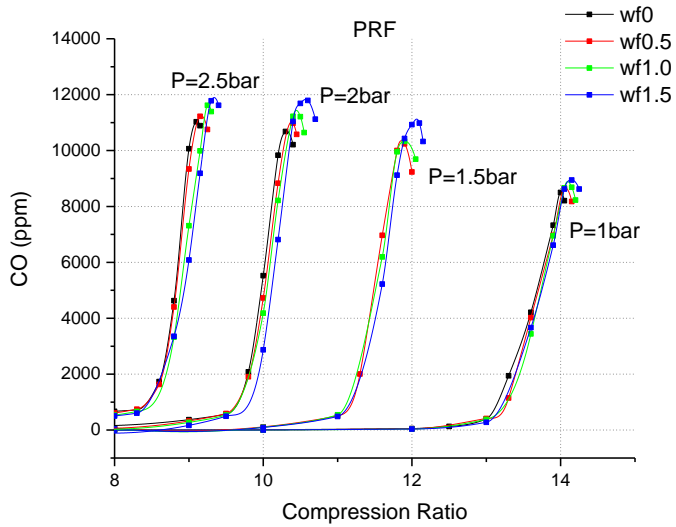
4.2.1. Effects of Intake air property changes under boosted conditions

As shown in Figure 4-3, at certain compression ratio CO converted to CO₂, and a sudden drop of CO concentration is observed. The results show that when a larger amount of water is injected into the intake air, a higher CCR was measured for all cases

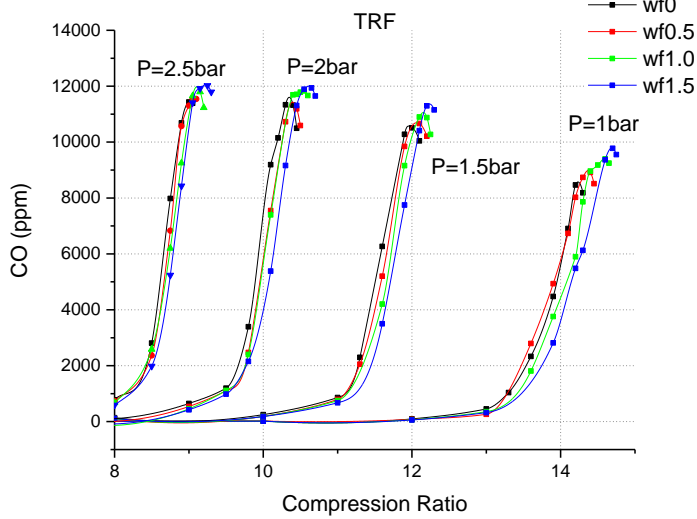
of premium gasoline, PRF, and TRF. This means that as a larger amount of water is injected, the effect of changing the intake air property is larger. This trend is shown to be more dominant for lower intake air pressure. Figure 4-4 shows that the critical compression ratio with various range for a range of water-fuel ratio and intake air pressure. As explained earlier, the critical compression ratio is defined as the compression ratio at which CO emissions suddenly drop. It can be observed that with increasing the intake air pressure, the CCR is advanced for all test fuels and, as expected, the CCR was higher for greater water-fuel ratio, when compared at the same intake pressure. The higher intake air pressure leads higher rate of hydrocarbon oxidation [117]. The results shown in these figures confirm that expected trend.



(a)



(b)



(c)

Figure 4-3. CO emission versus compression ratio at various intake pressures and water-fuel ratios for: (a) Gasoline, (b) PRF, (c) TRF

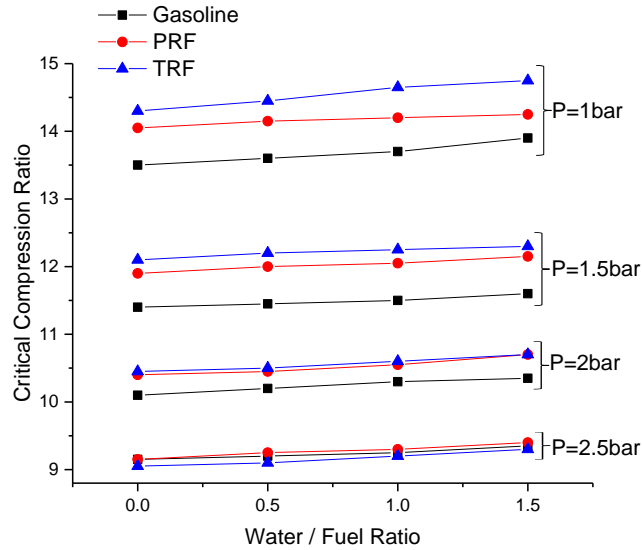
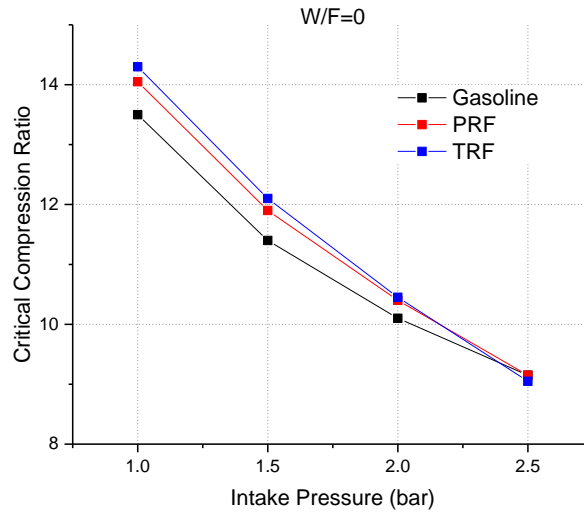


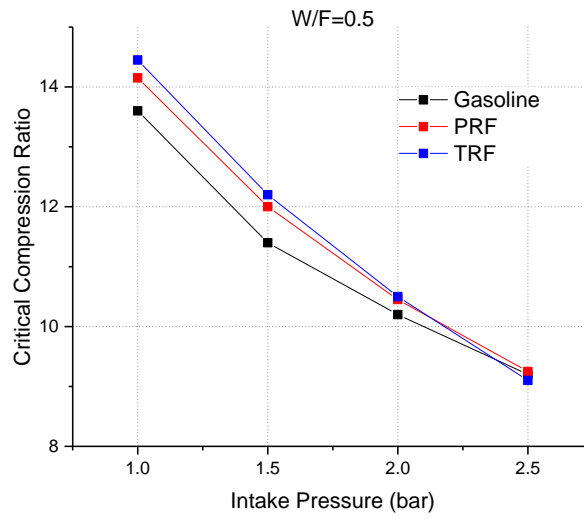
Figure 4-4. Critical compression ratio versus water-fuel ratio

Figure 4-5 shows the CCR results as a function of the intake air pressure for Gasoline, PRF and TRF to compare the effect of water on intake air property changes. The general trends are similar for test fuels, with the amount of water suggesting that reactivity of the fuels increases as the intake air pressure increases. TRF showed the highest CCR in all cases, because RON of TRF is higher than PRF and gasoline as shown in Table 4-3. Figure 4-6 shows the amount the CCR changed by adding water at different intake pressures. At 1bar intake air pressure, CCR change due to water addition was 0.4 and 0.45 for Gasoline and TRF, compared to without water and water fuel ratio 1.5. However, in case of PRF, CCR change due to water is only 0.2. At other intake air pressures, CCR changed due to water were similar for all three test fuels. With these results, it can be said that auto-ignition is suppressed by the effect of water while how the effect of water changes with the intake air pressure is not clearly explained. In studies [54,60], it was shown that with an increase of the amount of water addition, RON and

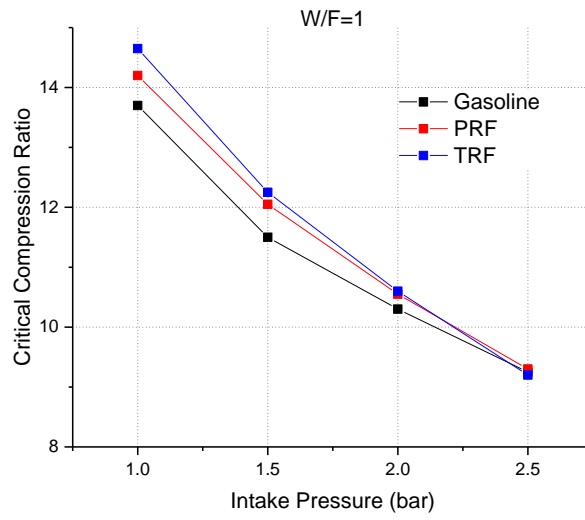
MON were increased. It means that water addition suppresses auto-ignition tendency and it agrees with the results.



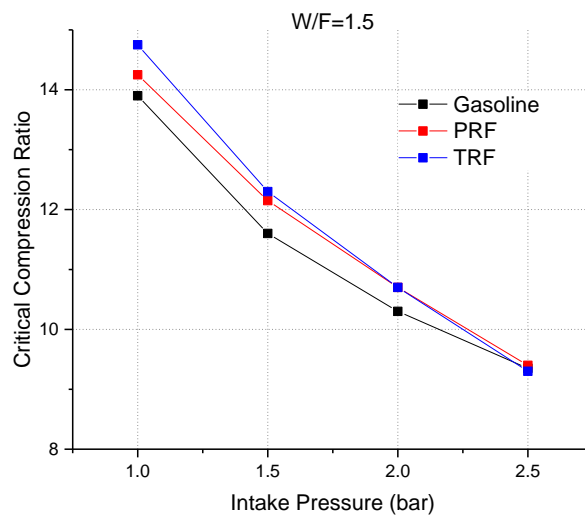
(a)



(b)



(c)



(d)

Figure 4-5. Critical compression ratio versus intake air pressure

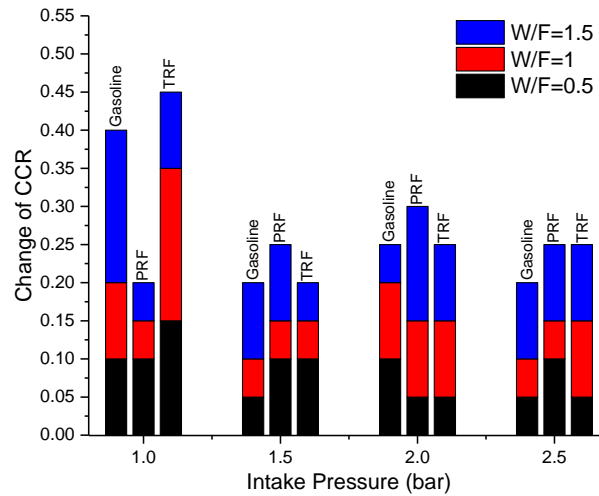


Figure 4-6. Change of critical compression ratio versus intake air pressure

The heat release rate indicates the progress of the combustion process at a given compression ratio. The heat release rate was used to derive the combustion phasing, the crank angle where 50% of fuel is burned (CA50) and combustion duration (CA1090), the crank angle differences where 10% of the fuel is burned (CA10) and 90% of the fuel is burned (CA90). Two compression ratios were selected to compare the effect of water. One was one specific value of compression ratio for all intake air pressure conditions. The other was a CCR for each test condition. Figure 4-7 shows the apparent heat release rate for PRF as a function of crank angle, intake pressure of 2.5bar, intake temperature of 190°C, ϕ of 0.25, and CR of 9.15. The peak heat release rate noticeably decreases with increasing water-fuel ratio. This agrees with results presented in earlier studies [65,89]. The authors state that water absorbs the energy released, and reduced the peak heat release rate. Again, this means that water suppresses auto-ignition. Figure 4-8 shows the apparent heat release rate for PRF as a function of crank angle, intake pressure of 2.5bar, intake temperature of 190°C, ϕ of 0.25, and CCR. It seems that there is no change on the

peak heat release rate at CCR. In addition, based on the comparison of combustion phasing (CA50), there is a trend that the combustion phasing is shifted to somewhat advanced, except for the gasoline cases. In case of combustion duration (CA1090) comparison, there is a lack of evidence whether the water addition in the intake air affects the combustion duration. Similar observation could be seen in a study by Hoppe et al. [85]. Although the test conditions were different (engine configuration and water injection methods), CA50 was generally advanced by adding water and CA1090 did not show clear correlations by adding water.

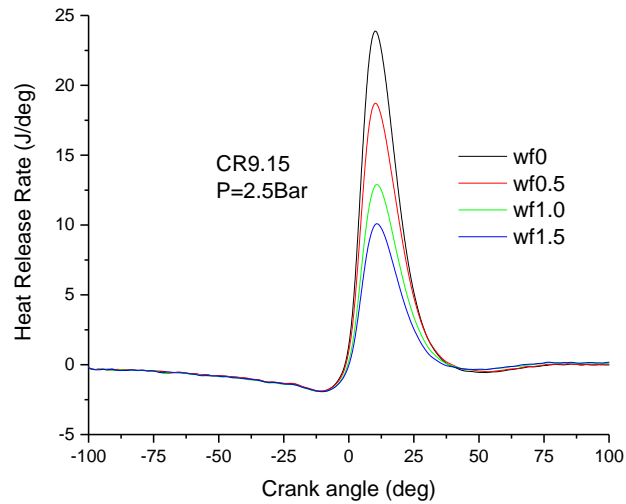


Figure 4-7. Apparent heat release rate profiles for PRF with water-fuel ratio 0 – 1.5 as a function of crank angle at CR=9.15

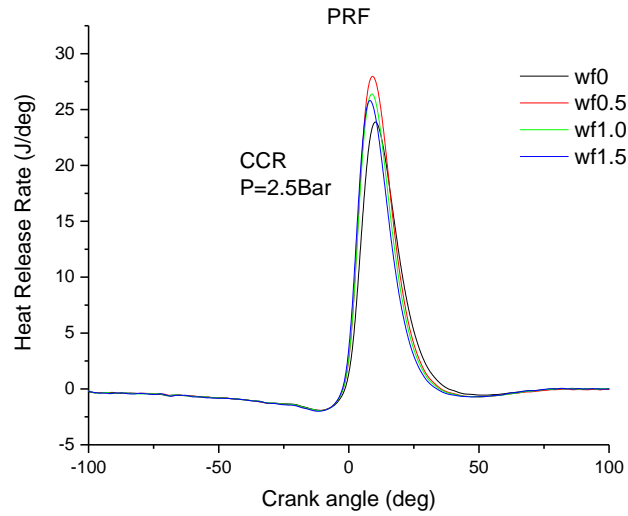


Figure 4-8. Apparent heat release rate profiles for PRF with water-fuel ratio 0 – 1.5 as a function of crank angle at CCR

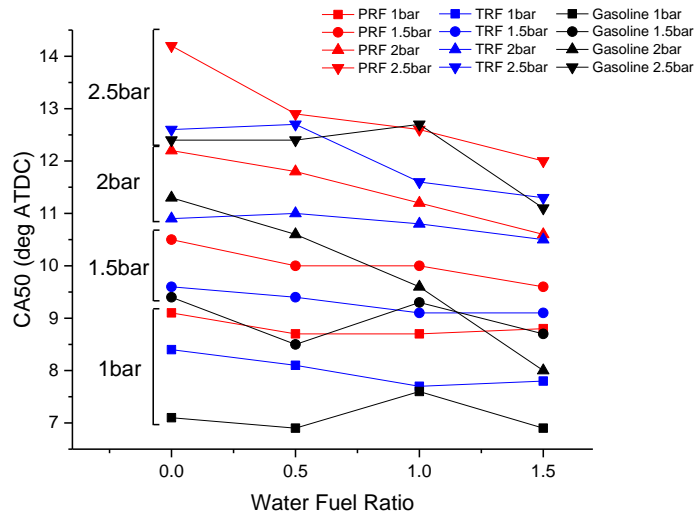


Figure 4-9. CA50 versus water-fuel ratio at CCR

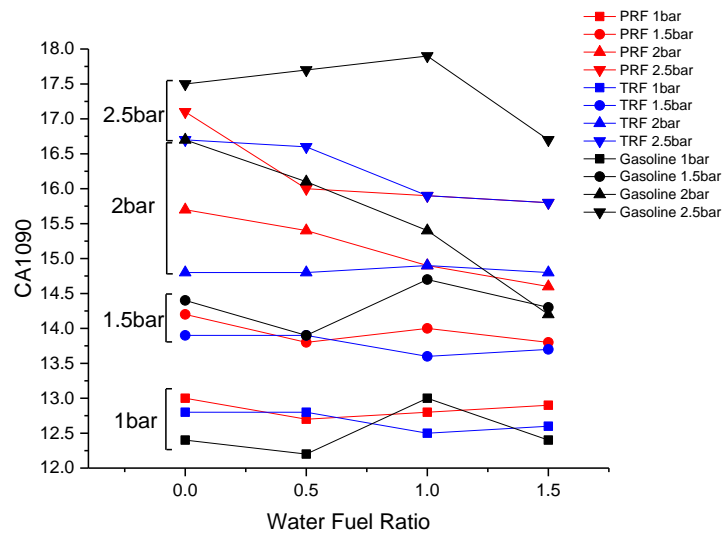


Figure 4-10. CA1090 versus water-fuel ratio at CCR

As Figure 4-11 and Figure 4-13 show maximum in-cylinder temperature profile and in-cylinder pressure profile for PRF with water-fuel ratio from 0 to 1.5 and the intake air pressure from 1bar to 2.5 bar. By adding more water, it is observed the lower maximum in-cylinder temperature, which is consistent with results from earlier studies [68,84,85,87,89]. At all intake air pressure conditions, higher water-fuel ratio led to ignition at higher compression ratio. Those results show that beyond a certain compression ratio, the temperature and pressure suddenly start to increase, which indicates a shift towards high temperature chemistry. This point shall be termed as a “thermal runaway” point. This thermal runaway temperature occurs at a lower CCR at the higher intake pressure. Moreover, with less water addition, a lower thermal runaway temperature was observed. It points out that water suppresses the onset of high temperature heat release. Figure 4-12 shows a zoomed figure of Figure 4-11. It is overserved that thermal runaway temperature is almost 7K differences. It can be observed from Figure 4-14 that the critical pressure, corresponding to the thermal runaway point, for W/F ratio of 1.5 is higher compared with that for W/F ratio of

0. Also, at higher intake pressure of 2.5 bar, the difference between the critical pressures is less compared with the 1 bar intake pressure suggesting that the reactivity suppression due to water addition is less pronounced at higher intake pressures. For two other test fuels, Gasoline and TRF, similar results were observed, meaning that the effect of water with changing intake air properties is less pronounced for different types of fuels, when those fuels have similar RON.

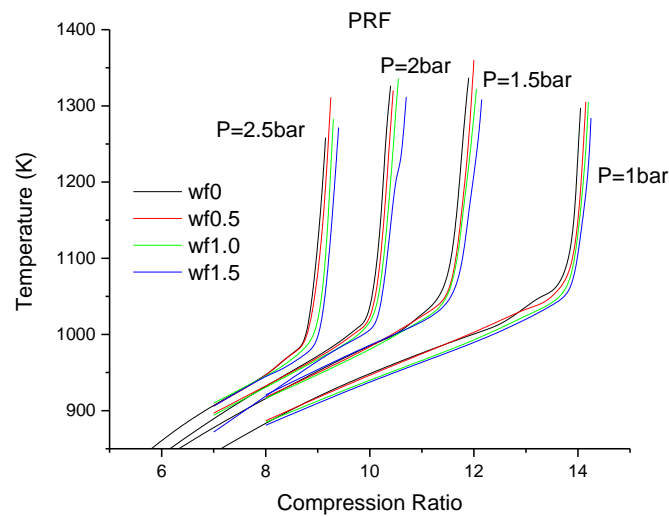


Figure 4-11. Maximum bulk in cylinder temperature for PRF with water-fuel ratio 0 – 1.5 versus compression ratio

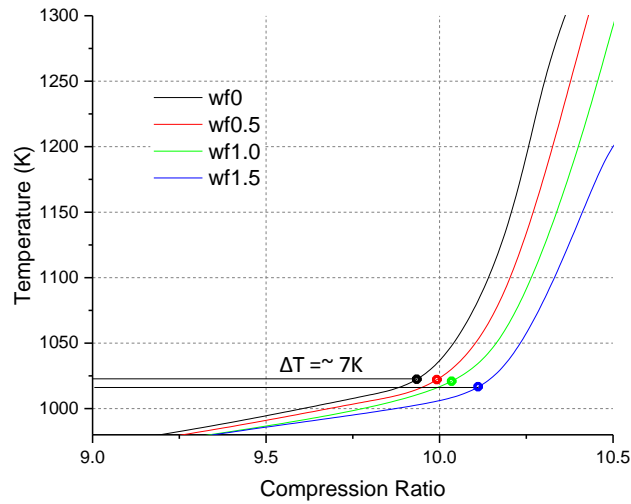


Figure 4-12. Zoomed in plot of Figure 4-11 indicating the thermal runaway points and differences in temperature

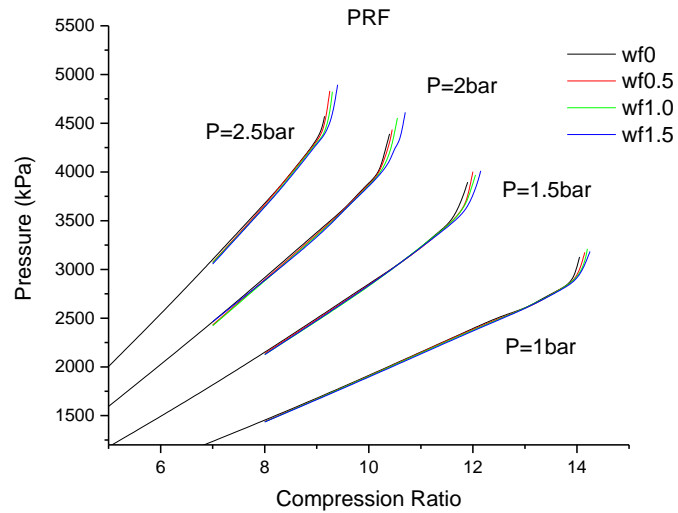


Figure 4-13. Maximum bulk in cylinder pressure for PRF with water-fuel ratio 0 – 1.5 versus compression ratio

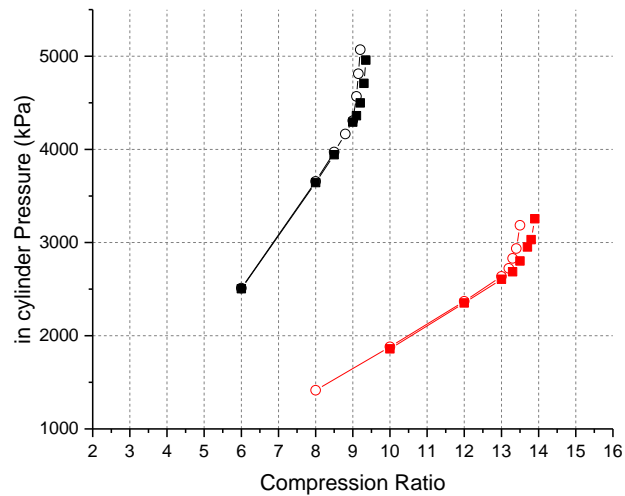


Figure 4-14. Maximum in cylinder pressure expressed as a function of compression ratio for W/F ratio 0 (○) and W/F ratio 1.5(■), Two intake pressure are shown; 1bar(—), 2.5bar(—)

4.2.2. Intake air cooling vs intake air property change

In this section, the results of comparison of the effects of water between intake air temperature drop and intake air property changes.

Figure 4-15 shows CO emission concentration for PRF at 1bar to 2.5bar intake air pressure and 3 different boundary conditions. It was shown that when the intake air temperature is 207°C without water, CCR was measured on the all cases of premium gasoline, PRF, and TRF. By changing the conditions, 190°C without water and 190°C with water, higher CCR was observed, as expected. In Figure 4-16, the critical compression ratio changes are compared with change in intake temperature (to simulate the evaporative cooling), and with intake air property changes (due to water vapor addition) while varying intake air pressure with PRF. It is shown that effects of water,

intake air cooling and intake air property changes, are constant for increasing intake air pressure. Although the results for the two other test fuels are not shown here, overall effect of water is similar for each of the test fuels.

As a result, critical compression ratio change due to intake air cooling on entire tested fuels was recorded 0.28 ± 0.02 compression ratio, and due to intake air property changes when water-fuel ratio 1.5 was recorded 0.28 ± 0.03 compression ratio. It can be observed from this result that as water is added to intake air, the effect of intake air temperature and effect of intake air properties are almost equivalent, as shown in Figure 4-17.

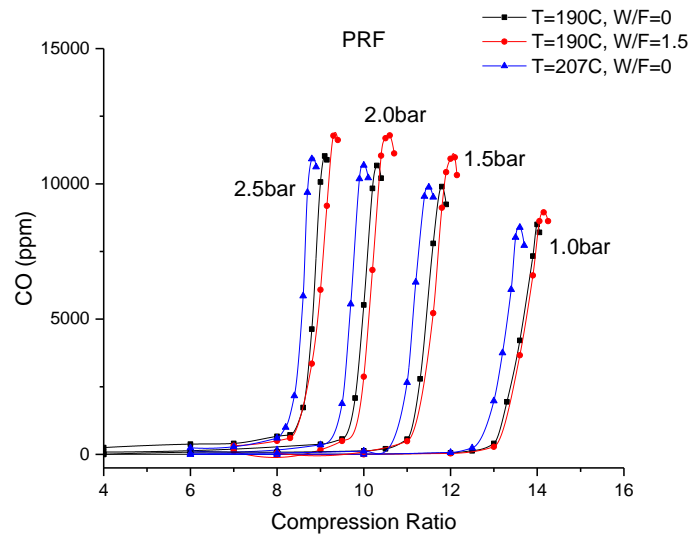


Figure 4-15. CO emission of PRF expressed versus compression ratio at various intake pressure and water-fuel ratio

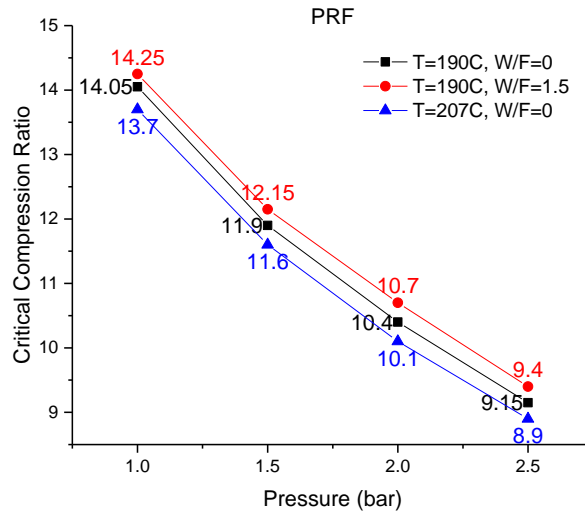


Figure 4-16. Critical Compression Ratio changes for PRF due to intake air cooling (differences of ■ and ▲) and intake air property changes (differences of ● and ■)

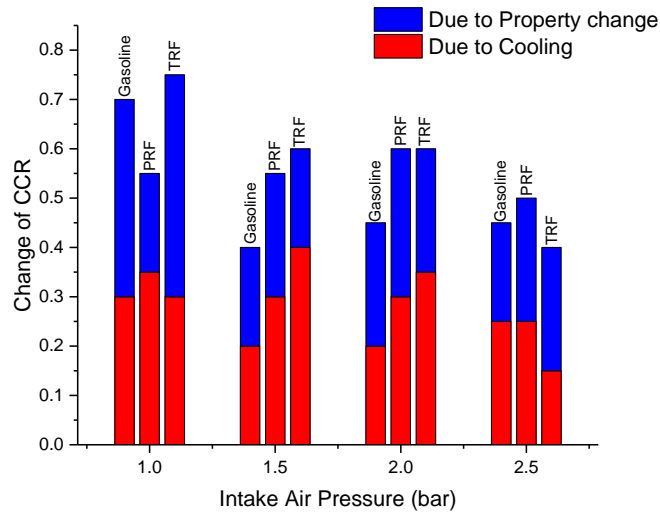


Figure 4-17. Change of critical compression ratio versus intake air pressure

The heat release rate analysis was done with similar method presented in previous section. Figure 4-18 shows the apparent heat release rate for PRF as a function of crank angle, intake pressure of 2.5bar, ϕ of 0.25, and CR of 8.8. Three different boundary conditions were compared. The magnitude of heat release rate noticeably decreases with 190°C intake air temperature without water and with water. Figure 4-19 shows the

apparent heat release rate for PRF at same condition as Figure 4-18, except its compression ratio. It seems that there is no change of the magnitude of heat release rate at CCR. As same as in previous section, combustion phasing (CA50) and combustion duration (CA1090) were compared. The combustion phasing tends to be advanced except for gasoline at 2 bar intake pressure. In case of combustion duration (CA1090), overall the combustion duration is shorter when decreasing the intake air temperature and adding water except for the gasoline 2 bar intake pressure. The effect of intake air temperature change on the combustion duration seems higher than the effect of intake air property change.

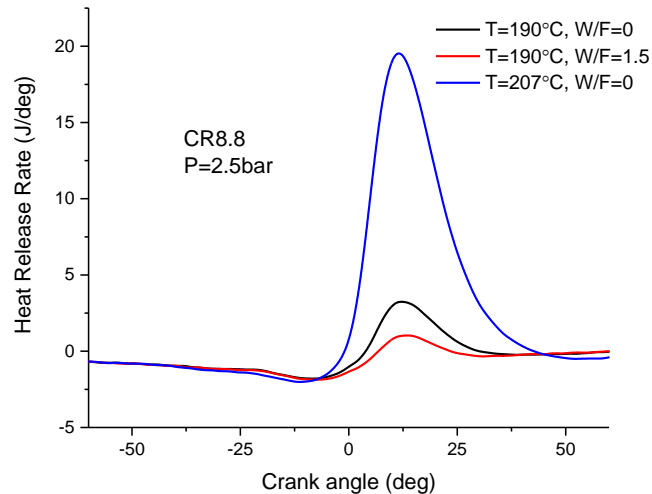


Figure 4-18. Apparent heat release rate profiles for PRF versus crank angle at CR=8.8

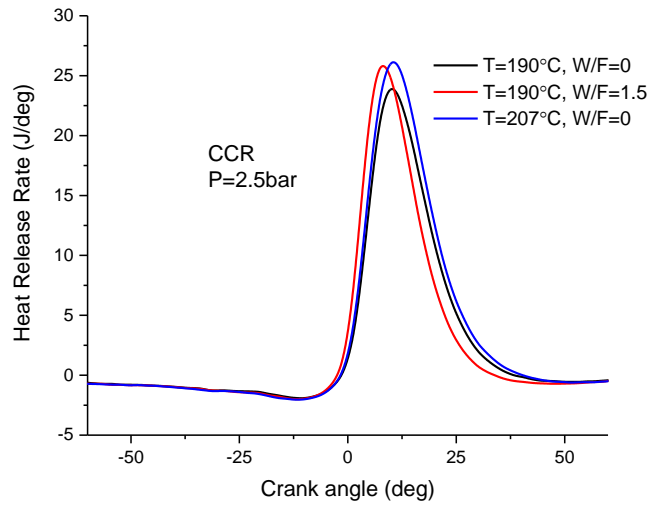


Figure 4-19. Apparent heat release rate profiles for PRF versus of crank angle at CCR

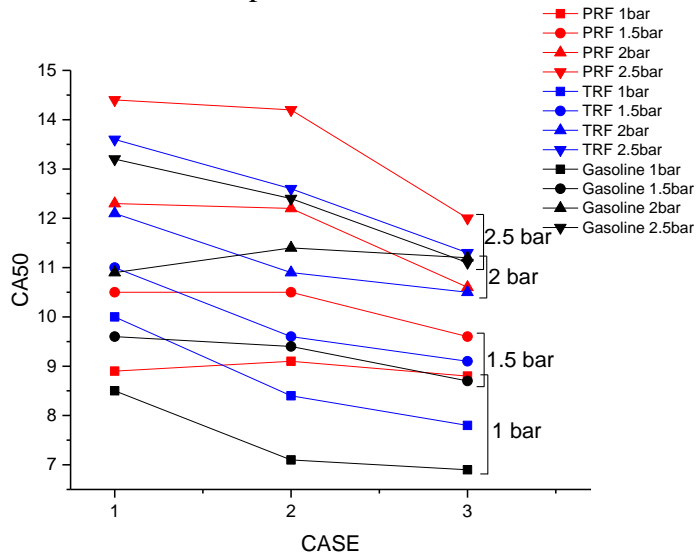


Figure 4-20. CA50 as a function of water-fuel ratio at CCR

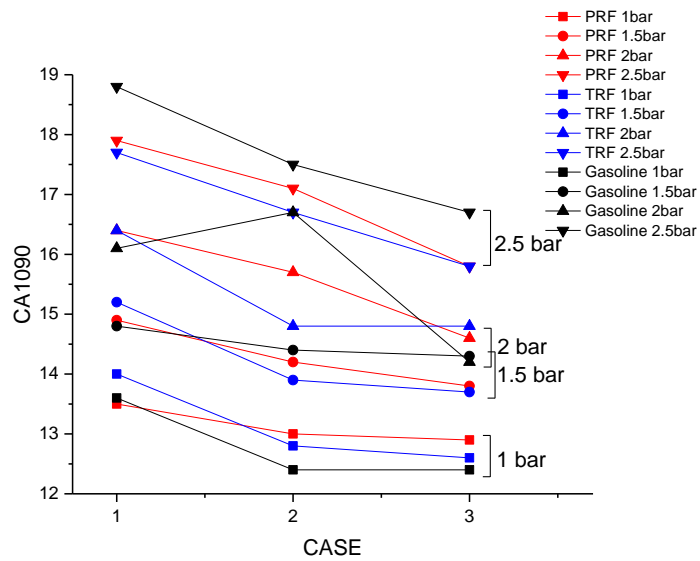


Figure 4-21. CA1090 as a function of water-fuel ratio at CCR

Figure 4-22 and Figure 4-24 show maximum in-cylinder temperature profile and in-cylinder pressure profile for PRF. The thermal runaway point with 207°C intake air temperature without water is lower than for 190°C intake air temperature with or without water. It is observed that thermal runaway temperature are almost 22K different due to intake air cooling effect and near 7K different due to intake air property change, as shown in Figure 4-23. Figure 4-24 shows the critical pressure, corresponding to the thermal runaway point. The higher critical pressure difference was observed for the effect of intake air cooling. As a result, in-cylinder temperature and pressure are more strongly affected by the intake air cooling than the intake air property change. In other words, the intake air temperature affects the onset of HTHR more than the changes of intake air properties. For two other test fuels, Gasoline and TRF, similar results were observed.

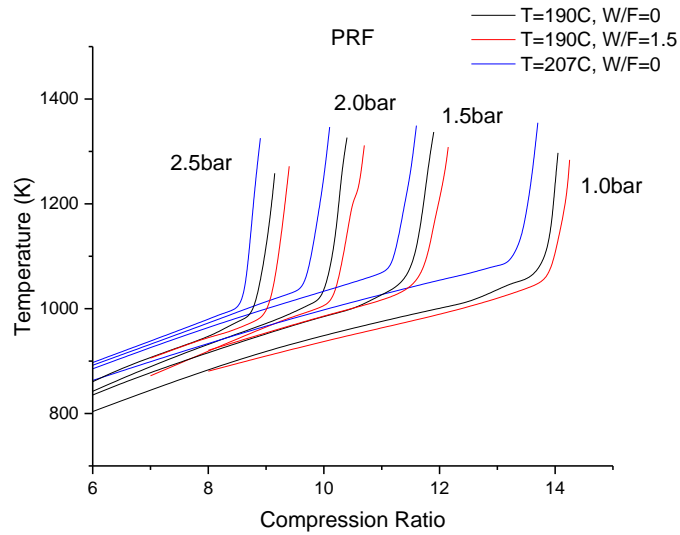


Figure 4-22. Maximum bulk in cylinder temperature for PRF versus compression ratio

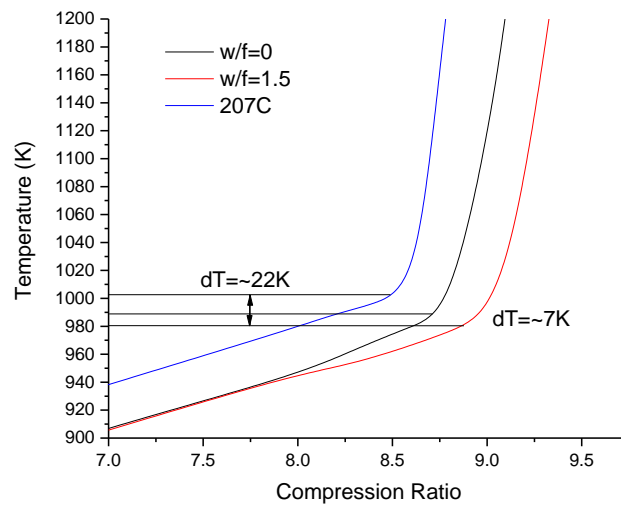


Figure 4-23. Zoomed in plot of Figure 4-22 indicating the thermal runaway points and differences in temperature

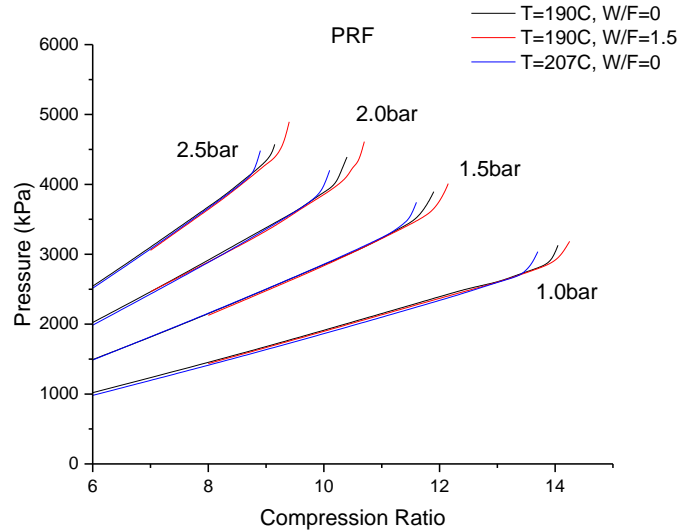


Figure 4-24. Maximum bulk in cylinder pressure for PRF versus compression ratio

4.3. Conclusion

Previous studies have characterized the effect of water on auto-ignition with the modified CFR engine. Three test fuels gasoline, PRF, and TRF which have similar RON were used for this test at various intake pressures and amounts of water addition. First test was done with constant intake air temperature and ϕ . This condition excludes the effect of intake air cooling due to water injection. One of the key conclusions from this study was that all of test fuels showed decreased reactivity as the water-fuel ratio was increased. Also, as the intake pressure was increased from 1 bar to 2.5 bar the CCR was decreased. All of selected fuels had similar CCR without water and by adding water the auto-ignition was suppressed.

Heat release analysis was used to examine the effect of water on combustion phasing and duration. The heat release was compared at CCR and at the same compression ratio just before of CCR. At CCR, the magnitude of heat release was

decreased by increasing the amount of water added to the intake air. Except for a couple of test conditions, combustion phasing tends to be advanced regarding to the crank angle by adding water, while no changes of combustion duration. Bulk in-cylinder temperature and pressure analysis indicated that the more water in the intake air, the lower the thermal runaway temperature as compared to no water addition.

Second test was for comparing the effect of the intake air cooling and the effect of the intake air property change. These results show that CCR changes, due to the intake air cooling and due to intake air property change when water-fuel ratio 1.5, were similar. The results show that the effect of intake air temperature change on the combustion duration seems higher than the effect of intake air property change. In the case of bulk in-cylinder temperature and pressure, the effect of the intake air cooling effect on thermal runaway temperature and critical pressure was greater than the effect of the intake air property changes.

Chapter 5

Chemical Reaction of Water with Oxygenated Fuels

In this chapter, the analytical and numerical modeling of the auto-ignition of oxygenated fuels with water is described. One of the common approaches for examining the hydrocarbon oxidation process is CFD simulation using a chemical kinetic mechanism. The mechanism shows the reactions pathway between the chemical species and the reaction rates in the hydrocarbon oxidation process. CHEMKIN is adapted for the calculation of reaction kinetics and thermodynamic properties.

5.1 Simulation Setup

5.1.1 Modeling tools

CHEMKIN is a software tool developed by Sandia National Laboratories for solving and modeling chemically reacting flows [118]. It is a highly structured computational tool that requires a kinetic mechanism and a thermodynamic database. It consists of number of programs, libraries of subroutines and data files. After CHEMKIN

reads the reaction mechanism, the kinetic reaction rate (forward) is calculated by equation (5-1)

$$k_{fi} = A_i T^{\beta_i} \exp\left(\frac{-E_i}{R_c T}\right) \quad (5-1)$$

where the pre-exponential factor A_i , the temperature exponent β_i , and the activation energy E_i . In addition, the reverse rate coefficient for a reaction is calculated based on equilibrium constants using thermodynamic data by equation (5-2).

$$k_{ri} = \frac{k_{fi}}{K_{ci}} \quad (5-2)$$

$$K_{ci} = K_{pi} \left(\frac{P_{atm}}{RT}\right)^{\sum_k v_{ki}} \quad (5-3)$$

where the equilibrium constants K_{pi} , the stoichiometric coefficients v_{ki} [119].

Three different approaches pursued done for examining the chemical effect of water on the auto-ignition process. First, ignition delay times with water and without water are calculated. Though the ignition delay analysis provided a valuable indication of auto-ignition characteristics with water, a fundamental understanding on the chemical effect of water is not obtained through the ignition delay analysis. Therefore, a brute-force sensitivity analysis with respect to H₂O and the detailed chemical reaction pathways are compared with water and without water.

5.1.2 Methodology

Ignition delay is defined as the period between the start of fuel injection into a combustion chamber and the start of combustion [3]. Therefore, the ignition delay is an indicator of the tendency toward auto-ignition. Numerous studies have been conducted on

the ignition delay using rapid compression machines, shock tubes, Ignition Quality Tester (IQT) and so on [120–128]. Also there are several ways of obtaining the ignition delay. It can be defined as the time of the maximum of certain species concentrations, the time of the specified temperature increase rate occurs, or the time when specific chemiluminescence is first observed. In this analysis, the ignition delay is defined as the time of the largest rate of change of temperature with respect to time.

Combustion is a very complex phenomenon. To understand this phenomenon, careful examination of interactions of physical and chemical processes is required. Sensitivity analysis is a very useful tool to analyze the chemical reaction pathways that are crucial during a reaction process. By applying the sensitivity analysis, the complex combustion reaction mechanisms can be simplified so that the dependency on the certain parameters can be determined. Furthermore, by using the main control parameters, a prediction can be made in similar conditions and for a range of variables. The sensitivity analysis in chemical kinetic mechanisms has been studied and applied many times [129–134]. Reaction pathway analysis is another technique to detect the important chemical reactions in a combustion process. It assists in developing a reaction mechanism which covers ranges of conditions such as composition, temperature and pressure. In other words, it can also be utilized to develop a simplified version of the detailed mechanism by removing unimportant species.

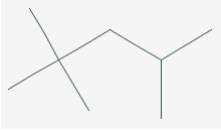
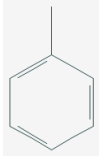


5.1.3 Modeling setup

All the simulations have been conducted using the zero dimensional, closed, homogeneous batch reactor model to control the volume and temperature of an intake

charge mixture. The reactor conditions for the calculation are constant volume and adiabatic. The pressure is set to 20 atm and temperature is swept from 714 K to 2000 K. In this research, the chemical reaction mechanism and thermodynamic data are chosen presented in the reference [130]. This mechanism contains 8231 reactions and 1944 species.

In this study, iso-Octane (2,2,4-trimethylpentane) is chosen as the base fuel with a RON of 100. In addition, three fuels, toluene, Ethanol, and n-Butanol are considered to examine the detailed chemical reaction, in the presence of water. Toluene is one of the most plentifully aromatics in gasoline, and commonly used as a surrogate for the other aromatics in the fuel. Therefore, understanding the auto-ignition behavior of toluene in the presence of water is important to predict the auto-ignition behavior of gasoline. In addition, Ethanol is already employed in commercial gasoline as a blending agent and it is expected that higher percentages of Ethanol will be applied in gasoline blends in the future(e.g., mid-level blends) [135]. n-Butanol is one of the key renewable fuels. n-Butanol offers similar volumetric energy density as that of gasoline, higher octane number, and has a high latent heat of vaporization, though neither the octane number nor the latent heat of vaporization are as high as for Ethanol [136]. The physical and chemical properties of the test fuels are shown in Table 5-1.

Table 5-1. Summary physical and chemical properties of tested fuels

	iso-Octane	Toluene	n-Butanol	Ethanol
Chemical formula	$\text{CH}_3\text{C}(\text{CH}_3)_2\text{CH}_2\text{CH}(\text{CH}_3)_2$	$\text{C}_6\text{H}_5\text{CH}_3$	$\text{C}_4\text{H}_9\text{OH}$	$\text{C}_2\text{H}_5\text{OH}$
Structure				
MW(g/mol)	114.23	92.14	74.11	46.06
O ₂ (mass %)	0	0	21.6	34.8
LHV(MJ/kg)	44.8	40.6	33.3	26.8
Stoichiometric air/fuel ratio	15.13	13.51	11.19	9
RON	100	121	92	109
MON	100	107	71	90
Density (kg/m ³)	692	862	802	790
Flash point(C)	4.5	4	28	8
Auto-ignition temperature(C)	418	480	415	434
Boiling Point(C)	99	110.6	108	78.4
Solubility in water (ml/100ml H ₂ O)	none	none	10.6	Fully miscible

When water is added into the inlet charge mixture at a constant temperature, there are three different effects on the combustion process. First is the dilution effect, which decreases O₂ concentration. Second, there is a thermal effect which raises the specific heat capacity of the inlet charge mixture. The last effect is a chemical effect, which is the main focus of this research. To identify the chemical effect of water, the dilution effect and the thermal effect should be isolated. To do so, a fixed concentration of oxygen is applied and set to 20.9 % mol. To eliminate the thermal effect, a mixture of water and

argon, which has lower specific heat capacity than nitrogen, replaces some of the nitrogen in the inlet charge mixture. Therefore, by keeping a constant oxygen concentration, the specific heat capacity of the inlet charge mixture is the same as the specific heat capacity without water. The methodology used to separate the dilution effect and the thermal effect of water on combustion is shown in Figure 5-1. In Table 5-2, mole fractions of constituents used in the calculations are presented and in Figure 5-2, specific heat capacity of the inlet charge mixture compared to other gases is shown.

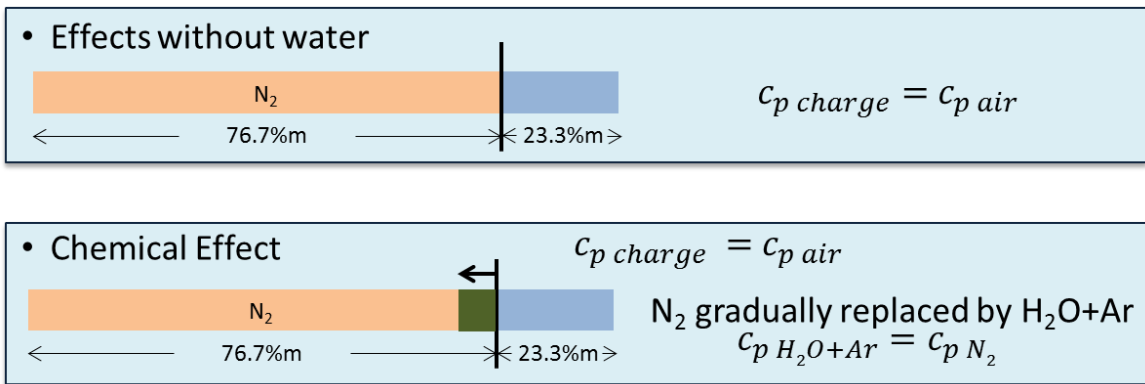


Figure 5-1. The methodology used to separate the effects of H₂O on combustion

Table 5-2. Summary of the mole fraction of the inlet charge mixture

	O ₂	N ₂	H ₂ O	Ar
Without H ₂ O	20.9%	79.1%		
With H ₂ O	20.9%	65.6%	10.0%	3.5%

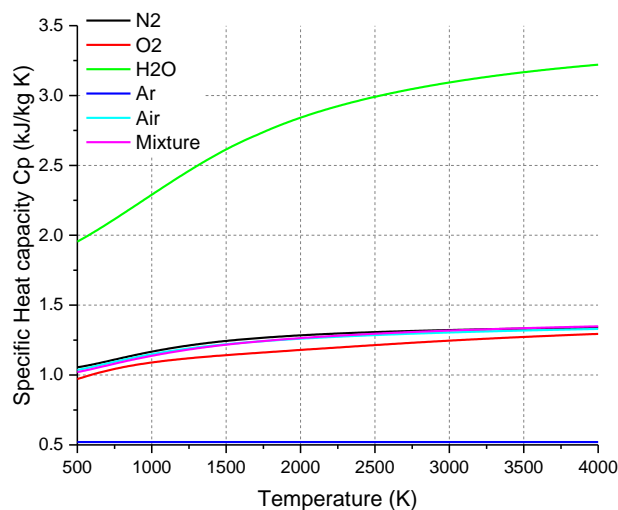


Figure 5-2. The specific heat capacity of the inlet charge mixture and gases

5.2 Results

5.2.1 Ignition Delay

To examine the auto-ignition behavior, the ignition delay time for the test fuels with water was calculated using CHEMKIN. Model calculations were performed for homogeneous adiabatic with a constant volume reactor. A comparison of simulated ignition delay times with water and without water is presented in Figure 5-3. Overall, the temperature increases ignition delay time is decreased, except for iso-Octane. The total average of the ignition time changes is 7.6%, 8.3%, 6.9%, and 10%, in order of iso-Octane, toluene, n-Butanol, and Ethanol. From 769.2 K to 833.3 K, the ignition delay time of iso-Octane increased. This is a negative temperature coefficient (NTC) behavior. This behavior is well explained from previous research [108,110,111]. Several studies [63,65,68,88] indicated longer ignition delay with water addition. The result shown in Figure 5-3 is contradictory to the earlier studies. It is mainly because the earlier studies

observed entire effects of water addition in the ignition delay. In the study [64], the chemical effect of water was observed and compared with the dilution effect and the thermal effect. Due to the chemical effect of water, a shorter ignition delay was observed as similar with the results from the present study. Therefore, the chemical effect is weaker than the other effects: intake charge cooling and heat capacity increase, so that the total effects of water lead to an increase of ignition delay time.

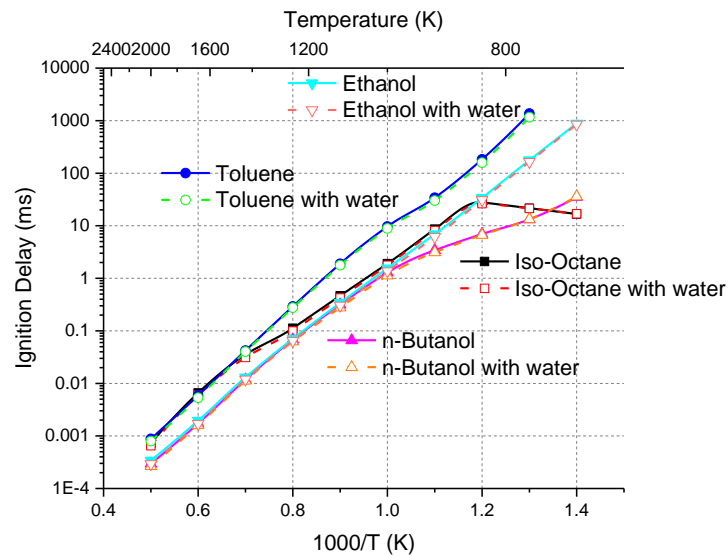
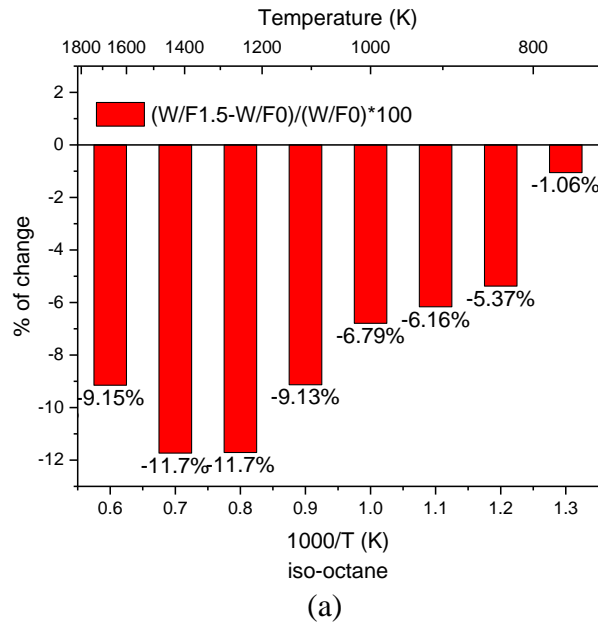


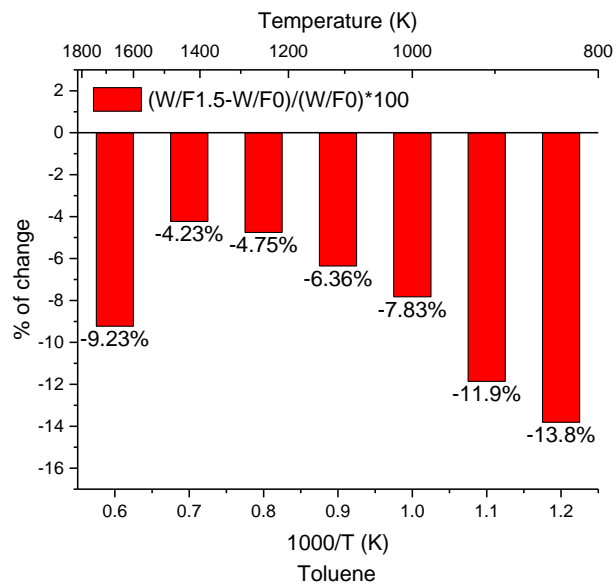
Figure 5-3. Ignition delay time for iso-Octane, Toluene, Ethanol, and n-Butanol with water (open symbols) without water (closed symbols)

A detailed comparison was made with regard to the effect of water on the ignition delay in Figure 5-4. In most cases, the ignition delay time was shorter with water than without water. This indicates that the chemical effect of water is to promote the auto-ignition behavior. However, the trend of ignition delay time with increasing the temperature is different. In the case of iso-Octane, the highest chemical effect of water was observed at 1250 K and 1428.6 K condition. Toluene showed that the most ignition

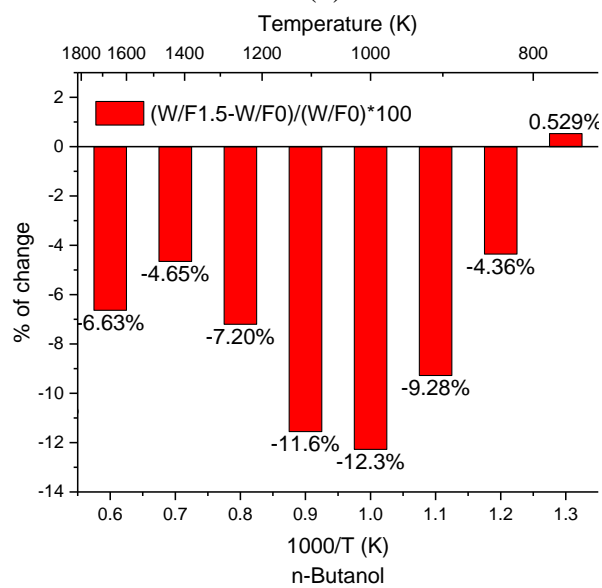
delay time changes in 833.3 K and decrease by increasing the temperature. However, at the highest temperature, 2000K, the chemical effect of water was increased. Ethanol and n-Butanol showed relatively similar trend of the ignition delay time change. Although at the minimum temperature, 769.2 K, the water led the ignition delay time increase in case of n-Butanol, the amount of effect of water was increase by increasing the temperature to 1000 K. After a temperature of 1000 K, the effectiveness of water decreases, and then increases again at 2000 K.

As a result of this observation, it is shown that there is a chemical effect of water on auto-ignition. On all of tested fuel, the ignition delay time is decreased by increasing temperature. Moreover, depending on the type of fuel and the temperature, the trends of chemical effectiveness of water are shown differently.





(b)



(c)

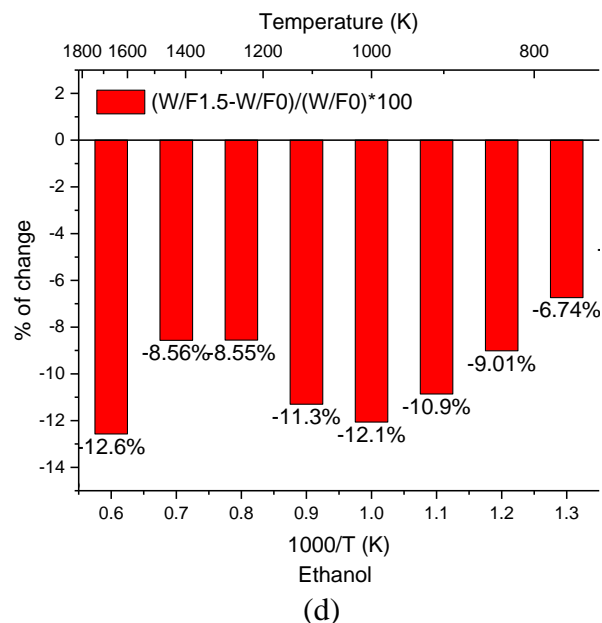


Figure 5-4. Ignition delay time changes due to water on (a) iso-Octane, (b) Toluene, (c) n-Butanol, and (d) Ethanol. Negative values indicate water shortens ignition delay

5.2.2 Sensitivity and Reaction Pathway Analyses

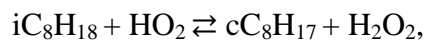
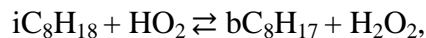
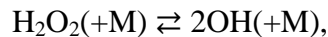
The chemical effect of water on high octane number fuels was computed using CHEMKIN with a chemical kinetic mechanism [130] by measuring the ignition delay time. Though the ignition delay analysis provided a valuable indication of auto-ignition characteristics with water, the fundamental understanding on the chemical effect of water is not obtained through the ignition delay analysis alone.

In order to reveal the important chemical reactions affected during the auto-ignition, a sensitivity and reaction pathway analyses were conducted at same condition of previous section. Because the analyses have to calculate each reaction at each condition, it required significant computational resources to run all cases. Therefore, in this section, only three different temperature conditions of 909 K, 1250 K, and 1666 K were

considered. Also, 3 different time steps, 20% fuel burn, 50% fuel burn and auto-ignition were compared.

(a) iso-Octane

Figure 5-5 shows a reaction pathway for iso-Octane in the presence of water and without water at 909K. Overall the reaction pathways are largely the same at all time steps. However, relative rates of production are slightly different. At the beginning of iso-Octane oxidation (20% fuel burn), H₂O is produced by the β-scission of aC₈H₁₇, bC₈H₁₇, cC₈H₁₇, and dC₈H₁₇ radicals. It is also observed from the experiments conducted by Le Cong and Dagaut [96], due to a reaction $H + O_2 + M \rightleftharpoons HO_2 + M$, a higher concentration of HO₂ was measured. In addition, the peak of OH concentration was measured to be 13% higher with H₂O addition. A higher the peak of OH concentration with water addition is also found in the study by Mazas et al. [97]. With water, because more OH radical is available, those reactions are promoted around 1% more on the basis of the relative rate of production. Similar observations are made at the 50% fuel burn and auto-ignition. Mainly due to higher available OH radicals, reactions involving OH are promoted around 1% relative rate of production, and those led to faster ignition delay compared to without water. Based on sensitivity analysis, the results identified the same key reactions for H₂O evaluated in case of with water and without water. The primary reactions controlling the H₂O profiles are



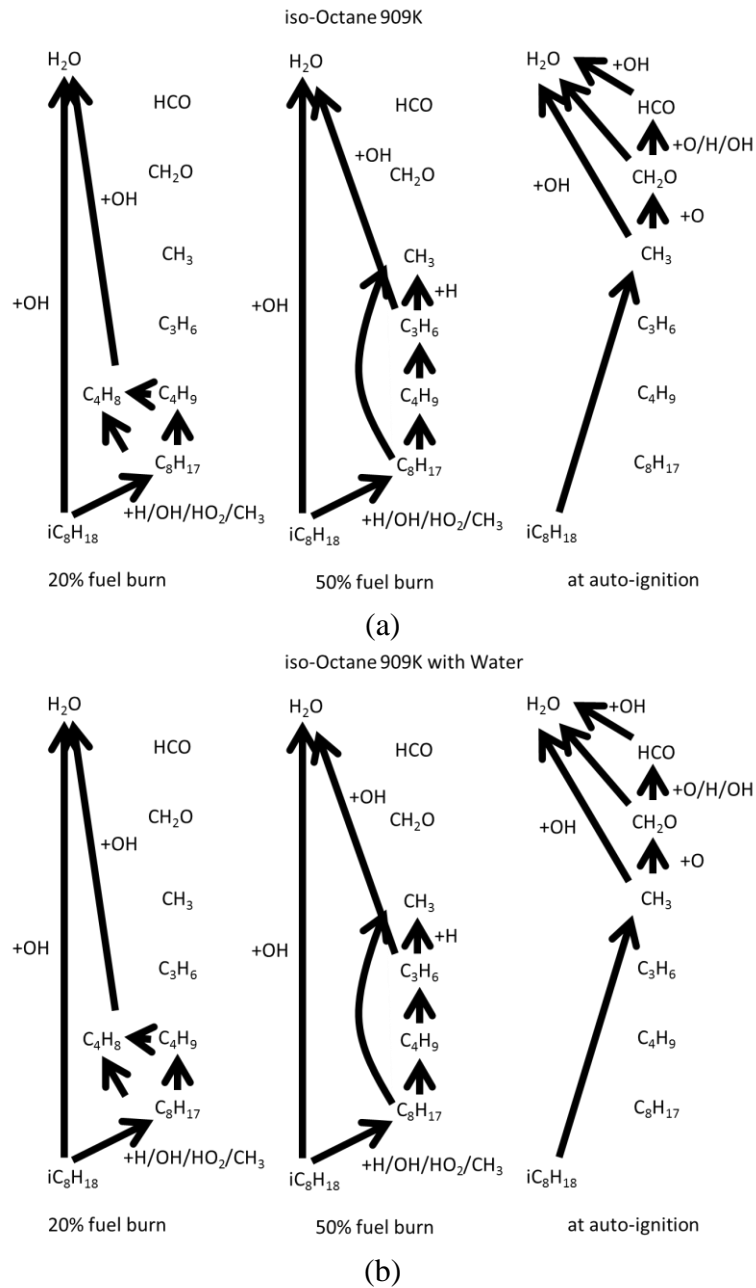
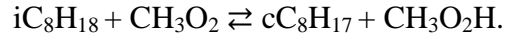
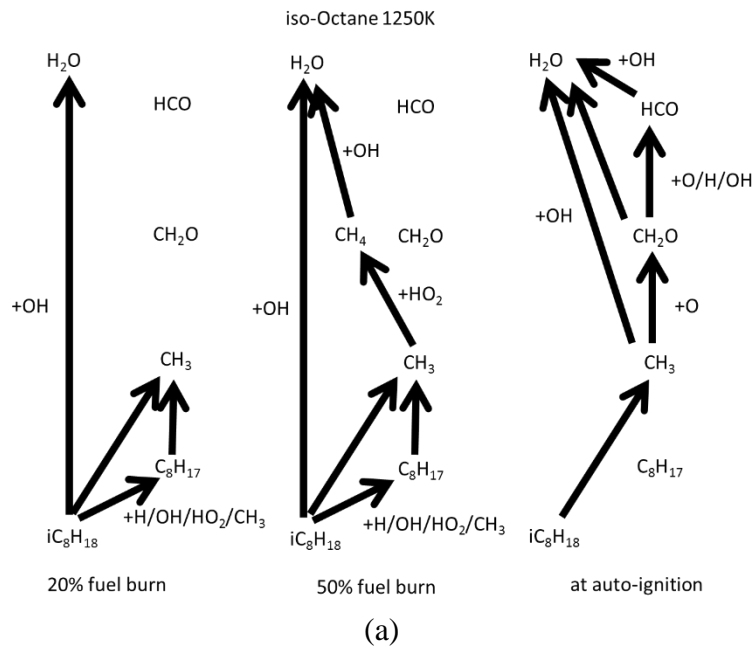


Figure 5-5. Reaction pathway for iso-Octane at 909K (a) with H₂O and (b) without H₂O

A reaction pathway of iso-Octane in the presence of water is slightly different at higher temperature 1250 K as shown in Figure 5-6. Major different reaction is CH₄ + OH

$\rightleftharpoons \text{CH}_3 + \text{H}_2\text{O}$. In the case of no water, methane (CH_4) reacts with OH radical to produce a methyl radical (CH_3). However, the reverse reaction occurs with water as well. Methyl radical combines with water and produces more methane and CH radical which is a highly reactive radical as shown in Figure 5-7. The top 5 most sensitive reactions are examined. The reactions do not change by adding H_2O or not, but the orders of the reactions (magnitude of sensitivity coefficient) are changed. Without H_2O , $\text{H} + \text{O}_2 \rightleftharpoons \text{O} + \text{OH}$ reaction is the top reaction but with H_2O , this reaction becomes the second most major reaction and $\text{H} + \text{O}_2(+\text{M}) \rightleftharpoons \text{HO}_2(+\text{M})$ comes first.



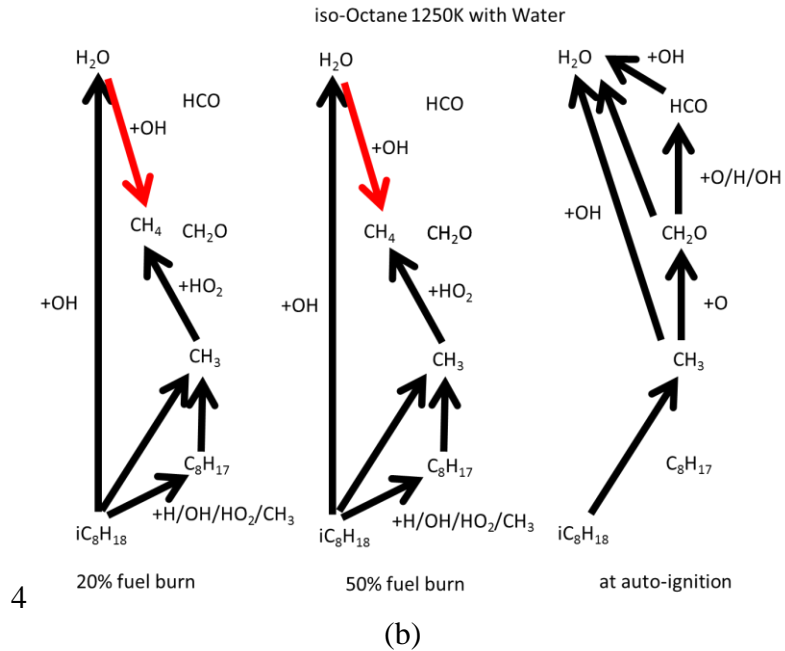


Figure 5-6. Reaction pathway for iso-Octane at 1250K (a) with H₂O and (b) without H₂O

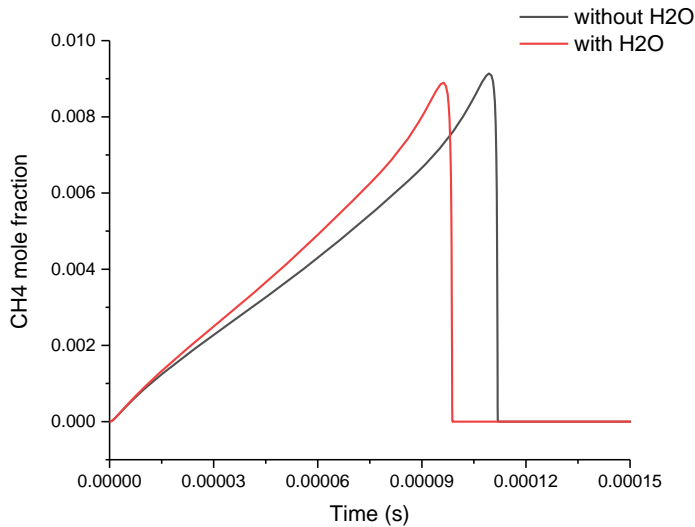
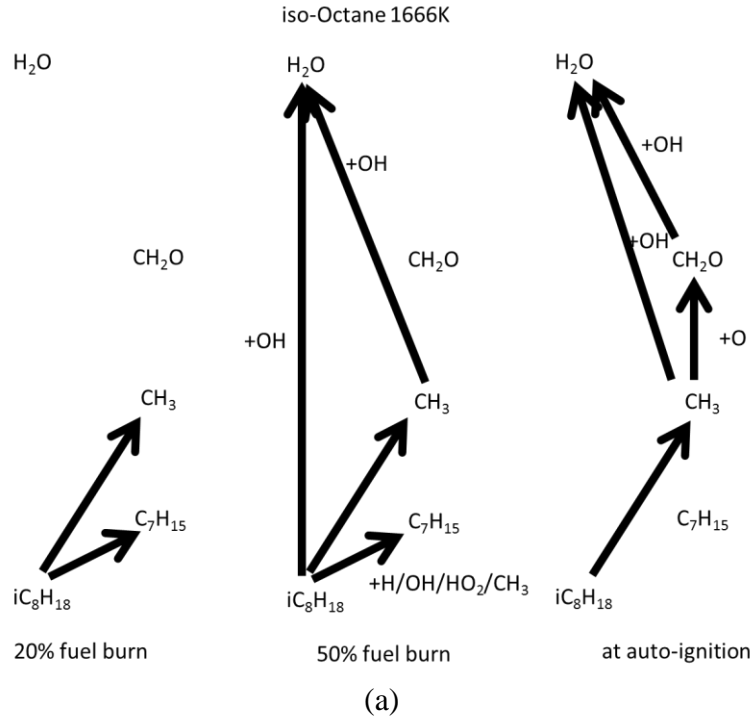


Figure 5-7. Evolution of CH₄ in the oxidation of iso-Octane with / without H₂O

At the highest temperature, 1666K, overall the reaction pathways are pretty much the same at all time steps, as with the 909K condition. Although the reactions, $\text{CH}_4 + \text{OH} \rightleftharpoons \text{CH}_3 + \text{H}_2\text{O}$ and $\text{OH} + \text{H}_2 \rightleftharpoons \text{H} + \text{H}_2\text{O}$, are not shown in the reaction pathways in Figure 5-8, those reverse reactions occur with water. It means that OH radical is combined with CH₄ and H₂ then H₂O is generated. However, in the case of H₂O addition,

those reactions occur reversely. H_2O contributes to produce more OH radical. In this temperature, $\text{H} + \text{O}_2 \rightleftharpoons \text{O} + \text{OH}$ reaction has top sensitive reaction related to H_2O with or without H_2O . However, similar with the 1250K condition, $\text{H} + \text{O}_2(+\text{M}) \rightleftharpoons \text{HO}_2(+\text{M})$ arises more important reaction with the presence of H_2O .

Overall, the major changes of iso-Octane oxidation process with addition of water is that H_2O helps to produce more OH radical and generate more intermediate species such as CH_4 and H_2 .



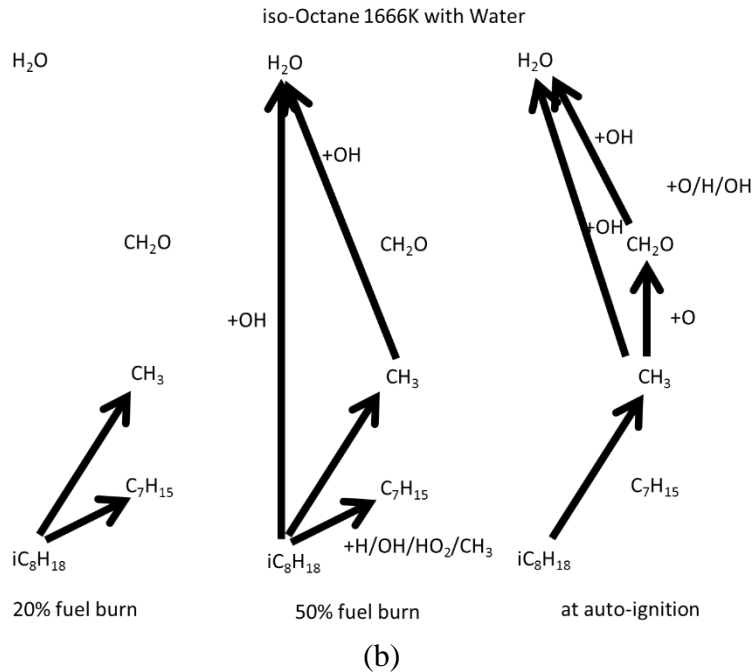


Figure 5-8. Reaction pathway for iso-Octane at 1666K (a) with H₂O and (b) without H₂O

(b) Toluene

Figure 5-9 shows a reaction pathway of toluene in the presence of water at 909K. Unlike the reaction pathway for iso-Octane, the reaction pathway of toluene at ignition point is very different with H₂O and without H₂O. In the case with H₂O, H₂O produces more hydrogen peroxide (H₂O₂) which is a strong oxidizer. Also, relative rate of production of OH radical involved reactions ($C_6H_5CH_3 + OH \rightleftharpoons C_6H_4CH_3 + H_2O$, and $C_6H_5CH_3 + OH \rightleftharpoons C_6H_5CH_2 + H_2O$) are slightly higher in H₂O case, because of higher number of available OH radicals as in the iso-Octane case. Therefore, at the same temperature (909K), the effect of the presence of H₂O on the ignition delay of toluene is higher than its effect on iso-Octane. The study by Andrae et al. [137] states the detail of the toluene oxidation process. At the beginning of the oxidation process of toluene, toluene reacts with oxygen and produces benzyl ($C_6H_5CH_2$) and hydroperoxy radicals. As the radical pool builds up with the reaction with the oxygen, the reaction $C_6H_5CH_3 + OH$

$\rightleftharpoons \text{C}_6\text{H}_5\text{CH}_2 + \text{H}_2\text{O}$ starts to be dominant. Therefore, the increase of this reaction rate with H_2O addition affects the auto-ignition process. Based on sensitivity analysis, the key reactions remain unchanged with water and without water.

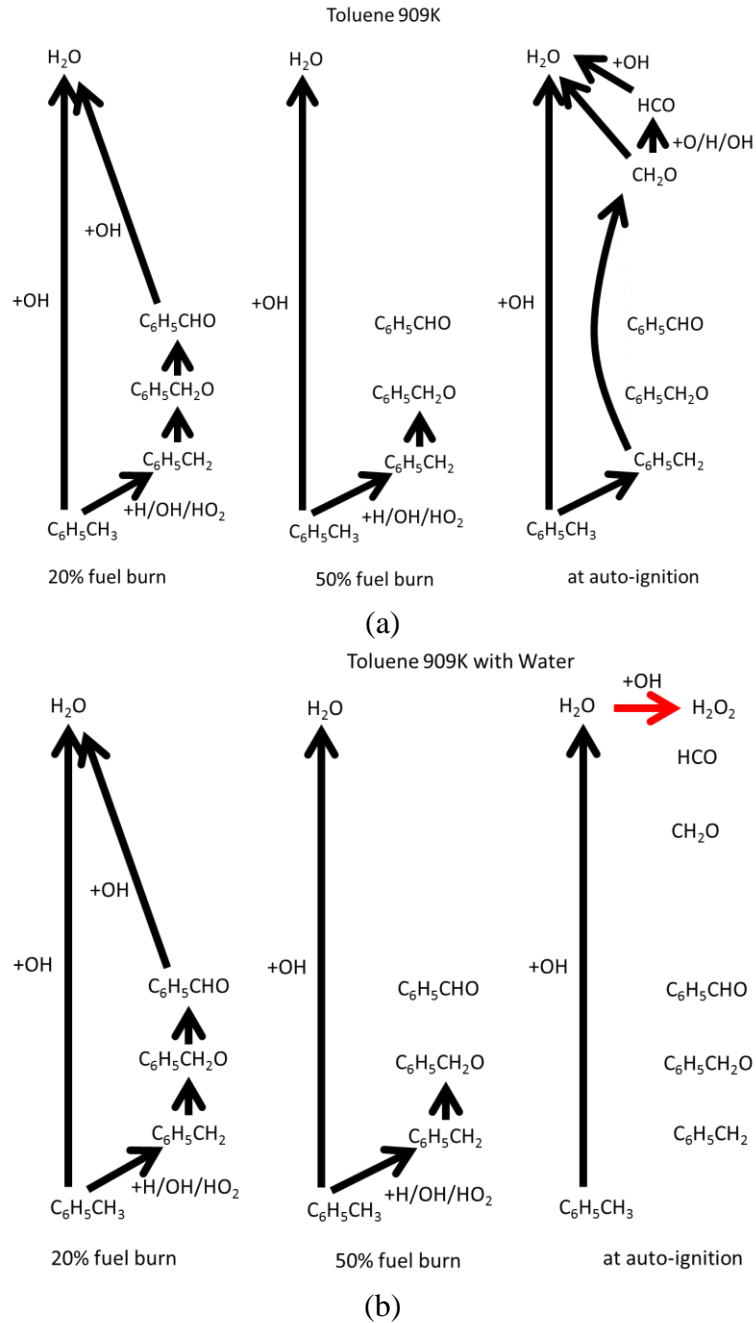


Figure 5-9. Reaction pathway for Toluene at 909K (a) with H_2O and (b) without H_2O

The reaction pathway for toluene in the presence of water at 1250K is shown in Figure 5-10. Like the reaction pathway for iso-Octane at 909K, the overall the reaction pathways are similar at all time steps with H₂O and without H₂O. The only differences are the rate of production of the OH radical. The top 5 most sensitive reactions are also the same with or without H₂O.

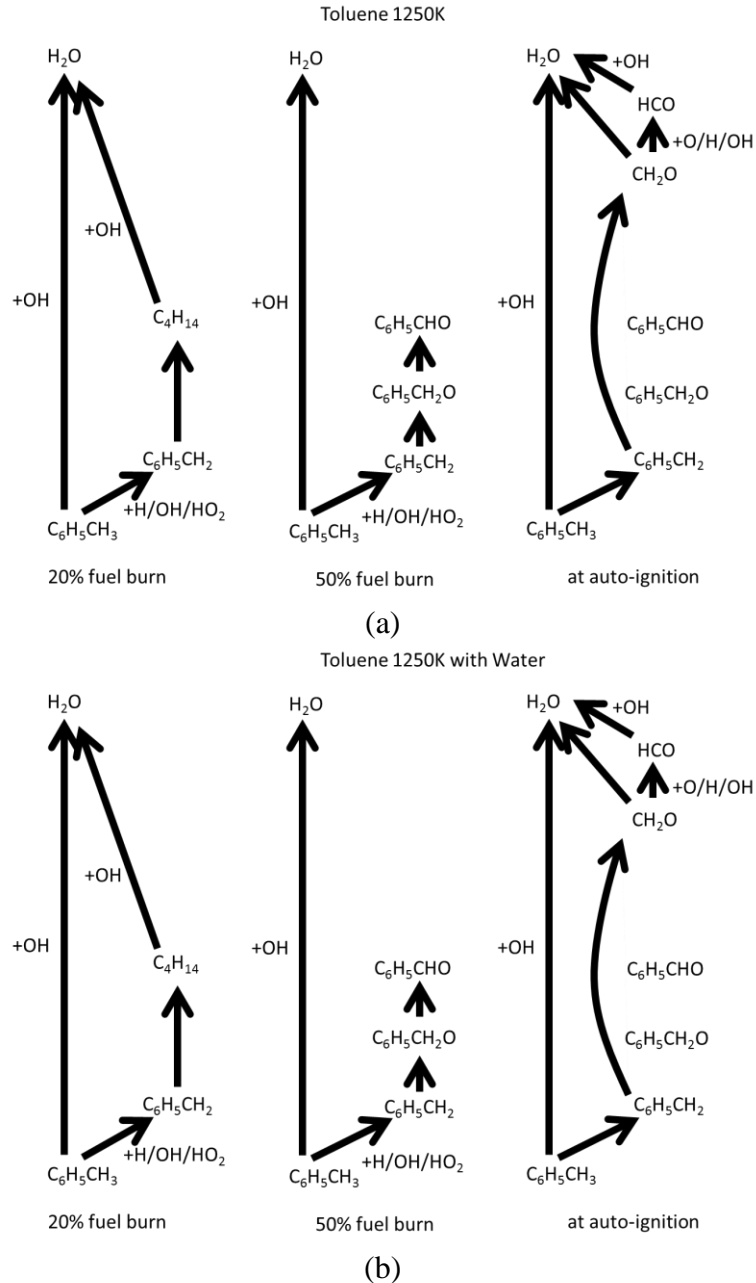
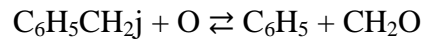
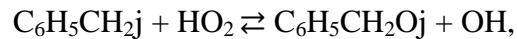
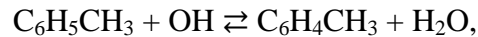
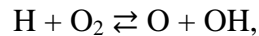


Figure 5-10. Reaction pathway for Toluene at 1250K (a) with H₂O and (b) without H₂O

At the highest temperature, 1666K, the major distinct reactions are $C_6H_5CH_2 + O \rightleftharpoons C_6H_5 + CH_2O$ and $CH_2O + OH \rightleftharpoons HCO + H_2O$. Those reactions present at the 50% fuel burn point without H_2O , but those reactions occur at an earlier time step (20% fuel burn) with H_2O addition. This is mainly due to the larger amount of O and OH availability due to H_2O breakdown. Although it is not shown in the pathway diagram, H_2O produces more hydrogen peroxide (H_2O_2) by combining with the hydroperoxyl radical (HO_2) as with the reaction pathway at 909K. In addition, more formyl radical (HCO) is generated by H-atom abstraction from formaldehyde (CH_2O), $CH_2O + X \rightleftharpoons HCO + HX$. Moreover, formyl radical (HCO) is an important radical for the combustion of hydrocarbons because it changes the chain termination rate and branching rate [138]. Otherwise, the results of sensitivity analysis are not affected by water addition. The top 5 major reactions related to H_2O are



As a result, the effect of water addition on toluene is shown to be similar to that on iso-Octane oxidation. More OH and O are available due to H_2O breakdown, and at some point, the rate of production for hydrogen peroxide (H_2O_2) and formyl radical (HCO) are changed by adding water.

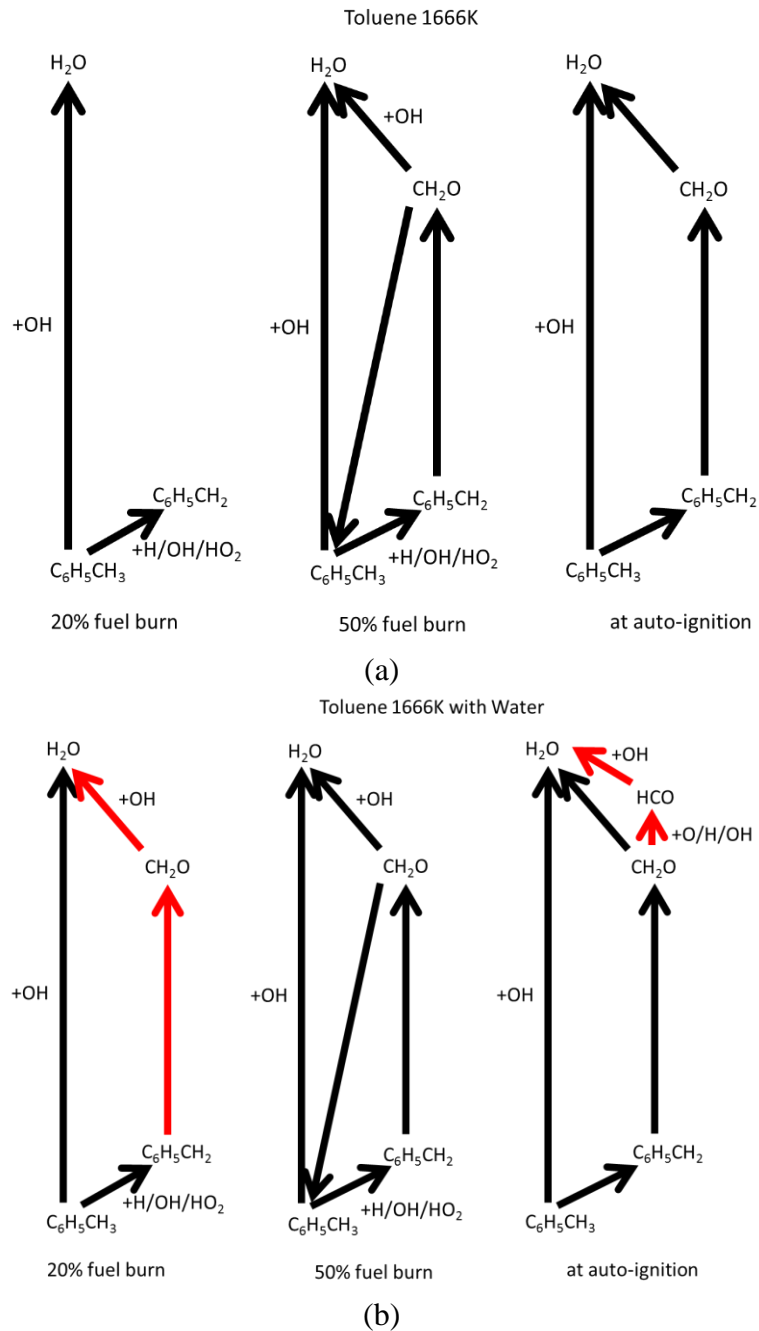
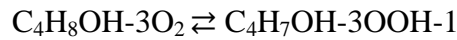
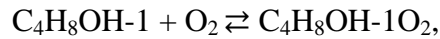
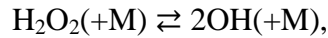
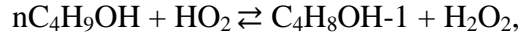


Figure 5-11. Reaction pathway for Toluene at 1666K (a) with H_2O and (b) without H_2O

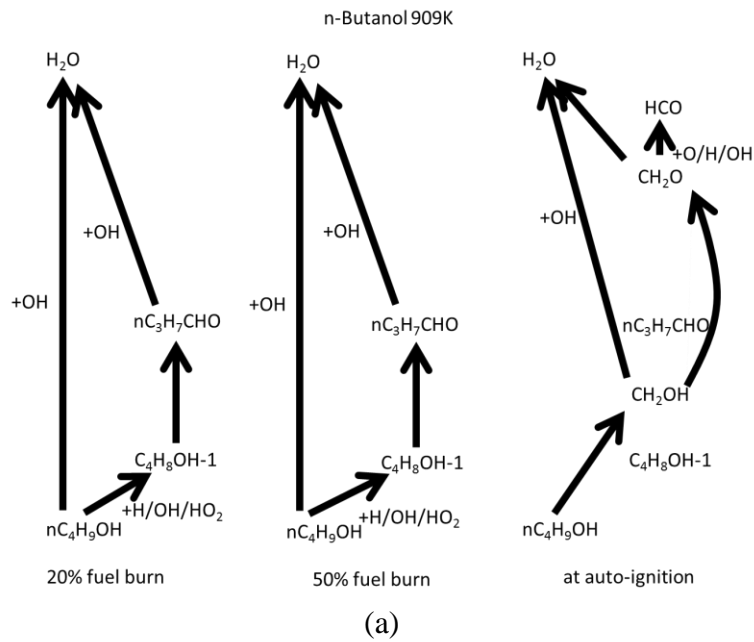
(c) n-Butanol

In Figure 5-12, a reaction pathway for n-Butanol in the presence of water at 909K is shown. In the early stages of combustion, 20% fuel burn and 50% fuel burn, the reaction pathways are pretty much the same, except the relative rate of production of the

to the OH radical. These are slightly high (around 1%) as observed for iso-Octane and toluene. At the ignition point, when H₂O is not present n-Butanol finishes a dissociation reaction, but when H₂O is present n-Butanol is still dissociating to C₄H₈OH. It is predicted that more OH radical is available at the end of combustion process. As a result of sensitivity analysis, key reactions related to H₂O are



are the same as with or without H₂O addition.



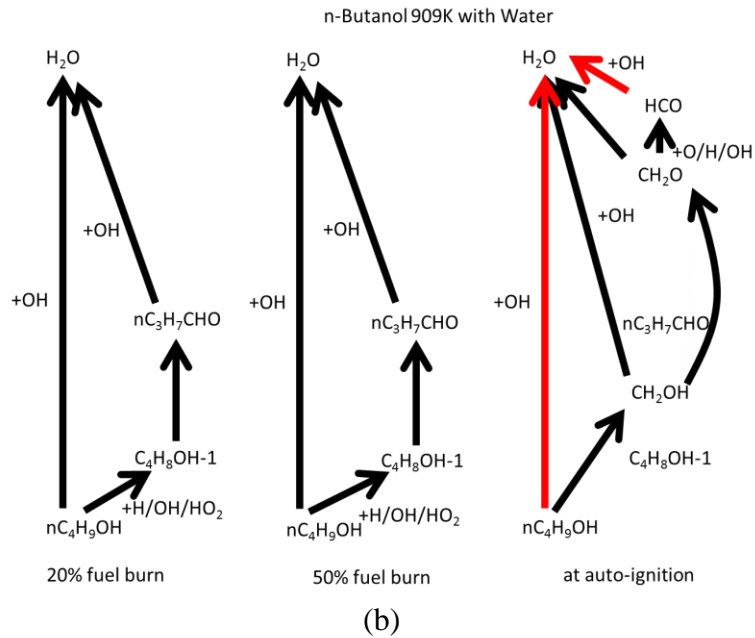


Figure 5-12. Reaction pathway for n-Butanol at 909K (a) with H₂O and (b) without H₂O

The reaction pathway of n-Butanol in the presence of water at 1250K is shown in Figure 5-13. Like the reaction pathway for iso-Octane at 909K and toluene at 1250K, the overall the reaction pathways are largely the same at all time steps with H₂O or without H₂O addition. The only differences are the rate of production of OH radical. The top 5 most sensitive reactions are also the same with or without H₂O addition.

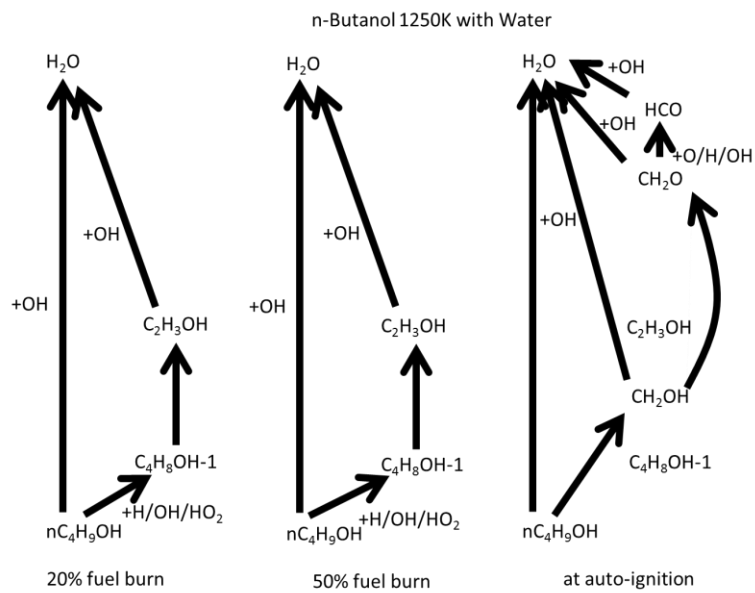
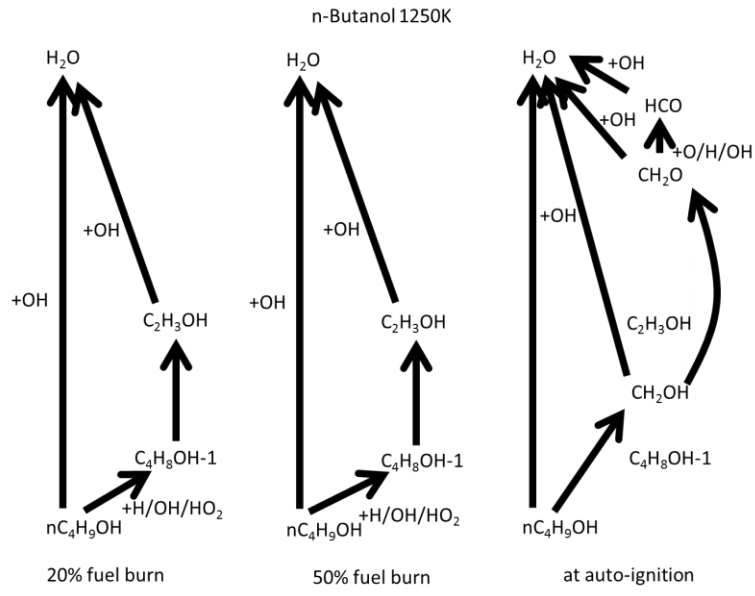


Figure 5-13. Reaction pathway for n-Butanol at 1250K (a) with H₂O and (b) without H₂O

At 1666K, the reaction pathways related to H₂O are the same at all time steps, as with the 1250K condition. In addition, the top 5 reactions are also the same with or without H₂O addition, based on sensitivity analysis.

As a result, the effect of water addition on n-Butanol is not clearly shown at all stages of time steps and temperatures. As explained earlier, it is expected that more OH radical leads to a shorter ignition delay.

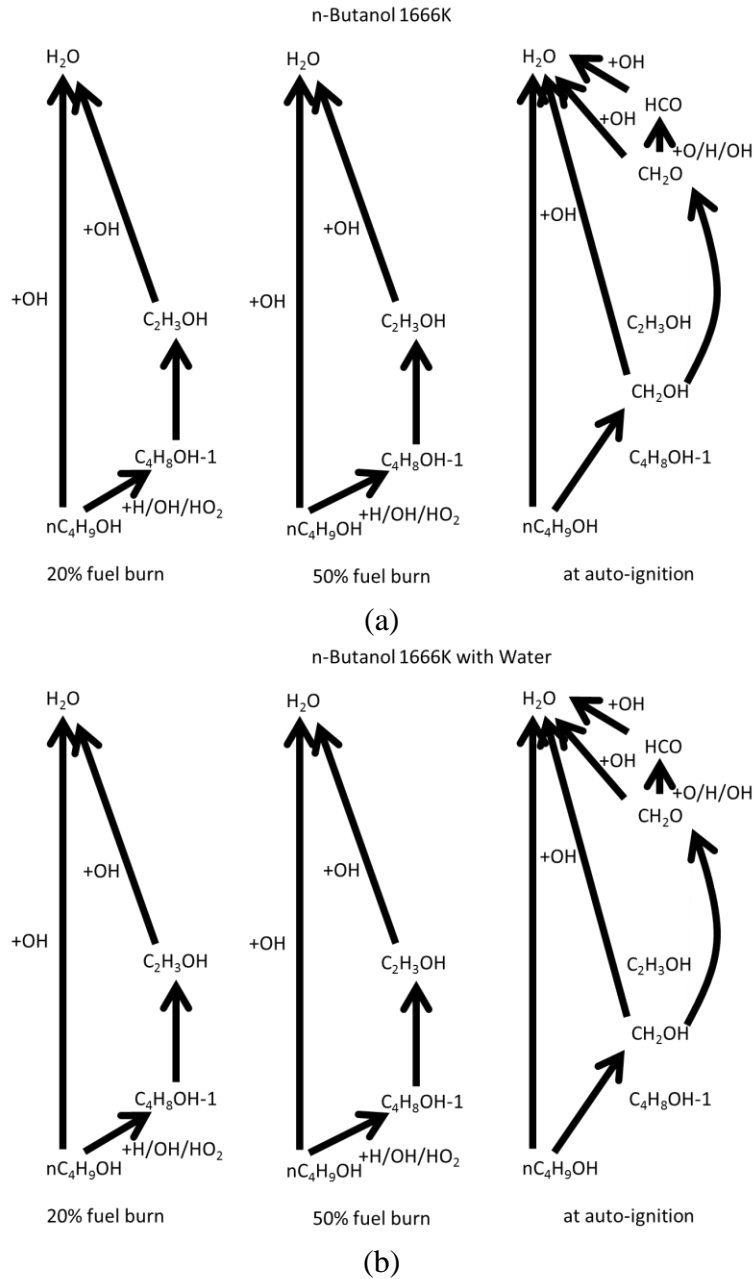
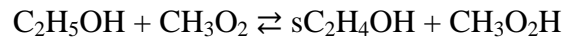
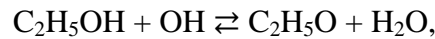
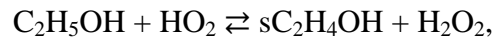
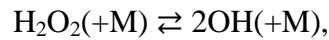


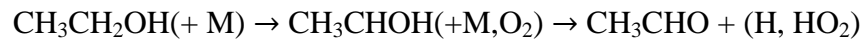
Figure 5-14. Reaction pathway for n-Butanol at 1666K (a) with H₂O and (b) without H₂O

(d) Ethanol

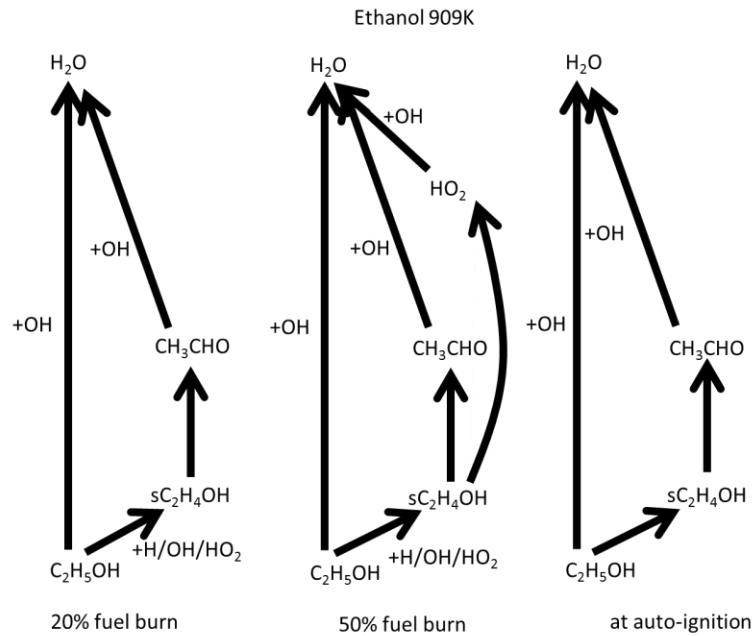
The reaction pathway for Ethanol in the presence of water at 909K is shown in Figure 5-15. In the early stage of combustion, the reaction pathways are identical except for a slightly higher rate of OH related reactions. However at the ignition stage, hydroperoxyl radical (HO_2) related reactions are enhanced with water addition. This reaction is $\text{H}_2\text{O}_2 + \text{OH} \rightleftharpoons \text{H}_2\text{O} + \text{HO}_2$ and water combines with hydroperoxyl radical, then hydrogen peroxide (H_2O_2) and OH radical are produced. Similar reactions are shown for toluene for the 909K and 1666K cases. At this temperature, the order of top five H_2O sensitive key reactions is not affected by water addition although the normalized sensitivity coefficients are decreased. The top five reactions are



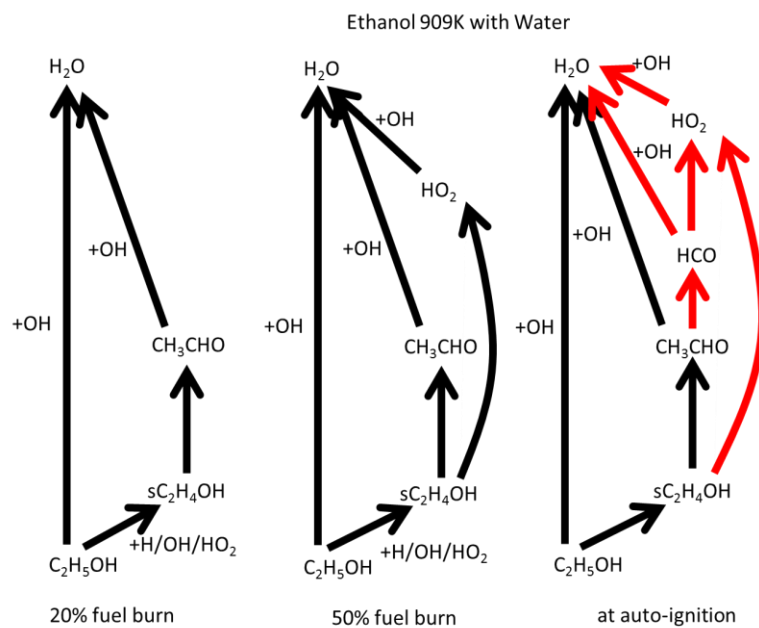
The ethanol oxidation mechanism by Norton and Dryer [139] discussed three distinct reaction pathways. Those are



Among three of reactions, the first and the last reactions are H_2O sensitive key reactions. Therefore, even though the change in these reaction rates is small by adding H_2O , H_2O affects the entire oxidation process of Ethanol.



(a)

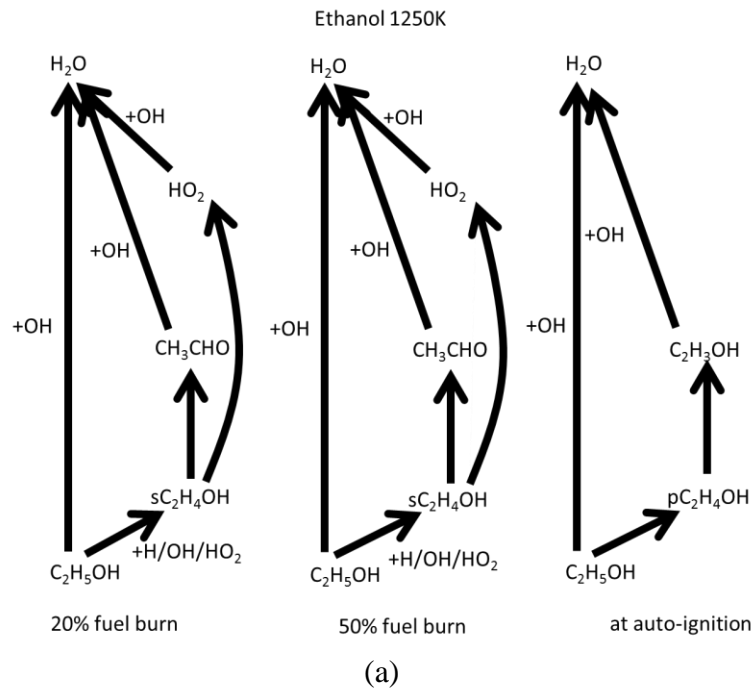


(b)

Figure 5-15. Reaction pathway for Ethanol at 909K (a) with H_2O and (b) without H_2O

In Figure 5-16, a reaction pathway of Ethanol in the presence of water at 1250K is shown. As with the reaction pathway at 909K, overall the reaction pathways at the early stages are same with H_2O and without H_2O . On the other hand, at the auto-ignition, it is

shown that higher reaction rate reacted with formaldehyde (CH_2O) with H_2O addition. Formaldehyde is an important intermediate species in the hydrocarbons and oxygenated hydrocarbon oxidation process. Previous research has shown that formaldehyde promotes the ignition process in the presence of oxygen [140]. As a result of sensitivity analysis, the fourth most sensitive reaction to H_2O , $\text{CH}_3 + \text{HO}_2 \rightleftharpoons \text{CH}_3\text{O} + \text{OH}$, without water is slightly promoted with water addition, and it turns to the third most important reaction.



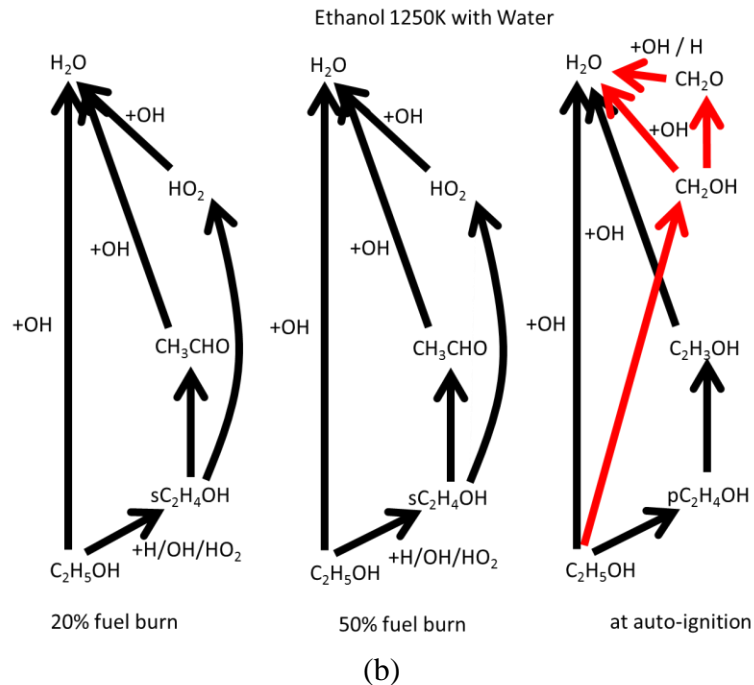
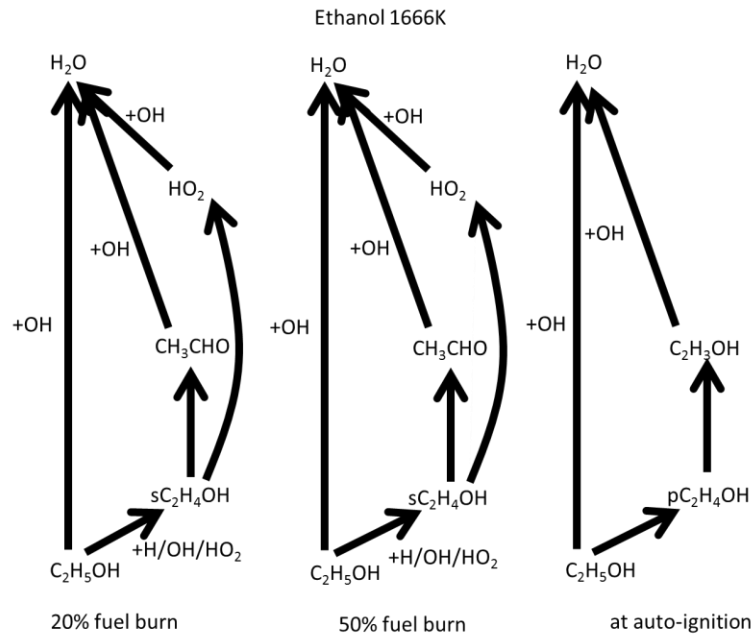


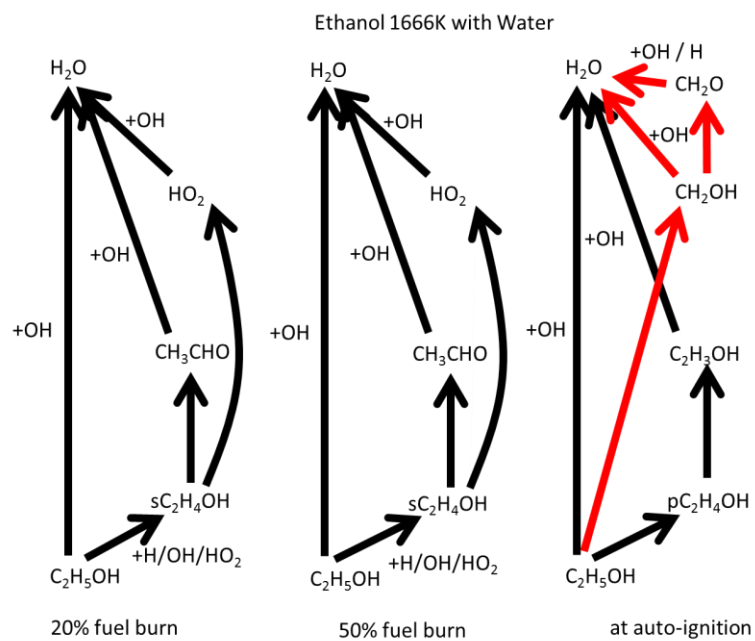
Figure 5-16. Reaction pathway for Ethanol at 1250K (a) with H₂O and (b) without H₂O

At 1666K, the reaction pathways related to H₂O are the same at all time steps as with the 1250K condition, as shown in Figure 5-17. In addition, the top 5 reactions are also the same with and without H₂O addition, based on sensitivity analysis.

As a result, one potential effect of water addition in Ethanol is observed at 1250K and 1666K, which is the formaldehyde (CH₂O) related reaction. The reaction rate is promoted by water addition and because it is an ignition aid in the presence of oxygen, it may lead to a faster ignition process.



(a)



(b)

Figure 5-17. Reaction pathway for Ethanol at 1666K (a) with H₂O and (b) without H₂O

5.3. Conclusion

In this chapter, numerical calculations of the chemical effect of water addition with high octane number fuels and oxygenated fuels including iso-Octane, toluene, n-Butanol, and Ethanol were presented. Using a chemical reaction simulation tool, CHEMKIN, the simulations have been conducted on the change of hydrocarbon and oxygenated hydrocarbon oxidation processes with water addition by examining ignition delay, sensitivity analysis and chemical reaction pathway analysis.

To examine the chemical effect of water on the combustion process, the homogeneous batch reactor model, mimicking a constant volume chamber was applied. Moreover, to eliminate the thermal effect of water on combustion, the composition of the intake charge was modified to have the same heat capacity with water and without water.

As a first step of the study, the change of the ignition delay due to water addition was quantified. The results showed out that a faster ignition delay, around 5-10%, was observed with water, although the magnitude of this enhancement of ignition varied with temperature and type of fuel. The results show that there is a chemical effect of water on auto-ignition.

To verify in more detail the chemical effect of water on the ignition process, the sensitivity analysis and the reaction pathway analysis were performed. All of the chemical reactions change due to the present of water is a matter to more OH radical availability due to H₂O decomposition. Therefore, there were lots of chemical reaction rates affected, increased or decreased, by having more OH radical. For example, $\text{CH}_4 + \text{OH} \rightleftharpoons \text{CH}_3 + \text{H}_2\text{O}$ occurred in the opposite direction, in the case of iso-Octane at 1250K. H₂O led to production of hydrogen peroxide (H₂O₂) by combining with hydroperoxyl

radical (HO_2) in the case of toluene case. Moreover, more formaldehyde (CH_2O) was formed due to water addition during the combustion of Ethanol.

Chapter 6

Conclusions and Recommendations for Future Work

6.1. Conclusion

The conclusions of the dissertation are summarized as follows.

In Chapter 3, this work included a wide scope of research to understand condensation generated inside of the charge air cooler. Using a 1.6L GDI turbocharged engine, experiments were conducted to understand how and how much condensates were generated at specific air humidity and engine conditions. The following conclusions were observed for the condensate generation.

- At low loads, the boost is low enough that water does not condense
- At high loads, the large charge air flow exceeds the cooling capacity of the CAC so the charge air remains too hot for water condensation
- In between, significant rates of water condensation can occur

Moreover, to understand the ingestion of condensates into the engine cylinders, the hard acceleration was applied and quantitatively correlated the amount of condensation and number of abnormal combustion behavior such as misfire and slowburn

events under different engine conditions. The following amount of abnormal combustion was quantified in over a total of 492 cycles.

- 47 cycles of slowburn were observed with 200ml and 2750 rpm and 33% of pedal position
- 156 cycles of slowburn and 1-2 cycles of misfire were observed with 150ml and 3000rpm and 40% of pedal position
- 256 cycles of slowburn and 21 cycles of misfire were measured with 200ml and 3000rpm and 40% of pedal position

The next a condensation separator was designed and tested to prevent the abnormal combustion behavior due to the ingestion of condensates. Therefore, the numerical simulation of the pressure drop and the separation efficiency for the charge air cooler condensation separator was developed. Empirical equations for the pressure drop and the separation efficiency were derived based on the simulation results. In addition prototype separators were built and engine tested. All of the simulation and experiment results matched well with the empirical equations.

In Chapter 4, the effect of water on auto-ignition was examined using a modified CFR engine. Three test fuels gasoline, PRF, and TRF which have similar RON values were used for this test at various intake pressures and amount of water addition. The tests were done in two steps. The first test was done with constant intake air temperature and ϕ to exclude the effects of intake air cooling. From the results of this test, regardless of the intake charge temperature cooling effect due to water, the intake charge property changes due to water addition suppressed the auto-ignition process. It was shown that when a larger amount of water was injected into the intake air, a higher critical compression ratio

was measured for all fuels: premium gasoline, PRF, and TRF. This trend is more significant at lower intake air pressure. The effect of pressure on water addition had similar trends to all test fuels and amounts of water adding consistently indicating that auto-ignition is promoted as the intake air pressure increases.

Also, the heat release, the bulk in-cylinder temperature, and the bulk in-cylinder pressure analyses were applied to examine the effect of the property change intake charge. The peak heat release rate noticeably decreases with increasing water-fuel ratio at constant compression ratio. However, there is a lack of evidence as to whether water addition in the intake air affects the combustion duration.

For the second part of CFR engine studies, the comparison of the effect of the intake air cooling and the effect of the intake air property changes was made. It was found that CCR change due to the intake air cooling or due to intake air property change when water-fuel ratio was 1.5, was similar.

Chapter 5 presented the numerical calculations of the chemical effect of water addition with high octane number fuels and oxygenated fuels including iso-Octane, toluene, n-Butanol, and Ethanol. Using chemical reaction simulation, CHEMKIN, the simulations have been conducted on the change of hydrocarbon and oxygenated hydrocarbon oxidation processes with water addition by examining ignition delay, sensitivity analysis and chemical reaction pathway analysis. At the beginning of the study, the change of the ignition delay due to water addition was quantified. On all of the test fuels, the ignition delay time is decreased by increasing temperature. Moreover, the chemical effectiveness of water is different depending on the type of fuel and the temperature.

Then, the sensitivity analysis and the reaction pathway analysis were carried out to verify in more detail of the chemical effect of water on the combustion process. Common observations made through all kind of fuels were more OH radical with H₂O addition due to H₂O decomposition. Therefore, many chemical reactions were affected by water addition. For example, the higher rate of reverse reaction of $\text{CH}_4 + \text{OH} \rightleftharpoons \text{CH}_3 + \text{H}_2\text{O}$ found in the case of iso-Octane at 1250K. H₂O addition led to production of hydrogen peroxide (H₂O₂) by combining with hydroperoxyl radical (HO₂) in the case of toluene. Moreover, more formaldehyde (CH₂O) was formed due to water addition during Ethanol combustion process.

Overall, the automotive industry has been shifting towards downsized, boosted, and direct fuel injection engines to achieve high efficiency. Boosted and downsized engines operate under higher in-cylinder pressure and temperature, leading to increased possibility of abnormal combustion events like knock. As a result, the compression ratio and boost pressure in modern engines are restricted, which in-turn limits the engine efficiency and power. A charge air cooler is utilized to manage the intake air temperature which is one of factors controlling the likelihood of knock events. However the condensate generated and ingested into the engine cylinder in certain conditions is a potential issue.

Through the studies presented in this thesis, some potential contributions to high efficiency gasoline engines have been obtained. By collecting the condensate which is accumulated in the charge air cooler, the abnormal combustion behavior such as misfire or slowburn can be prevented, and also the collected water condensate can be utilized as a supply source for a water injection system. Water injection is known to be an effective

technique to manage knock, but requires a customer to refill the water periodically. So, the main challenges of the water injection system are how to achieve high efficiency of the system with a given amount of water and how to make self-sufficient system, if possible. Because the detailed effect of water has been shown in previous studies, it is expected that the gasoline engine could achieve higher compression ratio with a water injection system which leads higher thermal efficiency. In addition, an engine with a water injection system could avoid knock limited operation condition. Therefore, the water injection system is able to improve the efficiency of the turbocharged and downsized gasoline engine.

6.2. Recommendations for Future Work

Used in the second study within this thesis, the CFR motored engine is a unique test equipment to observe the hydrocarbon oxidation process, and it is capable of operation over a wide range of pressure, temperature, fuel air ratio and so on. However the exhaust sampling device which was available with the CFR engine has a limited capability of measuring exhaust composition. Therefore, similar to the study done in Chapter 3, it is recommended to use Fourier Transform Infrared Spectroscopy (FTIR) to better quantify the exhaust composition to examine the effect of water. In addition, implementing a gas chromatography mass spectrometry (GC-MS) analysis is recommended for better understanding of intermediate species changes due to water addition.

In the third study, the chemical reaction calculation depends heavily on the on the chemical reaction mechanisms which was developed by other researchers. In addition, experimental validation is necessary even though de-coupling other effects of water and

the chemical effect of water is quite difficult. While the ignition delay and chemical reactions were derived by numerical calculation, the simulations may not guaranteed to match the actual test results. Thus, more fundamental experiments using shock tubes or rapid compression machines will be beneficial for future analysis.

Appendices

Appendix A. Condensation model description

This model has been developed by Chih-Kuang Kuan of Ford Motor Company starting with work done by Mehdi Abarham, while a graduate student at University of Michigan. This model was published in 2017, under the title of “An Experimental and Computational Analysis of Water Condensation Separator within a Charge Air Cooler” in the ASME 2017 ICEF technical conference.

The charge air coolers considered here are cross-flow, brick type, air to air heat exchangers. For this particular application, air flow paths are composed by bundles of straight rectangular passages separated by corrugated fins. Each individual flow passage has a characteristic length of about few millimeters in cross section and tens of centimeters in length, as shown in Figure A-1. The model treats the flow passage as a circular tube with an equivalent hydraulic diameter of the original rectangular flow passage. Under this L/D ratio, we can ideally use classic shear stress and heat transfer correlations for internal pipe flows. Mass transfer coefficient for water molecular

diffusion of water from the gas phase to the near wall can be approximated by momentum-mass transfer analogy when local Reynolds and Nusselt numbers are available. To simplify the problem, we consider film condensation alone. Liquid water is assumed to be a uniform thin film on the periphery of the flow passage, and may move due to shear stress from the air flow. Therefore, in this model, we use two computational domains: one is for the heat and mass transfer of charge air, and the other domain describes the transportation of the liquid water film.

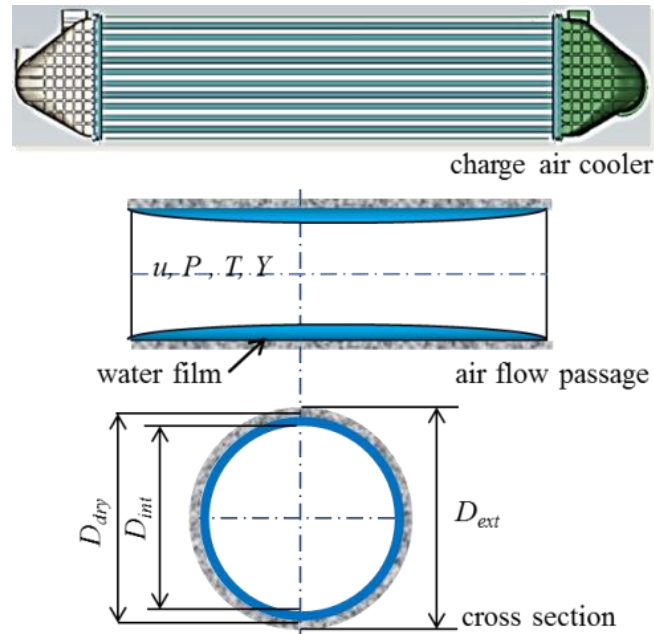


Figure A-1. The condensation model simulates a single air passage in a charge air cooler core containing computational domains for charge air and water film.

Without introducing other sources of water vapor, water mass fraction in air is minor composition compared to other non-condensable gas (around 4.6% in mass for saturated air at 40°C). Since the air mass flow rate in the cooler is assumed to be much higher than water condensation flux for the engine conditions considered, it is reasonable to treat this problem as quasi-steady state. We solve steady-state transport equations for mean charge air pressure P , temperature T , velocity u , density ρ , water mass fraction Y_w ,

as functions of axial distance from the cooler inlet, while a transient mass conservation equation is used for the movement of water film. Water film thickness will be much smaller than hydraulic diameter so that the cross section area variation of the air flow passage is negligible. This assumption makes the shear stress and heat transfer correlations for pipe flow and film condensation applicable. Body force on the thin film is small compared to shear stress of charge air exerted on the film surface, and hence an annular, uniform liquid film attached to the periphery of a flow passage is possible. Latent heat of condensation is ignored; it is negligible compared to cooler heat rejection under the engine conditions considered, and so is viscous dissipation.

$$\rho_g Au \frac{\partial Y_w}{\partial x} = -\dot{m}_w \quad (\text{A-1})$$

$$\rho_g u \frac{\partial u}{\partial x} = -\frac{\partial P}{\partial x} - \frac{1}{2} f \frac{\rho_g u^2}{D_{int}} \quad (\text{A-2})$$

$$\rho_g Auc_p \frac{\partial T}{\partial x} = \frac{\partial}{\partial x} \left(\frac{(T - T_w)}{R_{conv} + R_{cond}} \right) \quad (\text{A-3})$$

Equation (A-1) is the mass conservation of water vapor, momentum, energy equations for air flow in this model. The term \dot{m}_w on the right hand side of eq. (A-1) is the water mass flux due to condensation. It is a source term contributing to the liquid water film given in eq. (A-9). Bulk flow velocity u and pressure P are calculated in momentum equation as given in eq. (A-2). Friction loss is modeled by the Darcy–Weisbach equation where the Darcy friction factor, f , is derived from Zigrang-Sylvester’s correlation with local Reynolds number, roughness, and hydraulic diameter D_{int} [141].

$$R_{conv} = 1/(k_g Nu\pi)$$

$$R_{cond} = \frac{\ln(D_{dry} / D_{int})}{2\pi k_w} + \frac{\ln(D_{ext} / D_{dry})}{2\pi k_{metal}} \quad (\text{A-4})$$

Convection and conduction thermal resistance in the energy eq. (A-3) are described as functions of thermal conductivity of corresponding substances, Nusselt number, Nu , and hydraulic diameters of flow passage, as shown in eq. (A-4). Nusselt number can be derived from the Gnielinski correlation for forced convection in turbulent pipe flow. Entrance effect may be considered for higher heat and shear stress in the inlet regions. For an air-cooled cross-flow heat exchanger, the skin wall temperature T_w on the cooling side depends on both cooling air inlet temperature and its mass flow rate. In the following experiment section the boundary conditions of cooling air are controlled such that skin temperature T_w should be available for the model. Eq. (A-5) is used to compute temperature on the free surface, which is needed for phase change mass computation.

$$T_s = T_w + R_{cond} \frac{T - T_w}{R_{conv} + R_{cond}} \quad (\text{A-5})$$

Since the temperature drop over a cooler is less than 200°C, we use constant thermodynamic properties calculated at average pressure and temperature in the domain for constant-pressure specific heat, viscosity, and thermal conductivity.

$$\dot{m}_w = h_m \rho_g \ln \left(\frac{P - P_{w,f}}{P - P_w} \right) \quad (\text{A-6})$$

If we treat air-water vapor mixture as ideal gas, the mass flux of water condensation can be expressed as a function of water vapor partial pressure in the mixture, P_w , and water vapor pressure on the liquid film, $P_{w,f}$, as given in eq. (A-6) [142]. Here h_m is the mass transfer coefficient from air-water vapor mixture to the surface of water film. To obtain h_m , we assume that the Lewis relation in eq. (A-7) for air-water vapor mixture is valid and close to 1, then mass flux of eq. (A-6) can be expressed as a

function of Nusselt number and mass diffusivity of water vapor to air mixture, D_{w-a} , as shown in eq. (A-8) [143]. The water vapor pressure on the surface of liquid film can be predicted by the Antoine equation at free surface temperature T_s .

$$Le^{1/3} = \left(\frac{Sc}{Pr} \right)^{1/3} \cong 1 \quad (A-7)$$

$$\dot{m}_w = \frac{Nu}{D_{int}} \rho_g D_{w-a} \ln \left(\frac{P - P_{w,f}}{P - P_w} \right) \quad (A-8)$$

To understand instantaneous water volume trapped in the cooler core, we use an entrainment model to simplify liquid water movement simulation. This 1D entrainment model is based on mass conservation of liquid water film and an expression of stream-wise water transportation in liquid phase. Assumptions of this model are annular thin film and ignoring free surface instability when calculating average liquid velocity. Eq. (A-9) shows the mass conservation of liquid water film. Note that ρ_w , δ , and u_w are water density, film height, and average liquid velocity respectively. Instantaneous water volume trapped in the cooler core, which is $\delta(x,t)$, is available by solving the hyperbolic equation (A-9). Since condensation mass flux \dot{m}_w is addressed in eq. (A-6), the remaining unknown is u_w .

$$\frac{\partial(\rho_w \delta)}{\partial t} + \frac{\partial(\rho_w \delta u_w)}{\partial x} = \dot{m}_w \quad (A-9)$$

Figure A-2 is an illustration of velocity profiles u_g and u_l for gas mixture and an annular liquid water film in cylindrical coordinates. In eq. (A-9) the cross sectional area of the liquid film is approximated by film thickness due to the thin-film assumption ($D_{int} \gg \delta$).

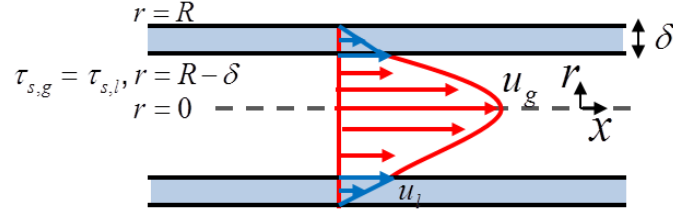


Figure A-2. Entrainment model illustration

To obtain the average velocity u_w , we have to assume a reasonable velocity profile u_l across the liquid film as given in eq. (A-10). Note V_l is the velocity on the free surface of liquid film, and R is radius of dry tube. The power m is a positive value which depends on flow fields. For example, if $m=1$ the velocity profile is linear as Couette flow. In practice, the flow is in the turbulent regime. We calibrate m from 0.5 to 0.1 to match experimental data for each particular cooler application.

The velocity profile u_l satisfies the no-slip condition at the wall and V_l has the same velocity as gas mixture on the free surface.

$$\begin{aligned}
 u_l &= V_l \left(\frac{\delta}{R} \right)^m \\
 u_l &= V_l, \quad r = R - \delta \\
 u_l &= 0, \quad r = R
 \end{aligned}
 \tag{A-10}$$

In addition this velocity profile should provide shear stress balance on free surface as shown in eq. (A-11). We approximate the shear stress from gas mixture exerting on the free surface by the friction loss of gas mixture, and hence V_l is derived in eq. (A-12).

$$\tau_{s,g} = \frac{1}{2} f \rho_g u^2 = -\mu_l \left. \frac{\partial u_l}{\partial r} \right|_{r=R-\delta} = \mu_w \frac{m}{R} V_l \left(\frac{\delta}{R} \right)^{m-1}
 \tag{A-11}$$

$$V_l = \frac{1}{\mu_w} \left(\frac{1}{2} f \rho_g u^2 \right) \frac{R}{m} \left(\frac{R}{\delta} \right)^{m-1}
 \tag{A-12}$$

Note this approach is a one-way coupling between liquid and gas phase, which dramatically eases two-phase modeling. Then we integrate velocity from $r=R$ to $r=R-\delta$ to obtain stream-wise flow rate of liquid water in eq. (A-13) and average liquid velocity u_w given in eq. (A-14).

$$\dot{m}_l = \frac{\pi D_{dry} \rho_w \delta^2}{\mu_w m(m+1)} \left(\frac{1}{2} f \rho_g u^2 \right) \quad (\text{A-13})$$

$$u_w = \frac{\dot{m}_l}{\delta \pi D_{dry}} = \frac{\rho_w \delta}{\mu_w m(m+1)} \left(\frac{1}{2} f \rho_g u^2 \right) \quad (\text{A-14})$$

With u_w we are able to solve eq. (A-9) and close the entrainment model.

The following steps constitute the condensation model algorithm:

1. Begin with initial conditions and boundary conditions.
2. Solve Eq. (A-1)-(A-3) for water vapor mass fraction, bulk velocity, pressure, friction factor, Nusselt number, and temperature with boundary conditions.
3. Compute condensation flux with local vapor pressure, Nusselt number, and free surface temperature from eq. (A-8).
4. Compute average liquid speed from eq. (A-14)
5. Solve eq. (A-9) with a hyperbolic solver for liquid water distribution $\delta(x,t)$.
6. With $\delta(x,t)$, return to step 2 for time marching.

Appendix B. Data of commercial premium gasoline fuel properties

Table B-1. Fuel properties of premium gasoline

<i>Elemental Analysis</i>	
Carbon (Wt%)	81.94 % m/m
Hydrogen (Wt%)	14.43 % m/m
Oxygen (from oxygenates)	3.63 % m/m
<i>Oxygenates by GC</i>	
Ethanol (EtOH)	10.46 % m/m
<i>FIA - Total Sample Basis</i>	
Avg. % Vol of Saturates Zone	73.9 % v/v
Avg. % Volume of Olefins Zone	2.4 % v/v
Avg. % Vol of Aromatics Zone	14.0 % v/v
<i>Individual Parameters</i>	
API Gravity at 15.56°C	61.4 °API
Density at 15.56°C	0.7329 g/mL
Spec. Grav. at 15.56°C/15.56°C	0.7336
Gross Heating Value (BTU/lb)	19406 BTU/lb
Net Heating Value (BTU/lb)	18089 BTU/lb
<i>Octanes</i>	
Research Octane Number	98.7
Motor Octane Number	90.0
AKI Calculation	94.4
Sensitivity	8.7

Bibliography

- [1] An F, Gordon D, He H, Kodjak D, Daniel R. Passenger Vehicle Greenhouse Gas and Fuel Economy Standards: A Global Update 2007.
- [2] Gerty MD, Heywood JB. An Investigation of Gasoline Engine Knock Limited Performance and the Effects of Hydrogen Enhancement, 2006. doi:10.4271/2006-01-0228.
- [3] Heywood JB. Internal combustion engine fundamentals. New York: McGraw-Hill; 1988.
- [4] Kern J, Wallner R. The Selection and Evaluation of Charge-Air Coolers for Vehicle Engines, 840350. doi:10.4271/840350.
- [5] Emmerling RC, Kiser CE. System Design Considerations for Low Temperature Aftercooling, 821051. doi:10.4271/821051.
- [6] Häggh B, Holmér E. Air-to-Air Charge Air Cooling for Truck Engines, 790770. doi:10.4271/790770.
- [7] Tang Y. The Condensation within a CAC - Thermodynamics Analysis. SAE 2011-01-1168 2011. doi:10.4271/2011-01-1168.
- [8] Smith PR. Durability Concerns of Aluminum Air to Air Charge Air Coolers, 931125. doi:10.4271/931125.
- [9] Harada M, Yasuda T, Terachi S, Pujols S, Spenny JR. Water Cooled Charge Air Cooler Development, 2016. doi:10.4271/2016-01-0651.
- [10] Morgado AO, Miranda JM, Araújo JDP, Campos J. Review on vertical gas-liquid slug flow. *Int J Multiph Flow* 2016;85:348–368.
- [11] Vij AK, Dunn WE. Modeling of two-phase flows in horizontal tubes. *Air Conditioning and Refrigeration Center. College of Engineering ...*; 1996.
- [12] Boure JA, Bergles AE, Tong LS. Review of two-phase flow instability. *Nucl Eng Des* 1973;25:165–92. doi:10.1016/0029-5493(73)90043-5.
- [13] Kakac S, Bon B. A Review of two-phase flow dynamic instabilities in tube boiling systems. *Int J Heat Mass Transf* 2008;51:399–433. doi:10.1016/j.ijheatmasstransfer.2007.09.026.
- [14] Dalkilic AS, Wongwises S. Intensive literature review of condensation inside smooth and enhanced tubes. *Int J Heat Mass Transf* 2009;52:3409–3426.
- [15] Dalkiliç AS, Celen A, Awad MM, Wongwises S. A critical review on the determination of convective heat transfer coefficient during condensation in smooth and enhanced tubes. vol. 2, 2013. doi:10.1115/HT2013-17565.

- [16] Murase T, Wang HS, Rose JW. Effect of inundation for condensation of steam on smooth and enhanced condenser tubes. *Int J Heat Mass Transf* 2006;49:3180–3189.
- [17] Vyskocil L, Schmid J, Macek J. CFD simulation of air–steam flow with condensation. *Nucl Eng Des* 2014;279:147–157.
- [18] Cash RY, Lumsdaine E, Talekar A, AbdulNour B. An Experimental and Computational Investigation of Water Condensation inside the Tubes of an Automotive Compact Charge Air Cooler, 2016. doi:10.4271/2016-01-0224.
- [19] Colosqui CE, Cheah MJ, Kevrekidis IG, Benziger JB. Droplet and slug formation in polymer electrolyte membrane fuel cell flow channels: The role of interfacial forces. *J Power Sources* 2011;196:10057–10068.
- [20] Cheah MJ, Kevrekidis IG, Benziger JB. Water slug to drop and film transitions in gas-flow channels. *Langmuir* 2013;29:15122–15136.
- [21] Cheah MJ, Kevrekidis IG, Benziger JB. Water slug formation and motion in gas flow channels: the effects of geometry, surface wettability, and gravity. *Langmuir* 2013;29:9918–9934.
- [22] Cho SC, Wang Y, Chen KS. Droplet dynamics in a polymer electrolyte fuel cell gas flow channel: Forces, deformation, and detachment. I: Theoretical and numerical analyses. *J Power Sources* 2012;206:119–128.
- [23] Cho SC, Wang Y, Chen KS. Droplet dynamics in a polymer electrolyte fuel cell gas flow channel: Forces, Deformation and detachment. II: Comparisons of analytical solution with numerical and experimental results. *J Power Sources* 2012;210:191–197.
- [24] Orell A. Experimental validation of a simple model for gas–liquid slug flow in horizontal pipes. *Chem Eng Sci* 2005;60:1371–1381.
- [25] Tay BL, Thorpe RB. Hydrodynamic forces acting on pipe bends in gas–liquid slug flow. *Chem Eng Res Des* 2014;92:812–825.
- [26] Chang-Mateu I-HM. Entrainment and condensation effects in a steam-water shock tube. Northwestern Univ., Evanston, IL (USA); 1986.
- [27] Koestel A, Gido RG, Gilbert JS. Film entrainment and drop deposition for two-phase flow. 1980.
- [28] Ousaka A, Kariyasaki A. Distribution of entrainment flow rate for air-water annular two-phase flow in a horizontal tube. *JSME Int J Ser 2 Fluids Eng Heat Transf Power Combust Thermophys Prop* 1992;35:354–360.
- [29] Assad A, Jan C, Bertodano M de, Beus SG. Entrainment measurements in annular flow. Bettis Atomic Power Lab., West Mifflin, PA (United States); 1997.
- [30] Perry RH, Green DW, ebrary I. Perry’s chemical engineers’ handbook. New York: McGraw-Hill; 2008.
- [31] Gruselle F, Steimes J, Hendrick P. Study of a Two-Phase Flow Pump and Separator System. *J Eng Gas Turbines Power* 2011;133:062401-062401–8. doi:10.1115/1.4002470.
- [32] Hoffman AC, Stein LE, Hoffmann AC, Stein LE. Gas cyclones and swirl tubes. vol. 56. Springer; 2002.
- [33] Fewel KJJ (Peerless MC, Kean JA (Richfield II. Computer Modeling Aids Separator Retrofit. *Oil Gas J U S* 1992;90:27.

- [34] Li J, Wang X, Huang S. Droplets turbulence effect of gas-water separator with corrugated plates. *Trans Tianjin Univ* 2009;15:440. doi:10.1007/s12209-009-0076-4.
- [35] Nakao T, Saito Y, Souma H, Kawasaki T, Aoyama G. Droplet Behavior Analyses in the BWR Dryer and Separator. *J Nucl Sci Technol* 1998;35:286–93. doi:10.1080/18811248.1998.9733858.
- [36] Nakao T, Nagase M, Aoyama G, Murase M. Development of simplified wave-type vane in BWR steam dryer and assessment of vane droplet removal characteristics. *J Nucl Sci Technol* 1999;36:424–432.
- [37] Mochizuki H, Hirao Y. Development of Steam Separator Performance Analysis Code and Its Validation, (III). *J Nucl Sci Technol* 1994;31:782–95. doi:10.1080/18811248.1994.9735224.
- [38] Zhongyi W, Jia H, Lei W, Tao S. The comparative study on the typical marine gas-water separator inertial blades. 2011 IEEE 3rd Int. Conf. Commun. Softw. Netw., 2011, p. 588–91. doi:10.1109/ICCSN.2011.6014962.
- [39] Wyman ET. *Combination steam and gas turbine*, 1949.
- [40] Coutant JG. Water or steam injection in gas turbine cycle provides unique performance. *Power Eng* 1959;63:93–5.
- [41] Harslem EW. *Liquid cooled gas turbine engine*, 1966.
- [42] Mathioudakis K. Analysis of the Effects of Water Injection on the Performance of a Gas Turbine. *J Eng Gas Turbines Power* 2002;124:489–495.
- [43] Bouam A, Aissani S, Kadi R. Combustion chamber steam injection for gas turbine performance improvement during high ambient temperature operations. *J Eng Gas Turbines Power* 2008;130:041701.
- [44] Bhagat M, Cung K, Johnson J, Lee S-Y, Naber J, Barros S. Experimental and Numerical Study of Water Spray Injection at Engine-Relevant Conditions. *SAE Tech. Pap.*, vol. 2, 2013. doi:10.4271/2013-01-0250.
- [45] Wang J-K, Li J-L, Wu M-H, Chen R-H. Reduction of Nitric Oxide Emission From a SI Engine by Water Injection at the Intake Runner 2009:335–40. doi:10.1115/IMECE2009-12517.
- [46] Dryer FL. Water addition to practical combustion systems—Concepts and applications. *Symp Int Combust* 1977;16:279–95. doi:10.1016/S0082-0784(77)80332-9.
- [47] Law CK, Lee CH, Srinivasan N. Combustion characteristics of water-in-oil emulsion droplets. *Combust Flame* 1980;37:125–143.
- [48] Jeong I, Lee K-H, Kim J. Characteristics of auto-ignition and micro-explosion behavior of a single droplet of water-in-fuel. *J Mech Sci Technol* 2008;22:148–156.
- [49] Tsao KC, Wang CL, Miller EM. Performance of Gasoline-Water Fuel in a Modified SI Engine, 1984. doi:10.4271/841399.
- [50] Bratkov AA, Azev VS, Radchenko ED, Gladkikh VA, Livshits SM. Addition of water to motor fuels — One of the means for conservation and expansion of fuel resources. *Chem Technol Fuels Oils* 1980;16:731–5. doi:10.1007/BF00745463.
- [51] Matheaus AC, Ryan TW, Daly D, Langer DA, Musculus MPB. Effects of PuriNOx™ Water-Diesel Fuel Emulsions on Emissions and Fuel Economy in a Heavy-Duty Diesel Engine, 2002. doi:10.4271/2002-01-2891.

- [52] Brown KF, Chadderton J, Daly DT, Langer DA, Duncan D. Opportunity for Diesel Emission Reductions Using Advanced Catalysts and Water Blend Fuel, 2000. doi:10.4271/2000-01-0182.
- [53] Boekhaus KL, Copeland LC. Performance Characteristics of Stratified Charge Vehicles with Conventional Fuels and Gasoline Blended with Alcohol and Water, 1976. doi:10.4271/760197.
- [54] Bratkov AA. Experience in Use of Water-Fuel Emulsions. *Chem Technol Fuels Oils* 1980;16:731–5.
- [55] Rajan S, Saniee FF. Water—ethanol—gasoline blends as spark ignition engine fuels. *Fuel* 1983;62:117–21. doi:10.1016/0016-2361(83)90265-X.
- [56] Berni F, Breda S, D’Adamo A, Fontanesi S, Cantore G. Numerical Investigation on the Effects of Water/Methanol Injection as Knock Suppressor to Increase the Fuel Efficiency of a Highly Downsized GDI Engine, 2015. doi:10.4271/2015-24-2499.
- [57] Durst B, Landerl C, Poggel J, Schwatz C, Kleczka W, Hußmann B. BMW Water Injection: Initial Experience and Future Potentials. *Int Wien Mot* 2017.
- [58] Porter JC. Alcohol-Water Injection for High Compression Engines. Warrendale, PA: SAE International; 1950. doi:10.4271/500042.
- [59] Peters BD, Stebar RF. Water-Gasoline Fuels-Their Effect on Spark Ignition Engine Emissions and Performance, 1976. doi:10.4271/760547.
- [60] Lanzafame R. Water Injection Effects In A Single-Cylinder CFR Engine, 1999. doi:10.4271/1999-01-0568.
- [61] Brusca S, Lanzafame R. Water Injection in IC - SI Engines to Control Detonation and to Reduce Pollutant Emissions, 2003. doi:10.4271/2003-01-1912.
- [62] Nicholls JE, Ei-Messiri IA, Newhali HK. Inlet Manifold Water Injection for Control of Nitrogen Oxides — Theory and Experiment, 1969. doi:10.4271/690018.
- [63] Harrington JA. Water Addition to Gasoline-Effect on Combustion, Emissions, Performance, and Knock, 1982. doi:10.4271/820314.
- [64] Ladommatos N, Abdelhalim SM, Zhao H, Hu Z. The Dilution, Chemical, and Thermal Effects of Exhaust Gas Recirculation on Diesel Engine Emissions - Part 3: Effects of Water Vapour, 1997. doi:10.4271/971659.
- [65] Subramanian V, Mallikarjuna JM, Ramesh A. Effect of water injection and spark timing on the nitric oxide emission and combustion parameters of a hydrogen fuelled spark ignition engine. *Int J Hydrog Energy* 2007;32:1159–73. doi:10.1016/j.ijhydene.2006.07.022.
- [66] Nande AM, Wallner T, Naber J. Influence of Water Injection on Performance and Emissions of a Direct-Injection Hydrogen Research Engine, 2008. doi:10.4271/2008-01-2377.
- [67] Shah SR, Maiboom A, Tauzia X, Hetet J-F. Experimental Study of Inlet Manifold Water Injection on a Common Rail HSDI Automobile Diesel Engine, Compared to EGR with Respect to PM and Nox Emissions and Specific Consumption, 2009. doi:10.4271/2009-01-1439.
- [68] Tauzia X, Maiboom A, Shah SR. Experimental study of inlet manifold water injection on combustion and emissions of an automotive direct injection Diesel engine. *Energy* 2010;35:3628–39. doi:10.1016/j.energy.2010.05.007.

- [69] Boretti A. Water injection in directly injected turbocharged spark ignition engines. *Appl Therm Eng* 2013;52:62–8. doi:10.1016/j.applthermaleng.2012.11.016.
- [70] Karagöz Y, Yüksek L, Sandalcı T, Dalkılıç AS. An experimental investigation on the performance characteristics of a hydroxygen enriched gasoline engine with water injection. *Int J Hydrog Energy* 2015;40:692–702. doi:10.1016/j.ijhydene.2014.11.013.
- [71] d’Adamo A, Berni F, Breda S, Lugli M, Fontanesi S, Cantore G. A Numerical Investigation on the Potentials of Water Injection as a Fuel Efficiency Enhancer in Highly Downsized GDI Engines, 2015. doi:10.4271/2015-01-0393.
- [72] Chintala V, Subramanian KA. Experimental investigation of hydrogen energy share improvement in a compression ignition engine using water injection and compression ratio reduction. *Energy Convers Manag* 2016;108:106–19. doi:10.1016/j.enconman.2015.10.069.
- [73] Netzer C, Franken T, Seidel L, Lehtiniemi H, Mauss F. Numerical Analysis of the Impact of Water Injection on Combustion and Thermodynamics in a Gasoline Engine using Detailed Chemistry, 2018. doi:10.4271/2018-01-0200.
- [74] Sun Y, Fischer M, Bradford M, Kotrba A, Randolph E. Water Recovery from Gasoline Engine Exhaust for Water Injection, 2018. doi:10.4271/2018-01-0369.
- [75] Teodosio L, De Bellis V, Bozza F. Combined Effects of Valve Strategies, Compression Ratio, Water Injection and Cooled EGR on the Fuel Consumption of a Small Turbocharged VVA Spark-Ignition Engine, 2018. doi:10.4271/2018-01-0854.
- [76] Karim GA, Amoozegar N. Determination of the Performance of a Dual Fuel Diesel Engine with the Addition of Various Liquid Fuels to the Intake Charge, 1983. doi:10.4271/830265.
- [77] Tesfa B, Mishra R, Gu F, Ball AD. Water injection effects on the performance and emission characteristics of a CI engine operating with biodiesel. *Renew Energy* 2012;37:333–44. doi:10.1016/j.renene.2011.06.035.
- [78] Miller CD. End-zone Water Injection as a Means of Suppressing Knock in a Spark-ignition Engine 1944.
- [79] Lestz SS, Meyer WE, Colony CM. Emissions from a Direct-Cylinder Water-Injected Spark-Ignition Engine. *SAE Trans* 1972;81:392–8.
- [80] Gadallah AH, Elshenawy EA, Elzahaby AM, El-Salmawy HA, Bawady AH. Effect of In Cylinder Water Injection Strategies on Performance and Emissions of a Hydrogen Fuelled Direct Injection Engine, 2009. doi:10.4271/2009-01-1925.
- [81] Conklin JC, Szybist JP. A highly efficient six-stroke internal combustion engine cycle with water injection for in-cylinder exhaust heat recovery. *Energy* 2010;35:1658–64. doi:10.1016/j.energy.2009.12.012.
- [82] Adnan R, Masjuki HH, Mahlia TMI. Performance and emission analysis of hydrogen fueled compression ignition engine with variable water injection timing. *Energy* 2012;43:416–26. doi:10.1016/j.energy.2012.03.073.
- [83] Fu L, Wu Z, Yu X, Deng J, Hu Z, Li L. Experimental Investigation of Combustion and Emission Characteristics for Internal Combustion Rankine Cycle Engine under Different Water Injection Laws. *Energy Procedia* 2015;66:89–92. doi:10.1016/j.egypro.2015.02.047.

- [84] Mingrui W, Thanh Sa N, Turkson RF, Jinping L, Guanlun G. Water injection for higher engine performance and lower emissions. *J Energy Inst* 2017;90:285–99. doi:10.1016/j.joei.2015.12.003.
- [85] Hoppe F, Thewes M, Baumgarten H, Dohmen J. Water injection for gasoline engines: Potentials, challenges, and solutions. *Int J Engine Res* 2016;17:86–96. doi:10.1177/1468087415599867.
- [86] Kim J, Park H, Bae C, Choi M, Kwak Y. Effects of water direct injection on the torque enhancement and fuel consumption reduction of a gasoline engine under high-load conditions. *Int J Engine Res* 2016;17:795–808. doi:10.1177/1468087415613221.
- [87] Wu Z-J, Yu X, Fu L-Z, Deng J, Hu Z-J, Li L-G. A high efficiency oxyfuel internal combustion engine cycle with water direct injection for waste heat recovery. *Energy* 2014;70:110–20. doi:10.1016/j.energy.2014.03.095.
- [88] Ishida M, Ueki H, Sakaguchi D. Prediction of NO_x Reduction Rate Due to Port Water Injection in a DI Diesel Engine, 1997. doi:10.4271/972961.
- [89] Sullerey RK, Agarwal A. Effect of Water Injection on Emission Characteristics of a Turbocharged Diesel Engine 2009:371–8. doi:10.1115/ICES2009-76025.
- [90] Obert EF. *Detonation and Internal Coolants*. Warrendale, PA: SAE International; 1948. doi:10.4271/480173.
- [91] Barnett HC, Hibbard RR. *Basic Considerations in the Combustion of Hydrocarbon Fuels with Air* 1957.
- [92] Fenn JB, Calcote HF. Activation energies in high temperature combustion. *Symp Int Combust* 1953;4:231–9. doi:10.1016/S0082-0784(53)80029-9.
- [93] Eberius H, Hoyermann K, Wagner HG. Zur Reaktion $H + H + H_2O \rightarrow H_2 + H_2O$. *Berichte Bunsenges Für Phys Chem* 1969;73:962–6. doi:10.1002/bbpc.19690731006.
- [94] Fristrom RM, Westenberg AA. *Flame structure*. McGraw-Hill; 1965.
- [95] Bowman CT. Non-equilibrium radical concentrations in shock-initiated methane oxidation. *Symp Int Combust* 1975;15:869–82. doi:10.1016/S0082-0784(75)80354-7.
- [96] Le Cong T, Dagaut P. Effect of Water Vapor on the Kinetics of Combustion of Hydrogen and Natural Gas: Experimental and Detailed Modeling Study 2008:319–28. doi:10.1115/GT2008-50272.
- [97] Mazas AN, Fiorina B, Lacoste DA, Schuller T. Effects of water vapor addition on the laminar burning velocity of oxygen-enriched methane flames. *Combust Flame* 2011;158:2428–40. doi:10.1016/j.combustflame.2011.05.014.
- [98] Bak J, Clausen S. FTIR emission spectroscopy methods and procedures for real time quantitative gas analysis in industrial environments. *Meas Sci Technol* 2002;13:150. doi:10.1088/0957-0233/13/2/302.
- [99] Brettschneider J. Berechnung des Luftverhältnisses Lambda von Luft-Kraftstoff-Gemischen und des Einflusses von Messfehlern auf Lambda. *BOSCH TECH BER* 1979;6.
- [100] ANSYS CFX-Solver Theory Guide. ANSYS, INC.; 2013.
- [101] ANSYS CFX-Solver Modeling Guide. ANSYS, INC.; 2013.
- [102] Ebersole GD, Manning FS. *Engine Performance and Exhaust Emissions: Methanol versus Isooctane*, 1972. doi:10.4271/720692.

- [103] Dalavia D, Santos D, Buboli HC, Bortolini M, Bassani IA. Modifications in CFR Engine in Order to Measure Overall Burning Time, 2010. doi:10.4271/2010-36-0119.
- [104] Morganti K, Foong TM, Brear M, Da Silva G, Yang Y, Dryer F. Design and Analysis of a Modified CFR Engine for the Octane Rating of Liquefied Petroleum Gases (LPG). *SAE Int J Fuels Lubr* 2014;7:283–300. doi:10.4271/2014-01-1474.
- [105] Perumal M, Floweday G. An Investigation of Cascading Autoignition and Octane Number using a Multi-zone Model of the CFR Engine. *SAE Int J Engines* 2011;4:976–97. doi:10.4271/2011-01-0850.
- [106] Thiart A, Floweday G, Meyer C. A CFD Study of Fuel Evaporation and Related Thermo-fluid Dynamics in the Inlet Manifold, Port and Cylinder of the CFR Octane Engine. *SAE Int J Fuels Lubr* 2012;5:1264–76. doi:10.4271/2012-01-1715.
- [107] Wimmer DB, Lee RC. An Evaluation of the Performance and Emissions of a CFR Engine Equipped with a Prechamber, 1973. doi:10.4271/730474.
- [108] Zhang Y. Low Temperature Oxidation of Biodiesel Surrogates in a Motored Engine and the Oxidation Behavior of Soot Generated from the Combustion of a Biodiesel Surrogate in a Diffusion Flame. Pennsylvania State University, 2010.
- [109] Lilik GK. Advanced Diesel Combustion of High Cetane Number Fuels and the Impacts on the combustion Process. Pennsylvania State University, 2012.
- [110] Kalaskar VB. Ignition Behavior of Gasolines and Surrogate Fuels in Low Temperature Combustion Strategies. Pennsylvania State University, 2015.
- [111] Kang D. Impacts of Fuel Chemical Structure and Composition on Fundamental Ignition Behavior and Autoignition Chemistry in a Motored Engine. University of Michigan, 2016.
- [112] Curran HJ, Gaffuri P, Pitz WJ, Westbrook CK, Leppard WR. Autoignition chemistry in a motored engine: An experimental and kinetic modeling study. *Symp Int Combust* 1996;26:2669–77. doi:10.1016/S0082-0784(96)80102-0.
- [113] Kalghatgi GT. Fuel Anti-Knock Quality - Part I. *Engine Studies*, 2001. doi:10.4271/2001-01-3584.
- [114] Singh E, Badra J, Mehl M, Sarathy SM. Chemical Kinetic Insights into the Octane Number and Octane Sensitivity of Gasoline Surrogate Mixtures. *Energy Fuels* 2017;31:1945–60. doi:10.1021/acs.energyfuels.6b02659.
- [115] Bradley D, Kalghatgi GT, Golombok M. Fuel Blend and Mixture Strength Effects on Autoignition Heat Release Rates and Knock Intensity in S.I. Engines, 1996. doi:10.4271/962105.
- [116] Morgan N, Smallbone A, Bhave A, Kraft M, Cracknell R, Kalghatgi G. Mapping surrogate gasoline compositions into RON/MON space. *Combust Flame* 2010;157:1122–31. doi:10.1016/j.combustflame.2010.02.003.
- [117] Newitt DN. The Oxidations of Hydrocarbons at High Pressure. *Chem Rev* 1937;21:299–317.
- [118] CHEMKIN Tutorials Manual. Reaction Design; 2011.
- [119] CHEMKIN Theory Manual. Reaction Design; 2004.
- [120] Gauthier BM, Davidson DF, Hanson RK. Shock tube determination of ignition delay times in full-blend and surrogate fuel mixtures. *Combust Flame* 2004;139:300–11. doi:10.1016/j.combustflame.2004.08.015.

- [121] Burcat A, Scheller K, Lifshitz A. Shock-tube investigation of comparative ignition delay times for C1-C5 alkanes. *Combust Flame* 1971;16:29–33. doi:10.1016/S0010-2180(71)80007-X.
- [122] Ciezki HK, Adomeit G. Shock-tube investigation of self-ignition of n-heptane-air mixtures under engine relevant conditions. *Combust Flame* 1993;93:421–33. doi:10.1016/0010-2180(93)90142-P.
- [123] Sarathy SM, Kukkadapu G, Mehl M, Wang W, Javed T, Park S, et al. Ignition of alkane-rich FACE gasoline fuels and their surrogate mixtures. *Proc Combust Inst* 2015;35:249–57. doi:10.1016/j.proci.2014.05.122.
- [124] Healy D, Donato NS, Aul CJ, Petersen EL, Zinner CM, Bourque G, et al. n-Butane: Ignition delay measurements at high pressure and detailed chemical kinetic simulations. *Combust Flame* 2010;157:1526–39. doi:10.1016/j.combustflame.2010.01.016.
- [125] Healy D, Donato NS, Aul CJ, Petersen EL, Zinner CM, Bourque G, et al. Isobutane ignition delay time measurements at high pressure and detailed chemical kinetic simulations. *Combust Flame* 2010;157:1540–51. doi:10.1016/j.combustflame.2010.01.011.
- [126] Allard LN, Webster GD, Hole NJ, Ryan TW, Ott D, Fairbridge CW. Diesel Fuel Ignition Quality as Determined in the Ignition Quality Tester (IQT), 1996. doi:10.4271/961182.
- [127] Naser N, Yang SY, Kalghatgi G, Chung SH. Relating the octane numbers of fuels to ignition delay times measured in an ignition quality tester (IQT). *Fuel* 2017;187:117–27. doi:10.1016/j.fuel.2016.09.013.
- [128] Bogin GE, DeFilippo A, Chen JY, Chin G, Luecke J, Ratcliff MA, et al. Numerical and Experimental Investigation of n-Heptane Autoignition in the Ignition Quality Tester (IQT). *Energy Fuels* 2011;25:5562–72. doi:10.1021/ef201079g.
- [129] Turányi T. Applications of sensitivity analysis to combustion chemistry. *Reliab Eng Syst Saf* 1997;57:41–8. doi:10.1016/S0951-8320(97)00016-1.
- [130] Agbro E, Tomlin AS, Lawes M, Park S, Sarathy SM. The influence of n-butanol blending on the ignition delay times of gasoline and its surrogate at high pressures. *Fuel* 2017;187:211–9. doi:10.1016/j.fuel.2016.09.052.
- [131] Saltelli A, Ratto M, Tarantola S, Campolongo F. Sensitivity Analysis for Chemical Models. *Chem Rev* 2005;105:2811–28. doi:10.1021/cr040659d.
- [132] Glarborg P, Miller JA, Kee RJ. Kinetic modeling and sensitivity analysis of nitrogen oxide formation in well-stirred reactors. *Combust Flame* 1986;65:177–202. doi:10.1016/0010-2180(86)90018-0.
- [133] Dougherty EP, Hwang J, Rabitz H. Further developments and applications of the Green's function method of sensitivity analysis in chemical kinetics. *J Chem Phys* 1979;71:1794–808. doi:10.1063/1.438530.
- [134] Pandis SN, Seinfeld JH. Sensitivity analysis of a chemical mechanism for aqueous-phase atmospheric chemistry. *J Geophys Res Atmospheres* 1989;94:1105–26. doi:10.1029/JD094iD01p01105.
- [135] Splitter D, Szybist J. Intermediate Alcohol-Gasoline Blends, Fuels for Enabling Increased Engine Efficiency and Powertrain Possibilities. *SAE Int J Fuels Lubr* 2014;7:29–47. doi:10.4271/2014-01-1231.

- [136] Smallwood I. Handbook of Organic Solvent Properties. Butterworth-Heinemann; 2012.
- [137] Andrae J, Johansson D, Björnbom P, Risberg P, Kalghatgi G. Co-oxidation in the auto-ignition of primary reference fuels and n-heptane/toluene blends. *Combust Flame* 2005;140:267–86. doi:10.1016/j.combustflame.2004.11.009.
- [138] Gardiner WCJ, editor. *Combustion Chemistry*. New York: Springer-Verlag; 1984.
- [139] Norton TS, Dryer FL. An experimental and modeling study of ethanol oxidation kinetics in an atmospheric pressure flow reactor. *Int J Chem Kinet* 1992;24:319–44. doi:10.1002/kin.550240403.
- [140] Hochgreb S, Dryer FL. A comprehensive study on CH₂O oxidation kinetics. *Combust Flame* 1992;91:257–84. doi:10.1016/0010-2180(92)90058-W.
- [141] Zigrang DJ, Sylvester ND. Explicit approximations to the solution of Colebrook's friction factor equation. *AIChE J* 1982;28:514–5. doi:10.1002/aic.690280323.
- [142] Faghri A, Zhang Y. *Transport Phenomena in Multiphase Systems*. Academic Press; 2006.
- [143] Baehr HD, Stephan K, SpringerLink (Online service). *Heat and Mass Transfer*. Berlin, Heidelberg: Springer-Verlag Berlin Heidelberg; 2011.